An investigation into harvesting solar energy using thermoelectric generator coupled IBR sheeting.

Submitted in fulfilment of the requirements of the degree of master's in mechanical engineering in the Faculty of Engineering and the Built Environment at the Durban University of Technology.

Momina Malik

Supervisor: Dr. M. Gilpin Date: 16/05/2024

Co – Supervisor: Mr. B. Graham Date: 16/05/2024

Abstract

There is a current global impending need for clean and renewable energy sources. Fossil fuels are non-renewable finite resources, which are dwindling because of high cost, and environmentally damaging retrieval techniques. South Africa's coal resources may soon reach their end, which further stresses the need for green energy. An efficient and more feasible alternative is solar energy. Thermoelectric generators (TEGs) may use the energy from the sun to generate power and are an innovative means to harvest electricity. The proposed study intends to validate whether TEGs are a potential method to harvesting solar power.

The study herein is a preliminary experimental investigation into a development in a TEG modular prototype. Relevant tests are run, and the performance characteristics obtained from experiments are discussed. The TEG system developed and tested in this study consists of 2 equally sized pieces of Inverted Box Rib (IBR) sheeting with one side exposed to a light source, while the other side remains shaded. An Arduino, connected and coded to read and display resulting temperatures, Peltier tiles, magnets, simple heatsinks and Multimeters are connected to measure open circuit voltage and closed-circuit current generated from the temperature difference between the two sides of the IBR sheeting.

The system aims to harvest energy whilst keeping the assembly and construction simple, practical, and minimalistic. Outdoor experiments were conducted to determine the temperatures and the resultant temperature gradients the configuration may experience in operation. The data collected established parameters for the laboratory experimental setup. The laboratory experiments characterized the power output of the units.

For comparative purposes, some variables were removed, such that the testing variable was isolated. Some environmental variables were removed by testing in a laboratory. The TEG was tested in the vertical position to allow for maximum natural convection, and hence may not reflect results that would be obtained in all applications. The TEG system is exposed to the light source at different distances, perpendicular to the sheets. The study intends to investigate the effect that the 2 variables have on the amount of solar power generated i.e., the colour of metal IBR sheeting, and the ideal electrical arrangement for scalability of Peltier tiles for maximum power output (P_{max}). The IV curve generation method (later explained in chapter 2.4.1) is used to read the parameters required to calculate P_{max}.

The results show a strong influence of the black coated sheets on the power output of the TEGs. It is deduced from solar experiments, that the aluminium rods used as the heatsink fulfilled its purpose of regulating a ΔT of 1-2°C.

Furthermore, the TEG in series configuration, generated the highest P_{max} when located 300mm from the heat source, followed by 600mm and lastly, 900mm. The same pattern is found for the unit and parallel configurations.

It may be concluded from the proposed TEG system that TEGs are a potential method of harvesting solar energy on IBR sheeting, specifically in a vertical position. However, applications of different orientations and geographical locations require further investigation. The results merit further investigation and refinement into the use of TEGs on IBR sheeting where the herein designed TEG system is set-up in a user friendly, simple, cost effective and practical manner for solar energy harvesting. While the power output per TEG tile is small in magnitude, the proposed configuration has potential in the coupling of multiple units to increase power output. The current work shows potential for the use of TEGs in this application. Through further investigation, refinement and cost analysis, the system may prove to be a practical method of solar energy harvesting.

Acknowledgements

I would like to thank sincerely and wholeheartedly:

- Dr. M. Gilpin for the guidance, mentorship, patience, and unmatched support provided to me during my research journey. Dr. Gilpin was my lecturer during my undergraduate studies at DUT and inspired me to study for a post graduate degree. Your words of encouragement “research is not a linear progression” resonated with me during my learning curve. Along with this master’s degree, I will be taking along inspiration, leadership skills, wisdom, and valuable insight for my future endeavours.
- Mr. B. Graham for the co-supervision, advice and necessary insight into this research, the thermodynamics, and thermal energy aspects of this research. Your expertise in publications have helped greatly.
- My family and friends, for the unwavering support. My mum, who has been a great inspiration and my role model. My dad, who made certain that every member of my family achieved the best education possible.
- DUT and the National Research Foundation (NRF), for the funding provided.

Declaration

I declare that this thesis is my own unaided work except where due acknowledgement is made to others. This thesis is being submitted for the Degree of Master of Engineering to the Department of Mechanical Engineering at the Durban University of Technology and has not been submitted previously for any other degree or examination.

16/05/2024

Momina Malik Date

Mark Gilpin (Supervisor)

Table of Contents

List of Figures

List of tables

List of abbreviations

TEG	–	Thermoelectric Generator
IBR	–	Inverted Box Rib
TEM	–	Thermoelectric Module
STEG	–	Solar Thermoelectric Generator
CSTEG	–	Concentrated Solar Thermoelectric Generator
STECG	–	Solar Thermoelectric Co-Generator

Nomenclature and symbols

T_h	–	Temperature of the hot side	$(°C)$
T_c	–	Temperature of the cold side	$(°C)$
ΔT	–	Temperature gradient between T_h and T_c	$(°C)$
Q_{in}	–	Heat flow entering the TEG	(J)
I	–	Current	(A)
I_s	–	Current measured under closed circuit condition	(A)
V	–	Voltage	(V)
V_o	–	Open circuit voltage	(V)
I_{o-s}	–	Current measured immediately after circuit is closed	(A)
V_{o-s}	–	Voltage measured immediately after circuit is closed	(V)
V_s	–	Short circuit voltage	(V)
I_o	–	Open circuit current	(A)
I_{MP}	–	Maximum current from the MPPT method	(A)
P_{max}	–	Maximum Power output by a TEG system	(W)
P_{MP}	–	The resultant maximum power from MPPT method	(W)
Voc	–	Voltage reading when $I = 0$ from MPPT method	(V)
Ioc	–	Current reading when V = 0 from MPPT method	(A)
V_{MP}	–	Maximum voltage from the MPPT method	(V)
$Pout$	–	Output Power	(W)
Vp	–	Voltage at the terminals for a parallel array	(V)
cm	–	Centimetre	
cm^2	–	Square centimetre	
mm	–	Millimetre	
mm^2	–	Square millimetre	
W	–	Watt	
mW	–	Milliwatt	
μW	–	Microwatt	
nW	–	Nanowatt	
W/m^2	–	The unit for solar irradiance i.e., Watts per square meter	
m	–	Gradient	

1 Introduction

1.1 Background Information

This section provides introductory background information into the aspects and sub-sections pertaining to this work. It is vital to understand the context around which this research revolves. A potential application of the proposed TEG system may be on the wall cladding or sheeting of large warehouses. Due to the large surface areas of the warehouse, which is exposed to heat, the system power output may be optimised.

1.1.1 Warehouse

Warehouses are housings designed to hold goods and products, belonging to a company before, during and even after they are transported. Warehouses are generally large structures with effective yet simple design. The structure is mainly comprised of steel beams and columns to create a tall yet durable frame. Other materials used in the structure are fiberglass, wood, and some plastics. This main structure is commonly made of Q345B Steel [1].

There has been an increase in demand for online commerce and retail due to the COVID19 pandemic, this leads to an increase in demand for warehouse construction as well. Since warehouse operations are becoming increasingly dependent on technology, they require a lot of energy, which has led to many companies opting for greener options [2]. Figure 1.1 illustrates a Prefab Steel Structure Warehouse.

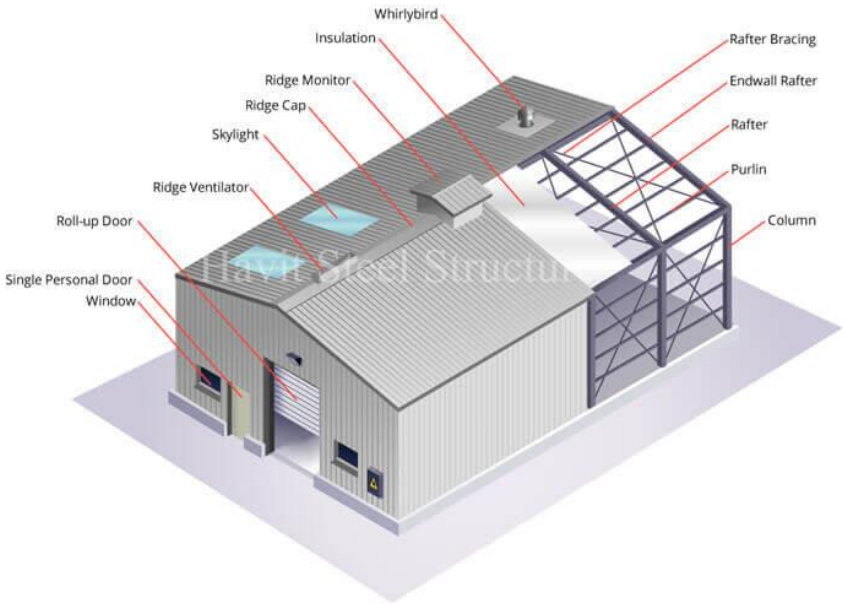

Figure 1.1: Image illustrating Prefab Steel Structure Warehouse [3]

1.1.2 Metal sheeting

One of the most popular metal sheeting profiles used in construction of industrial and commercial buildings, such as large warehouses and distribution centres, is the Inverted Box Rib (IBR) sheeting. IBR sheeting has an angular trapezoidal profile with large channels [3]. IBR roof sheeting is given its' name based on the size of the cover width of a singular sheet. Some examples are IBR 890 and IBR686, where the cover width is 890 mm and 686 mm respectively. IBR roof sheeting is used as roofing, and as wall cladding, and are available in different sheet thicknesses [4]. IBR roof sheeting is durable, easy to use and is regarded as the most efficient of all profiles [5]. The sheets are provided in galvanized steel and in different colours. Figure 1.2 shows the picture and dimensions of an IBR686 roof sheeting.

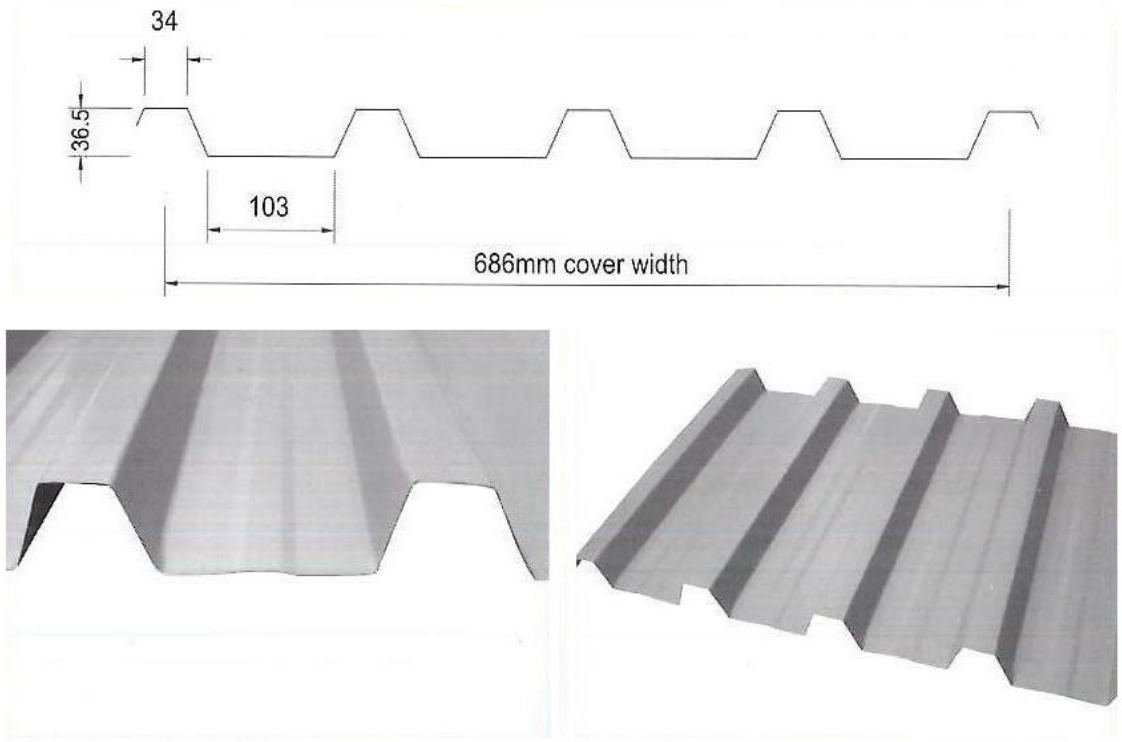

Figure 1.2: Picture and standard profile dimensions of the IBR686 roof sheeting [3]

Another commonly used and commercially available roof sheeting is the sinusoidal corrugated roof sheeting, which is shown in Figure 1.3. It is easy to use and is an effective profile for wall cladding and roofing [3].

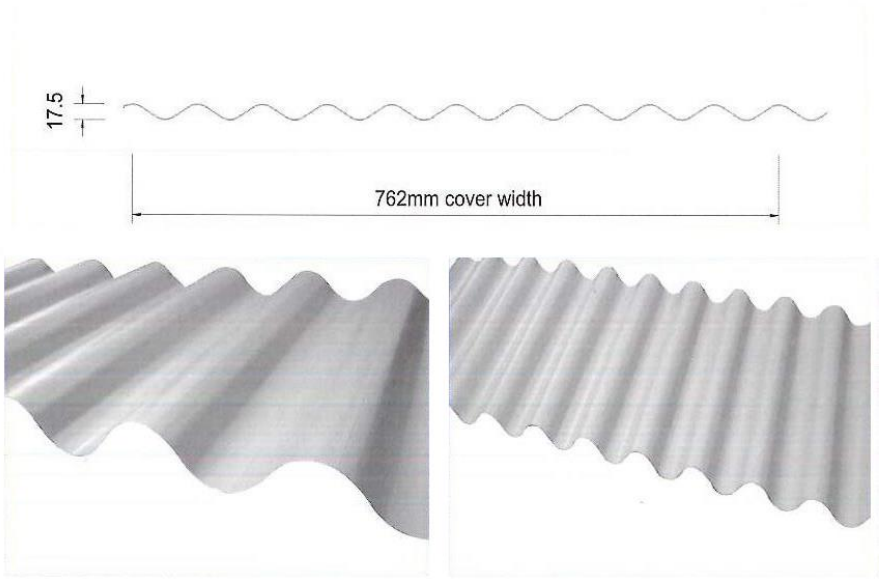

Figure 1.3: Image of standard profile dimensions of the sinusoidal corrugated roof sheeting [3]

1.1.3 Thermal transfer

Thermal or heat transfer refers to the movement of energy, or heat, due to a temperature difference between a surface and its surroundings. The temperature difference is sometimes referred to as the 'potential' that allows for heat transfer [6]. Heat is transferred in many ways. These are conduction, convection, and radiation. Conduction allows for heat transfer from objects of higher temperature to objects of lower temperature, this is between objects that are touching [6]. Figure 1.4 illustrates the conduction process from a higher temperature to lower temperature environment.

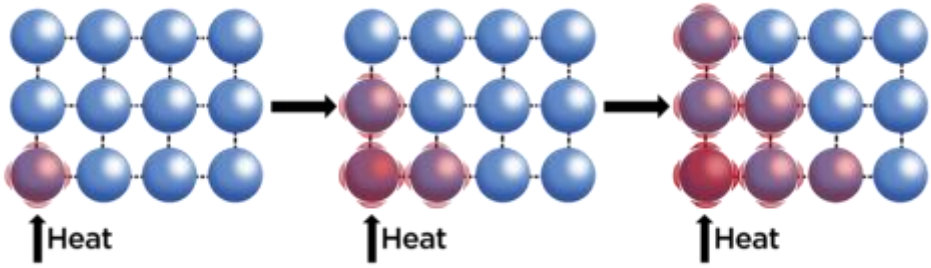

Figure 1.4: Conduction between particles of higher temperature to lower temperature [7]

Convection refers to the movement of fluid molecules from areas of higher temperature to areas of lower temperatures. Figure 1.5 illustrates the circulation of air due to convection in a room with a heat source.

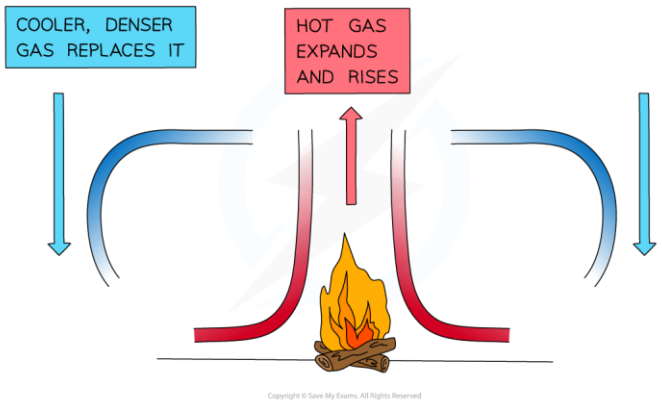

Figure 1.5: Image illustrating circulation of air due to convection in a room with a heat source [8]

Natural convection occurs on a vertical plate due to gravity and the difference in density gradients of the air surrounding the plate. The heated plate will cause the surrounding air to heat up, which reduces the air density. Buoyancy forces then move the low-density air upwards which is replaced by higher density air, i.e. cool air being drawn downwards [9]. Hence, the circulation of air is greater if the plate is placed vertically. Due to this factor that allows for natural cooling, the proposed TEG prototype in the experiments has the metal roof sheeting placed vertically. Therefore, the natural convection in the vertical sheets allow for the side in the shade to cool naturally which provides the relatively constant temperature difference benefiting the design. The TEG system can be applied to vertical or angled steel IBR sheets of a warehouse and similar structures. The results obtained by the TEG in a vertical position does not depict all expected results in the real world, where more thermal variables and orientations may be introduced.

1.1.4 Radiation and Solar Irradiation

Electromagnetic waves carry heat that is emitted from a body. Thermal radiation, also referred to as radiant heat is given off by these electromagnetic waves which are ubiquitous in some form or the other. Radiation is the transfer of energy between objects that do not need to be touched physically. In this way, the sun warms up the earth and is hence the main source of energy for solar radiation and ocean dynamics. 70% of the energy emitted by the sun is absorbed by the earth and the remaining energy is reflected into space. Current technological advancements are now capable of harvesting this energy to produce electricity [10]. Figure 1.6 shows an illustration of solar radiation on a photovoltaic panel for solar energy harvesting.

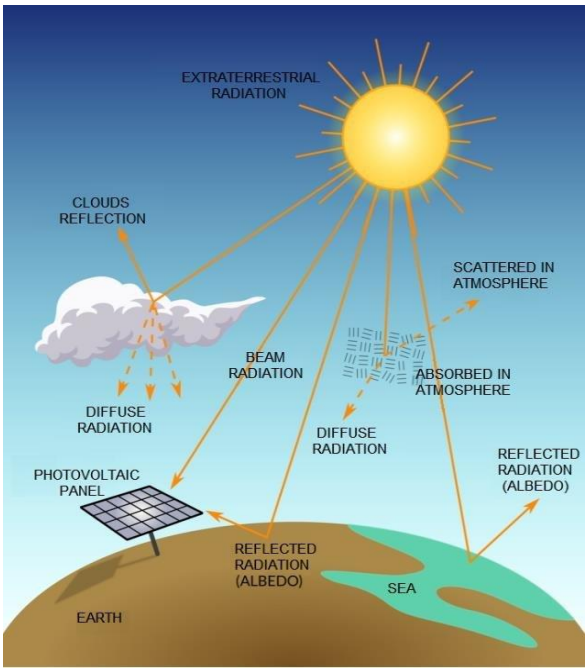

Figure 1.6: Solar radiation on a photovoltaic panel for solar energy harvesting [11]

Solar irradiance is the amount of solar energy received by the surface of the earth, per unit area and at a certain angle. It is measured in Watts per square meter (W/m^2) [12]. Solar irradiance is a key aspect in this research since heat from the sun and the atmosphere serves as the heat source for power generation.

Given the numerous variables influencing real-life results—incident angle, sun orientation, geographical coordinates, landscape, elevation, pitch, insulation, wind, and solar factors—the presented work aims to limit the number of variables to characterise the TEG performance.

1.1.4 The effect of dark colours on heat absorption

A salient aspect is that darker objects heat up more quickly than light colours, because dark colours absorb more of the different light energy wavelengths, while lighter colours, or shiny reflective surfaces reflect most of these wavelengths [13].

This is corroborated by Ehsan and Kianmehr [14], who conducted a straightforward experiment demonstrating that black surfaces absorb significantly more light, leading to rapid heat absorption compared to lighter surfaces. The colour black in general will absorb heat entirely [15].

Paminto, et al. [15] carried out experiments to establish the effect of different coloured acrylic boxes on the absorption of solar radiation energy. It was found that the order in which the coloured boxes absorbed heat, from highest to lowest was black, green, red, purple, yellow,

pink, blue, and white. The black box was found to absorb the most heat in the shortest period of time [15].

These aspects of thermal transfer are important in this study since thermal radiation from the sun reaches the surface of the roof-sheeting and increases its temperature. Power may then be generated, by a TEG, due to the existing temperature difference. The following sub-chapter explains this phenomenon in detail.

1.1.5 Heat Sinks

Thermal management in electronic devices are crucial to provide functional integrity of these devices [16]. A heat sink is one such heat dissipation component that transfers heat, typically generated by a mechanical or electronic device, into a desired coolant fluid such as air or water. They are designed to maximise the contact surface area between heat source and the coolant. Metals with a high thermal conductivity are used as heat sinks and these can be found in computers and high-powered devices such as lasers [17].

Heat moves away from the heat source via the heat sink by means of natural conduction. The coolant fluid passes over the surface of the heated heat sink and uses convection and thermal diffusion to remove this heat away, and into the environment. A temperature gradient is required for this process to occur i.e., for heat to move from a high temperature into a low temperature environment. A larger surface area will subsequently provide a larger area for convection and thermal diffusion [18]. Most heat sinks are designed with a base which is a flat metal sheet. Attached to the base are thermal fins which increase the surface area to dissipate the heat into its surrounding air [16]. Figure 1.7 illustrates the working principle of an aluminium heat sink with fins. Conduction occurs at point 1 and natural or forced convection occurs at point 2.

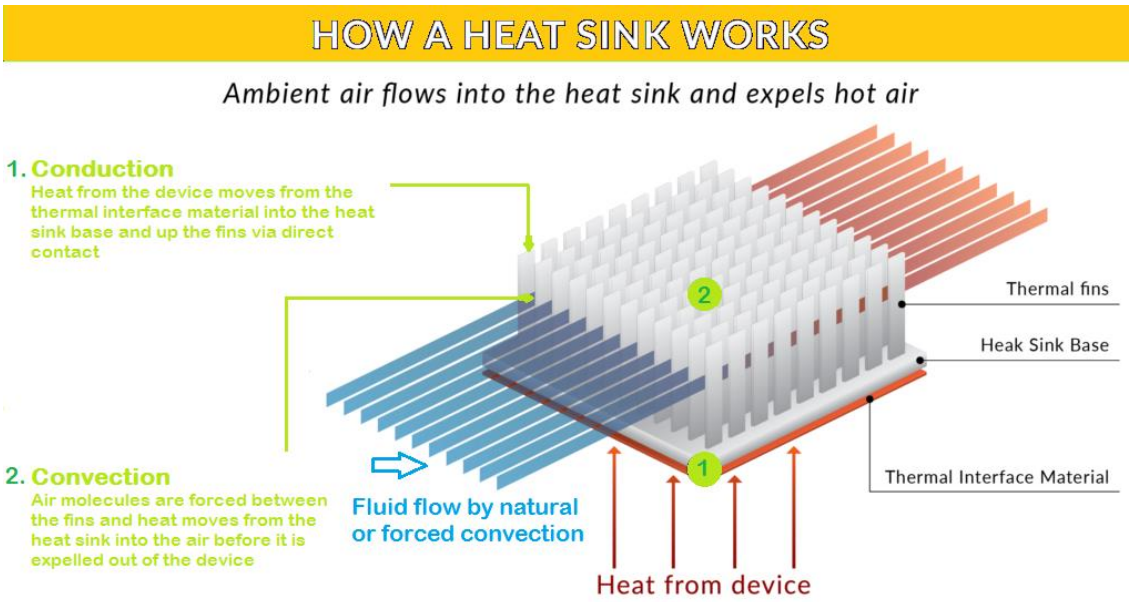

Figure 1.7: The working principle of an aluminium heat sink with fins [19]

1.1.6 Heat absorption by metals

Amongst common metals, copper has the highest thermal conductivity followed by aluminium. Therefore, these materials make for ideal heat sinks. However, Aluminium is more affordable than copper as aluminium is more abundant [17].

1.1.7 Thermoelectric Generators (TEGs)

Almost every human activity produces some form of waste heat, this is referred to as thermal energy. Power generation, industrial processes, transportation industry and domestic applications provide large amounts of thermal energy as a by-product. Generating power from recovered energy is quickly becoming a lucrative method of generating 'green energy'.

An innovative and emerging technological means to harvest the endless supply of thermal energy given off by the sun, utilises Thermoelectric generators (TEGs). TEGs are devices that convert thermal energy into electrical energy, and are solid-state devices that consist of thermocouples, connected electrically in series, within a thermoelectric module (Hereon referred to as a TEM). These thermoelectric materials convert temperature gradients supplied by a heat source and a heat sink into electrical energy [20]. TEMs have a 'hot side' (T_h) which receives the heat and is maintained at a higher temperature, and a 'cold side' (T_c) which is relatively cooler [21]. The thermocouple in the TEM consists of two dissimilar materials, P and N type, joined electrically in series and thermally in parallel [22].

TEGs adopt a working principle called the Seebeck effect. This is a phenomenon by which the imposition of a temperature difference between two different electrical conductors produces a voltage [23]. Therefore, the conversion efficiency of heat to electricity in a TEM is a function of the temperature gradient and the thermo-electric material properties i.e. thermal conductivity, electric resistivity and the Seebeck coefficient [21]. The TEM scheme and operation can be seen in Figure 1.8.

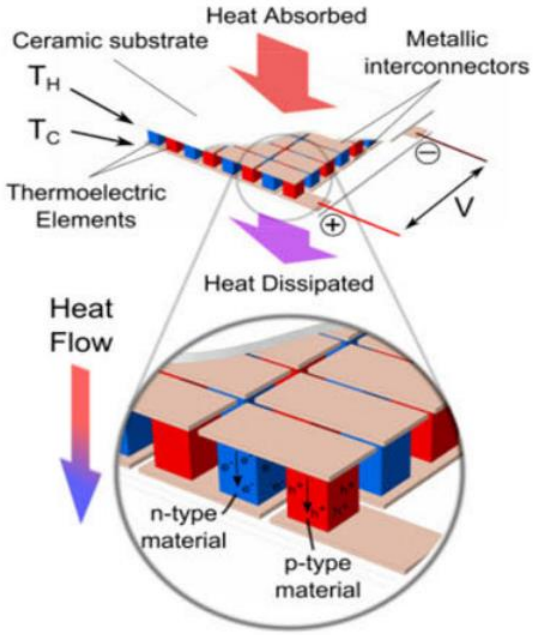

Figure 1.8: The TEM scheme and operation [24]

TEMs have attained massive attention over the more recent decades due to their advantageous nature of converting thermal energy directly into electrical energy, having no moving parts, no noise, having a scalability, high reliability, long lifespan, high flexibility in applications, minimal maintenance, and compatibility with the environment [21].

Another notable point worth mentioning in the field of TEGs, is that devices, components, and materials in their infancy are generally expensive. However, as the device becomes more popular through possible technological advancements, the demand for them increases and this results in a price drop [25]. A typical example of this occurrence, in industry, was the reduction of the cost of carbon fibre. Once the market demand increased, the product became more accessible and at lower costs. Today, carbon fibre is sold commercially at reasonable prices due to its high demand. While a TEM is currently expensive for a small unit, it can generate

microwatts of power, and this has already developed and gained traction in this era of ‘green’ energy alternatives [25].

TEG performance is derived empirically, and the performance curves provided by the manufacturer of the TEM does not provide design equations. This is because TEGs are an innovative and relatively new field of research and is constantly evolving. Further information on the choice of TEM used in the presented research is provided in Chapter 1.2.2.

1.1.8 Temperature measurement devices in electronics.

Temperature sensors are commonly used devices and are of paramount importance in everyday temperature control and monitoring systems. In this concise sub-section, the different types of commercially available temperature sensors, their advantages, disadvantages, their applications and working principles are explored.

Due to recent technological advancements, temperature sensors have become a critical building block in electronic systems, to keep devices within an acceptable operating performance. Temperature measurement devices may trigger a programmed function to heat up or cool down and hence, alter performances of systems. Therefore, thermal malfunctions such as batteries catching alight or damaged components may be prevented [26].

Other common applications of temperature sensors are in motors, home appliances such as kettles, refrigerators, air conditioning, computers, motorsport vehicles, food production, alcohol breathalysers and fire detectors [27].

State of the art high precision temperature sensors have led to technological advancements in automated machines, telecommunications industries, artificial intelligence, smart valves, smart buildings, fire detectors and IT services [28].

1.1.8.1 Thermocouples

The most used temperature sensors are thermocouples, due to the advantages they hold such as being self-powered, having a wide temperature operating range and fast response times. The working principle by which thermocouples operate is the Seebeck Effect (previously explained in chapter 1.1.8 above). The voltage difference produced from the temperature gradient of two dissimilar conductors can be measured and used to calculate the resultant temperature. A picture of various thermocouple type temperature sensors may be seen in Figure 1.9.

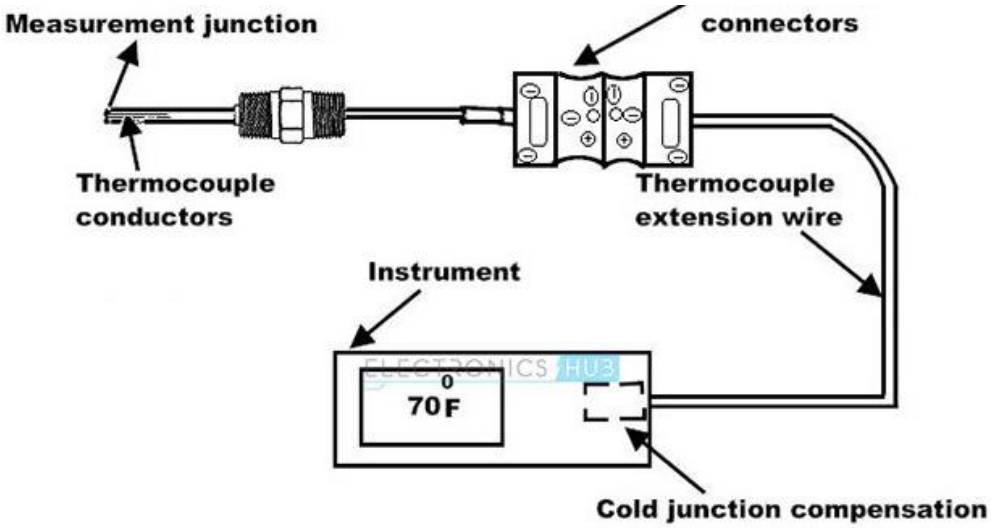

Figure 1.9: Illustration of thermocouple type temperature sensors [29]

Each type of thermocouple, used in temperature sensors, have a pair of conductor alloys, a temperature range within which it can read temperatures and a sensitivity factor. One of the main drawbacks of thermocouples in measuring temperatures is that they have a small output voltage [30]. Thermocouples offer temperature measurement range of -270° to 2300°C which is greater than other types of sensors [31].

1.1.8.2 Resistance temperature detectors (RTDs)

RTDs are temperature sensors, commonly made from platinum, which measure temperatures based on the change of resistance in a metal undergoing temperature fluctuations [30]. RTDs are preferred over thermocouples since they have a high level of accuracy, repeatability and have near linear response properties [32]. An image of an RTD type temperature sensor can be seen in Figure 1.10.

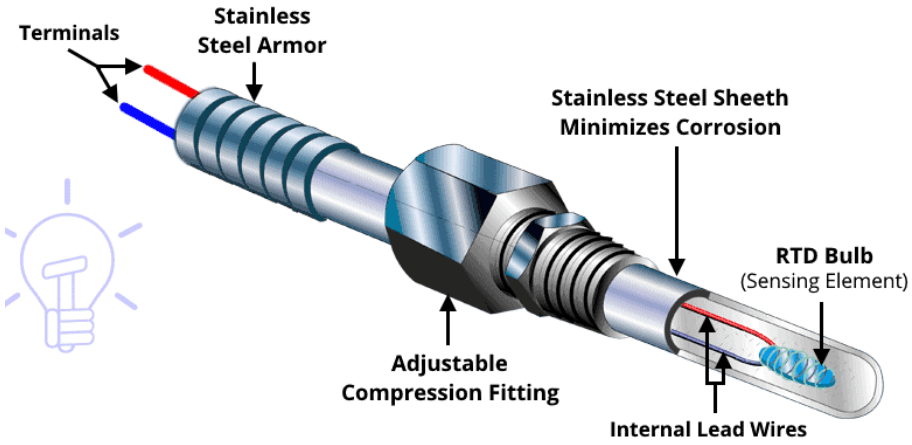

Figure 1.10: RTD type temperature sensor [29]

1.1.8.3 Thermistors

Thermistors are like RTDs since the change in resistance is used to calculate the temperature fluctuations. These temperature sensors are made of ceramic or polymer material and hence, are cheaper than RTDs [30]. The main advantage of thermistors is that they are highly sensitive and ideal for uses in the automobile and electronics industry. Thermistors are small and durable but do not have a linear characteristic behaviour which makes calibration a difficult task [33]. A picture of various thermistor type temperature sensors can be seen in Figure 1.11.

Figure 1.11: Picture of various thermistor type temperature sensors [29]

1.1.8.4 Semiconductor based integrated circuits.

Semiconductor based temperature sensors are primarily incorporated in integrated circuits (ICs). These sensors monitor temperature fluctuations by utilising two identical diodes that have temperature sensitive current vs voltage behavioural characteristics. These temperature sensors provide a simple way for calibration since they offer a linear response. However, this comes with a draw-back of low accuracy and a slow response time with a narrow temperature range of -70°C to 150°C [34].

In microprocessor-based systems, a digital output temperature sensor provides reliable monitoring of temperature fluctuations within an approximate range of -50°C to 150°C with a ±0.5°C accuracy [35].

One such precision IC temperature sensor series is the LM35, whose output voltage is linearly proportional to the Celsius temperature. The proposed design utilises 4 LM35DT temperature sensors and the design aspects and calibrations are further evaluated in chapter 3. The LM35DT offers a linear scale factor of $10.0\frac{mV}{^{\circ}C}$. This makes calibrating the sensor for the purpose of this work very easy. Figure 1.12 illustrates a digital output temperature sensor in the LM35 series.

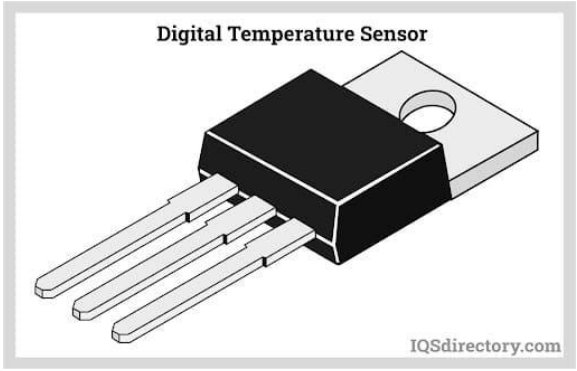

Figure 1.12: Illustration of a digital output temperature sensor in the LM35 series [36]

1.1.9 Photovoltaics

Solar cells or photovoltaic (PV) cells put together become a device capable of converting light energy directly into electrical energy by means of the photoelectric effect [37]. Presently, photovoltaic cells efficiency is at 12-19% under promising conditions [38].

Green [39] refers to the solar cells as a "quantum device" that exchanges photons for electrons. Ideally, for each photon reaching the device, one electron flows through the load. However, this ideal scenario seldomly occurs due to incoming photons being reflected from the photovoltaic cells or being absorbed by metal in the cells, where the photon's energy becomes heat. Due to this increase in operating temperature, the PV panels efficiency is generally low and results in degradation of PV panels. It is reported that for each 1°C rise in operating temperature, the efficiency of the PV panel is reduced by 0.5% [40]. Another limiting factor is the high manufacturing and installation cost [41]. Since PV panels are exposed to the elements, they are at a higher risk of damage and ware. External factors that cause significant degradation of PV panels are dust accumulation, water-stains, and bird droppings. The system's internal factors said to reduce overall performance efficiency by 10-25% are losses due to the inverter, solar module soiling due to debris and dust, and wiring [42]. Figure 1.13 illustrates the PV working principle. Figure 1.14 shows the damage to a PV panel from hail. Figure 1.15 shows dust accumulation on PV panels in contrast to clean PV panels.

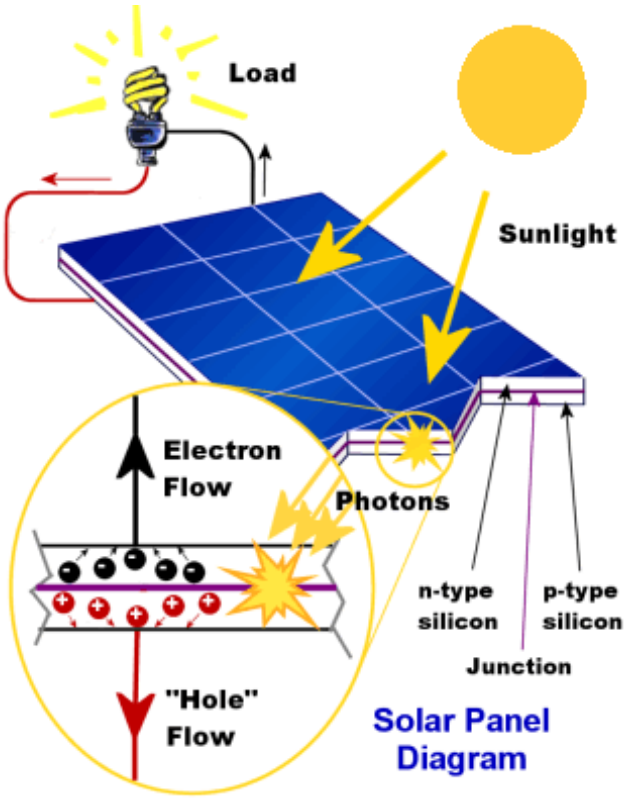

Figure 1.13: Image illustrating the photovoltaic panel working principal [43]

Figure 1.14: Picture of the damage to solar panels due to a hailstorm [44]

Figure 1.15: Picture of soiled solar panels in contrast to clean solar panels [45]

Traditional PVs convert a relatively small section of the sun's light spectrum into power, which is the main limiting agent for its efficiency. PVs that are made of silicon material converts a small range of light wavelengths into electricity, while ignoring the longer or shorter wavelengths. This acceptable range of visible light waves measures between 400-700 nanometres (nm) whereas the sun's light spectrum contains wavelengths of between 300-2500 nm. Wavelengths below 400nm simply pass right through the cells whereas wavelengths longer than 700 are too high in energy and are not absorbed entirely [46]. Figure 1.16 illustrates the solar spectrum in comparison to the acceptable visible light region.

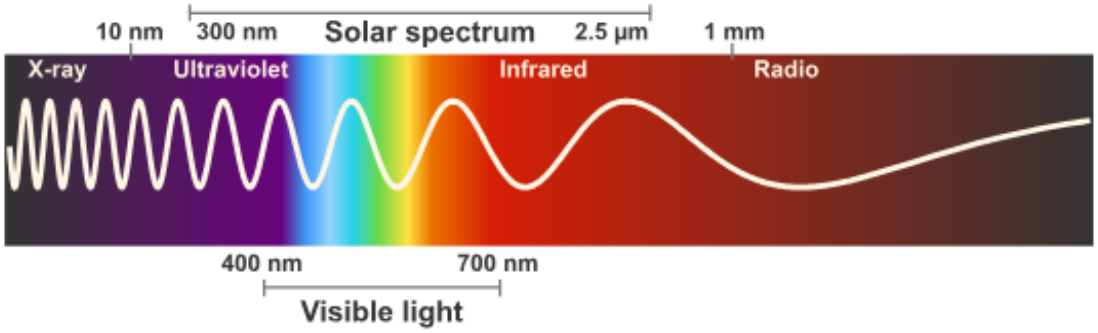

Figure 1.16: Image illustrating the solar spectrum in comparison to the acceptable visible light region [47].

1.2 An investigation into harvesting solar energy using Thermoelectric generator-coupled IBR sheeting.

1.2.1 Aim and objectives

The aim of this research is to investigate a potential application of the proposed solar thermoelectric generator, coupled with IBR sheeting and positioned vertically. The system generates power while keeping the assembly and construction of the system onto an application such as a warehouse, simple, practical, and minimalistic. A possible application may be the sides of a large warehouse in hot regions. To achieve this, outdoor solar experiments were conducted to determine the temperatures and temperature gradients the configuration may experience in operation. The data collected established parameters for the laboratory experimental setup. The experiments characterised the power output of the units. The effect of the colour of the metal sheeting and the electrical connection arrangements for maximum power output were investigated. The TEG is tested in the ideal vertical position, devoid of most thermal variables and hence would not reflect results that would be obtained in real application. Applications of different orientations and geographical locations require further investigation.

1.2.2 Research methodology

The IV curve generation method (later explained in chapter 2.4.1) is used to read the parameters required to calculate P_{max}. The effect of the following variables on P_{max} are investigated:

i. The effect of roof sheeting colours on power output i.e., Galvanised, black, and white.
ii. Scalability in series vs. parallel electrical arrangement for optimum power output.

Table 1.1: Both TEMs used in the experiments are of the same size and number of junctions.

TEG Sample	Size(mm)	Number of junctions
TEM1	40×40	127
TEM2	40×40	127

The aforementioned choice and sizing of the TEM is further elaborated on in Section 3.2.2.3 and the characteristic curves, found empirically, may be seen in Appendix A.

Galvanised, white, and black were chosen as the test colours because the proposed research may have a possible application of generating power on the sheeting of large warehouses. These warehouses are either galvanised or painted white to help cool the warehouse. The colour black was introduced to test whether coating the sheeting black would enhance the power output.

While the power output per TEG tile is small in magnitude, the proposed configuration lends itself to the coupling of multiple units to increase power output. The current work shows potential for the use of TEGs in this application. Through further investigation, refinement and cost analysis, the system may prove to be a practical method of solar energy harvesting. For purposes in future research, the expected solar output power when the system is scaled up could also be predicted and compared to the output power generated by PV solar panels of the same scale.

2 Literature Review

This chapter reviews the existing literature in relation to the field of TEGs. The growth and progression of the TEG industry is highlighted, together with any major similarities and differences these literatures have with the proposed research concept and methodology herein. This section additionally includes subsections exploring potential TEG applications beyond solar energy harvesting.

2.1 Automobile Industry:

In vehicle internal combustion engines, chemical energy provided by the fuel is momentarily converted to mechanical energy in order to run the vehicle, an estimated 40% of this energy is lost as exhaust gas emissions [48]. These exhaust gas emissions cause an increase in greenhouse gases that are proving to be detrimental to the environment [49]. Due to these resulting negative environmental effects, the use of biofuels and electric vehicles have increased, but these applications are used for light motor vehicles. On the contrary, Heavy-duty motor vehicles and industrial transportation continue fuel consumption, hence, more innovative solutions need to be explored [50].

Research has been conducted in the potential use of TEG systems as a means of thermal energy recovery in the automobile industry, one such application is a TEG system installed on light-vehicle exhaust pipes [22].

Cao, et al. [22] states that when using 36 thermoelectric modules in the TEG system, the maximum open circuit voltage obtained was 81.09V, the corresponding power output was 13.08W and the thermoelectric power generation efficiency was found to have been optimised to 2.58%. Thacher, et al. [51] designed and built a TEG using 1080 carbon steel and it was found that reducing coolant water in the engine significantly increases the conversion efficiency of the TEG. Figure 2.1 shows a schematic of the HP-TEG structure proposed by Cao, et al where (a) top view, (b) front view.

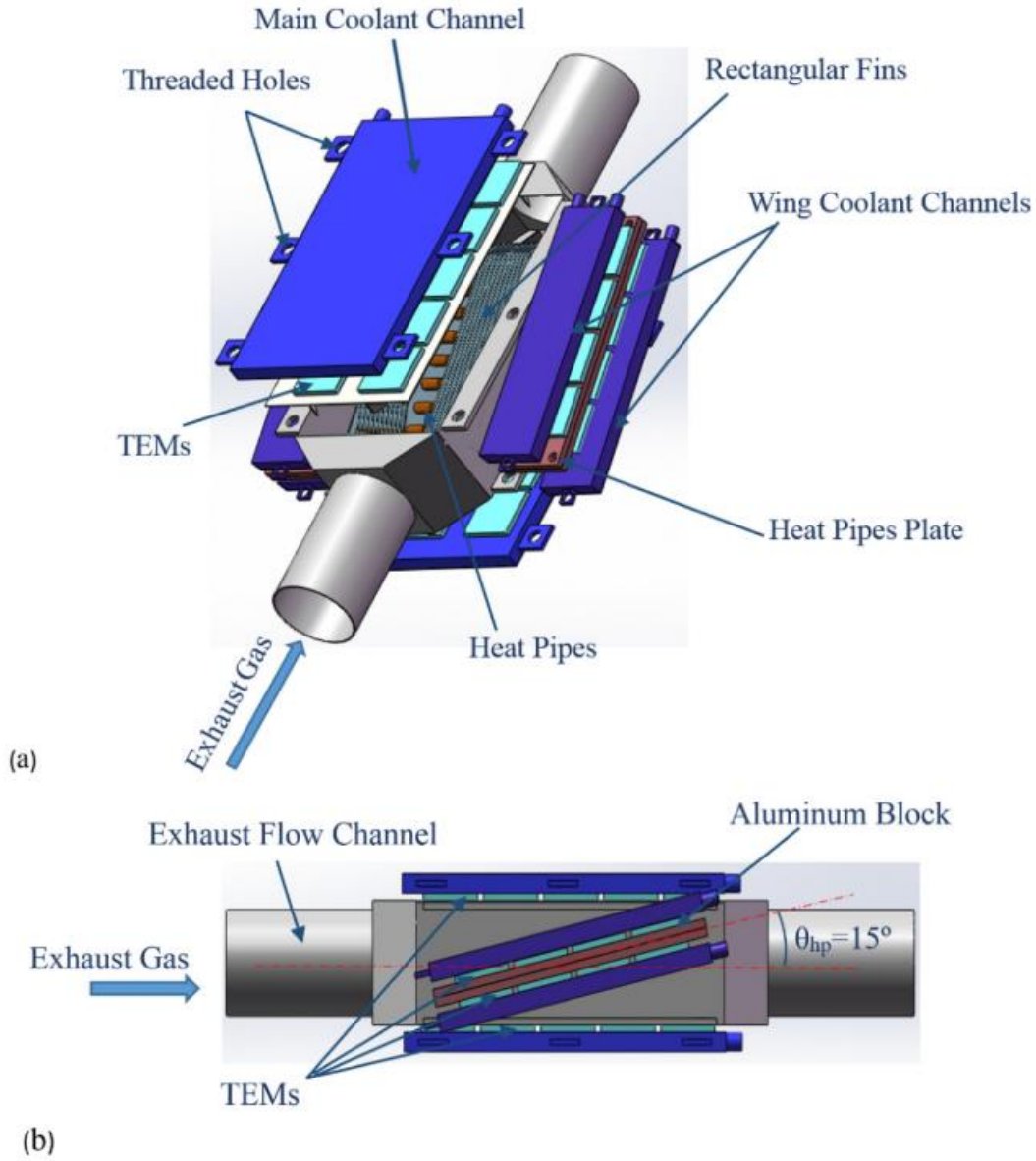

Figure 2.1: Schematic of the HP-TEG structure [22]

Liu, et al. [52] designed a TEG system of four TEGs, whose heat source was an automobile exhaust and was cooled by water. The maximum power extracted was 944W, at a temperature difference of 240°C, an open circuit voltage of 201.7V and a current of 8A. The overall system efficiency was also increased from 0.28% to 1.85%. Figure 2.2 is an illustration of the HTTEG system proposed.

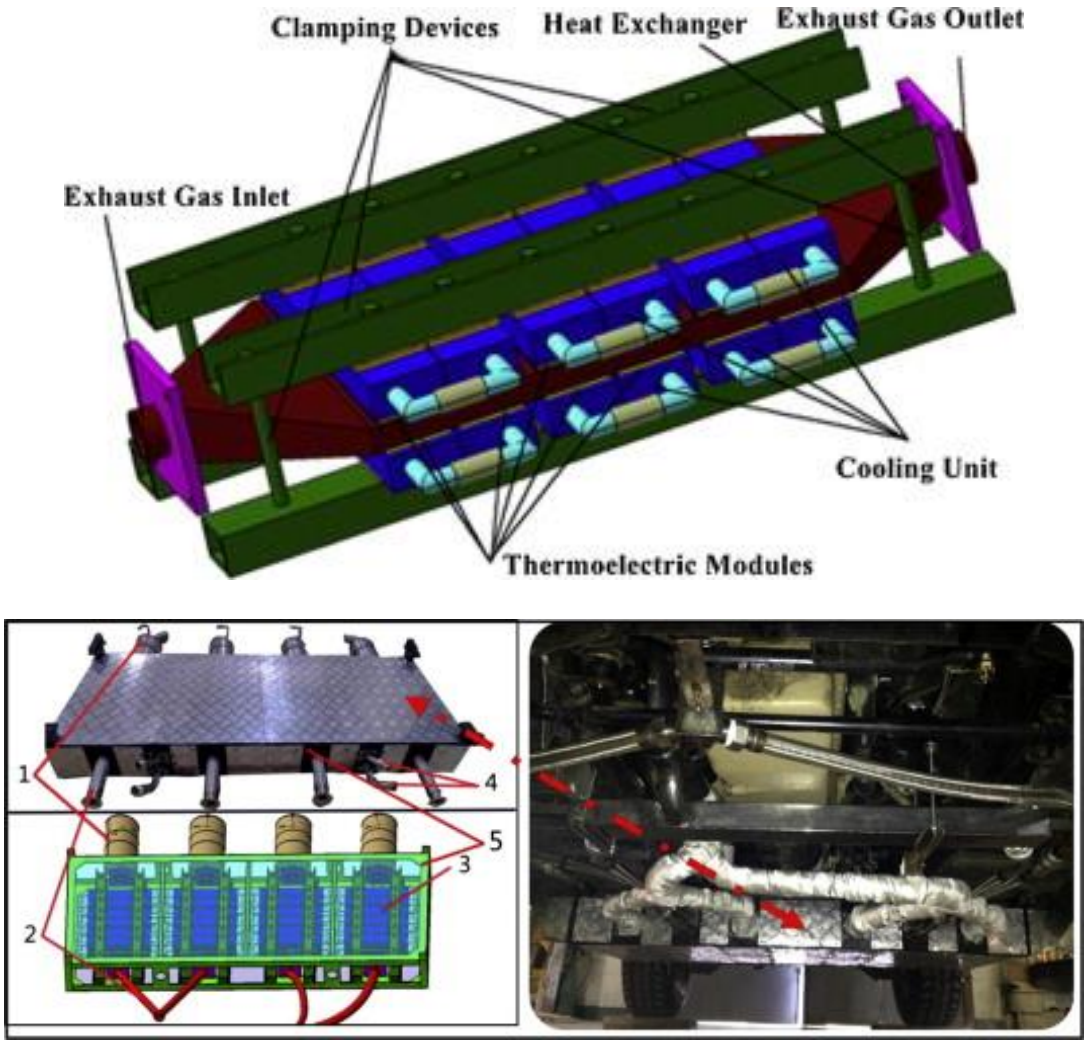

Figure 2.2: The HTTEG system [52]

Chen, et al. [53] proposed a segmented converging TEG which was optimised using a variable converging angle within each segment in the heat exchanger. His mathematical model proved that the output power can be increased by 12.5% when the air temperature is 500 K at certain fin converging angles. Figure 2.3 shows the model of the segmented converging TEG by Chen, et al. [53]. (a) Shows the heat exchanger and heat sinks, (b) Shows the fins in the design.

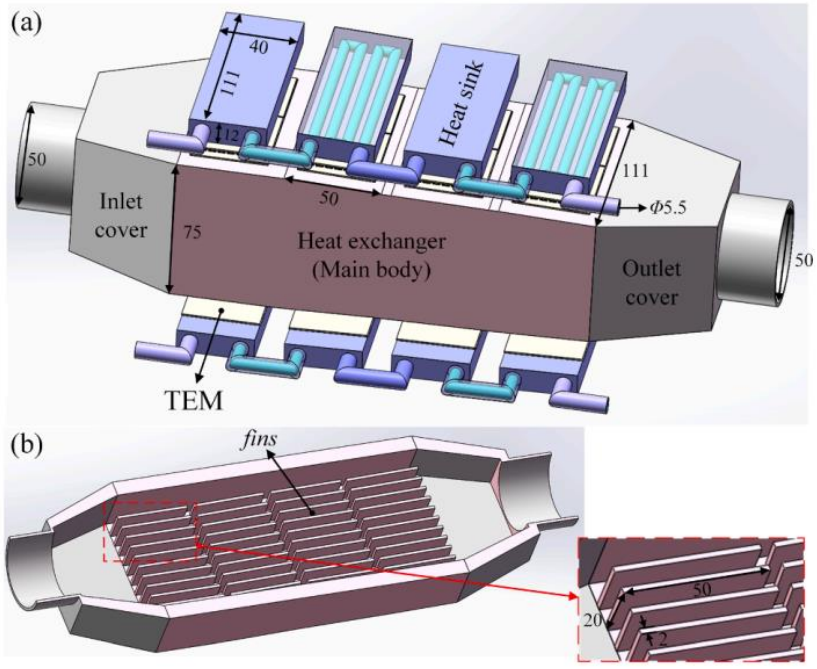

Figure 2.3: Model of the segmented converging TEG system [53]

Kushch, et al. [54] developed and tested a TEG system containing 72 modules for heavy-duty diesel trucks, designed to replace the shaft driven alternator. It was found to generate $1kW$ Power at $30V$ DC for nominal engine operation.

2.2 Solar thermoelectric generators (STEGs)

Thermoelectrical materials are a type of material that can generate a voltage when a temperature gradient exists. With the help of a solar absorber and a heat sink, a temperature gradient can be established and when thermoelectric materials are introduced in between, power is generated. These systems are referred to as Thermoelectric Generators (TEGs). Solar Thermoelectric generators (STEGs) are TEGs whose source of heat is the sun. The main advantage of STEGs, aside from their 'green' nature, is that they can utilise the entire solar spectrum in contrast to PV's that utilise the wavelengths of the spectrum above the band gap of the material used for the cell [55].

2.2.1 STEGs and vacuum enclosed hybrids

Enclosing a TEG within a vacuum eliminates the majority of heat loss due to convection through the air, thus increasing system efficiency. Wang, et al. [56] proposed one such vacuum-flat plate STEG system with high thermal concentrators and achieved a maximum efficiency of

4.6%, which is 7-8 times more efficient than previous flat plate STEG's reported. Figure 2.4 illustrates the vacuum-flat plate STEG designed by Wang, et al.

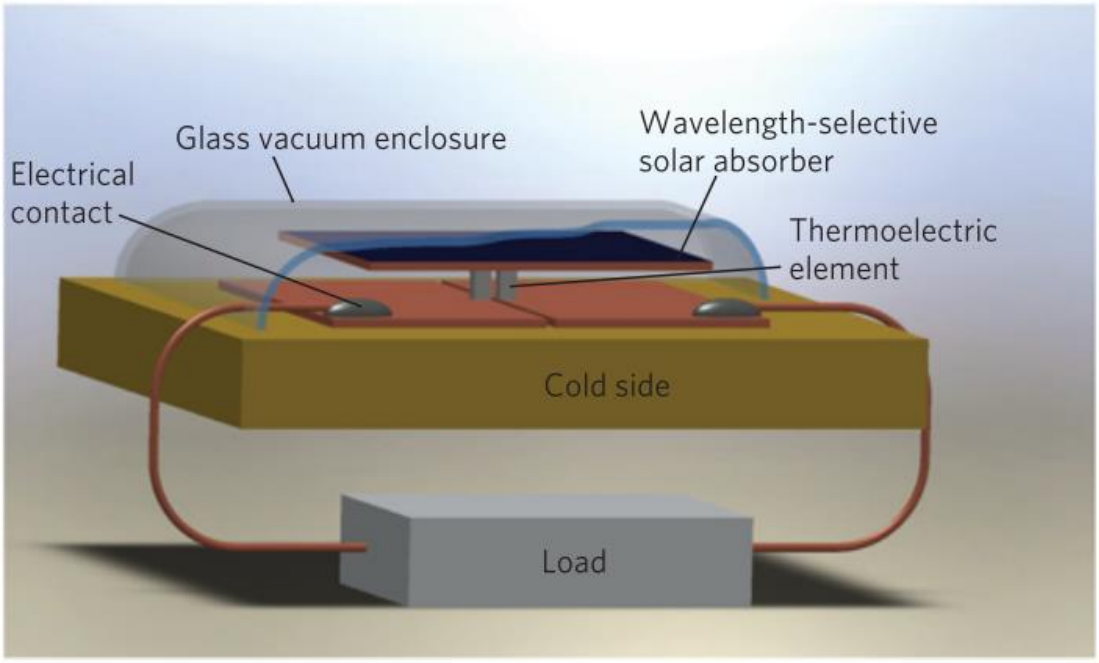

Figure 2.4: The vacuum-flat plate STEG [56]

Lv, et al. [57] developed a solar heat pipe-vacuum hybrid STEG system comprised of a selective solar absorber, TEMs with optimised thermoelectric material with device and heat management integration which produced a maximum electrical efficiency of 5.2%. This design was intended for water heating and domestic applications. Figure 2.5 shows the STEG system model.

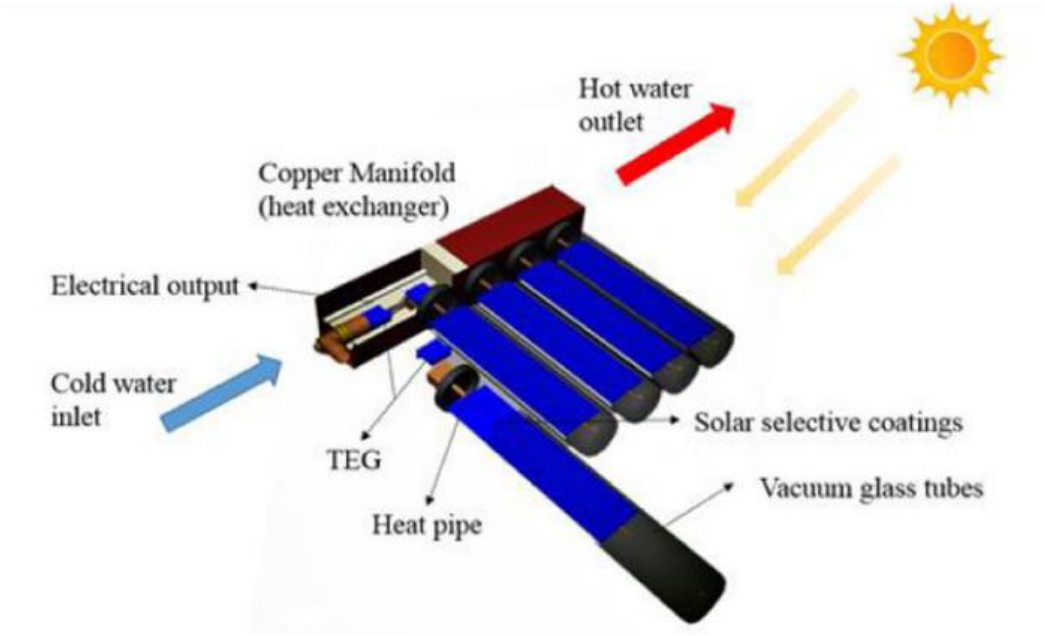

Figure 2.5: The STEG system model [57]

2.2.2 Concentrated Solar Thermoelectric Generators (CSTEGs)

Concentrated Solar Thermoelectric Generators (CSTEGs) are basically STEGs with an enhanced feature that concentrates the heat onto the hot side where the incident solar flux heating the absorber can be controlled or varied to increase efficiency by encompassing parabolic troughs, parabolic dishes or optical lenses [58]. Additionally, due to delayed thermal response, CSTEGs can continue to generate power even if the clouds partially block off the sun [59].Study into CSTEGs intended to power a spacecraft was pioneered by Telkes [60], who achieved an optimal efficiency of 3.35% by concentrating sunlight using a 50× lens. In more recent times, the interest in researching into this field propelled forward innovative technologies to enhance conversion efficiency and applications worldwide.

Kraemer, et al. [61] reported a new record-breaking efficiency of 9,6% and a power output of 0.5W at an absorber temperature of 560-580°C derived from a CSTEG system whose performance was achieved by using segmented thermoelectric legs, glass vacuum enclosure, spectral-selective solar absorber of high temperatures and a combination of thermal and optical concentration. Figure 2.6 shows an illustration of the model of the proposed CSTEG.

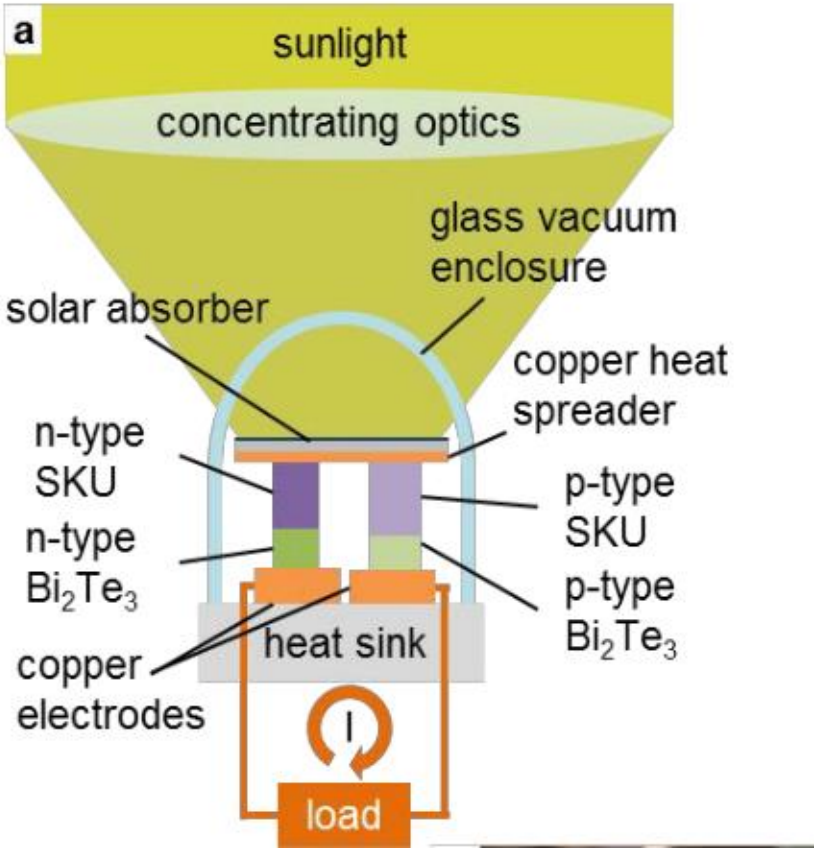

Figure 2.6: Model of the proposed CSTEG [61]

Mgbemene, et al. [62] designed and tested a compound parabolic concentrator (CPC) and a TEM system for power generation. It was found that the TEG system could generate power to sustainably run a small device. Figure 2.7 displays a schematic diagram of the hybrid CPC/TEM system.

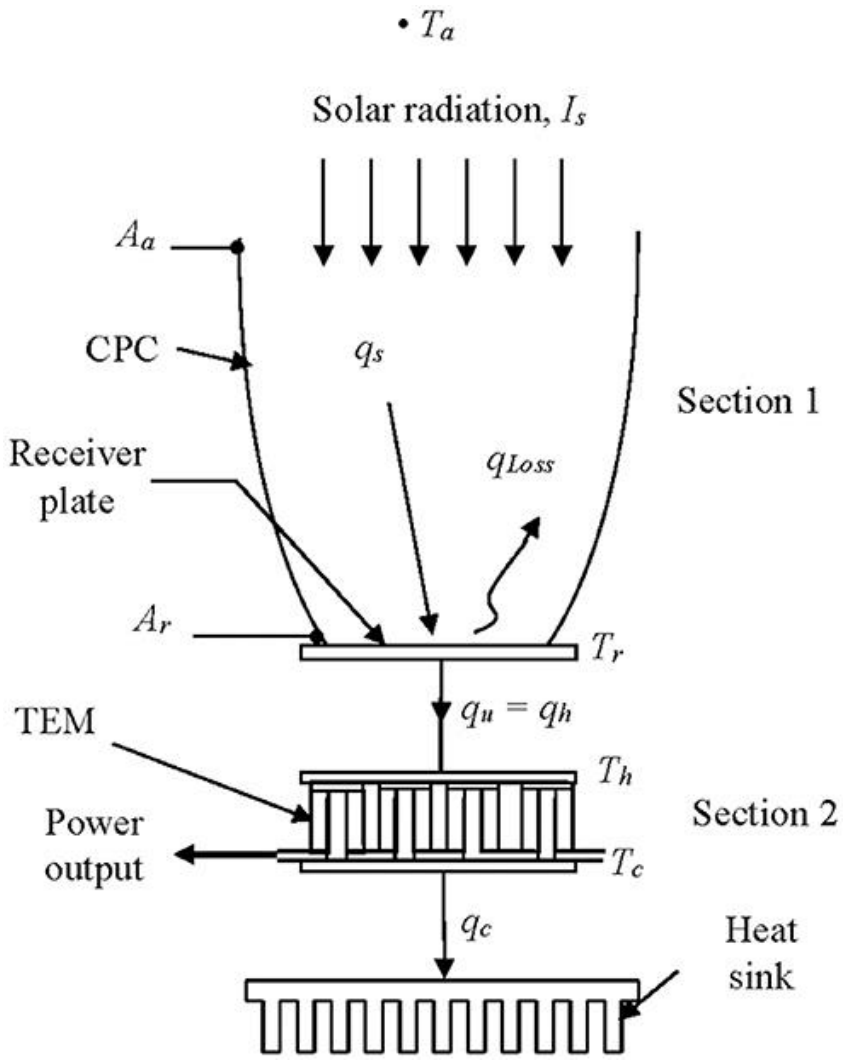

Figure 2.7: The hybrid CPC/TEM system [62]

Tzivanidis, et al. [63] designed and simulated a small parabolic trough collector (PTC) for different operating conditions. Their goal was to predict an efficiency and an analysis on the heat transfer that occurs. The efficiency was found to be more than 75% which proves a high collector performance, under high temperature conditions.

Lashin, et al. [64] designed and tested a TEG system using a partial illumination technique. The performance of the TEG under partial illumination with different percentages of illumination covering, as well as various light intensities (Concentrated light produced by a Xenon-Lamp solar simulator with 12× and 105× intensities) and the effect of different Peltier tile sizes was investigated. It was found that the Peltier tile which contains most P-N junctions resulted in a larger open circuit voltage (Vo) under both low and high light concentration levels. The highest power was also found to be generated under the highest light intensity, by the medium sized Peltier tile whose number of junctions are the highest (sample B). Lashin's work proved that

the number of P-N junctions of thermoelectric materials in a Peltier tile and the power generated is directly related, and that the higher the light intensity, the higher the power generated.

Lashin et al. [64] employed a water-cooled heat sink, while the proposed system opts for a simpler and practical solution i.e., natural convection on a vertical plate and an aluminium heat sink. Lashin et al. tested a sample with an equivalent number of junctions (sample B-127 junctions) as used in the presented research.

Figure 2.8 shows photo(a) and sketch (b) of the experimental set up conducted. Partial illumination is applied on the hot side of the TEG and the Peltier tile is thermally connected to the heat sink which is immersed in water flowing at a constant temperature of 23°C.

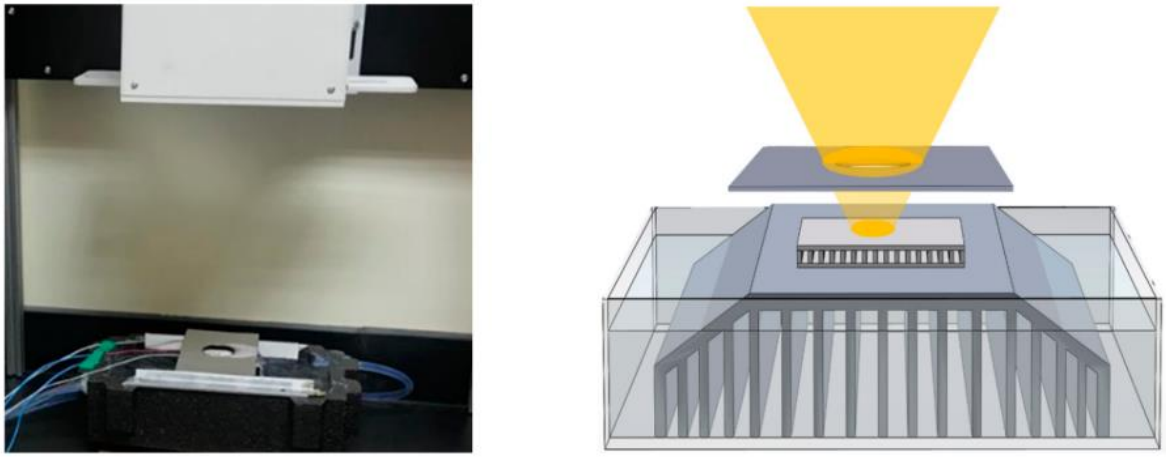

(a) (b)

Figure 2.8: The experimental set up conducted which applies the partial illumination technique [64]

An optimal relationship between receiver area and aperture (variable opening, through which light enters) area was established by Kumar and Shukla [65] successfully. Amongst the concentration ratio, an optimised rim angle was also calculated to achieve a maximum solar collection efficiency of the parabolic trough concentrator.

A hybrid direct absorption flat plate solar collector integrated with a TEG was modelled and analysed under different optical concentration ratios by Moh'd A, et al. [66]. The results showed that the output electrical power increased by 19.13% under a concentration ratio of 20 suns.

Another CSTEG design set up with Fresnel lens concentrating solar thermal energy on a TEG with Aluminium fins on the cool side was designed and experimented by Jeyashree, et al. [67]. The cool side heat sink encompassed a nano-composite material, and the thermal adhesive

contained a nano-PCM (Phase change material) which changes from liquid phase during the day to solid during the night, thus storing heat. This TEG device can then use latent energy to generate power at night devoid of the sun or a heat source. The maximum output voltage harvested at night was 89mV. During the day, a maximum temperature difference of 96°C, a maximum current of 84.9mA and a 0.65V was generated from a single TEG.

The peak efficiency obtained was 7.17%. The device used Multimeters, thermocouples, and a temperature monitoring system to explore the parameters mentioned. An estimate combination size of 44 TEGs in series and 66 in parallel to power up a 70W rating LED streetlight was also established. Figure 2.9 shows the hardware design of the CSTEG system. Figure 2.10 displays a graph of temperatures established by the TEG throughout the day.

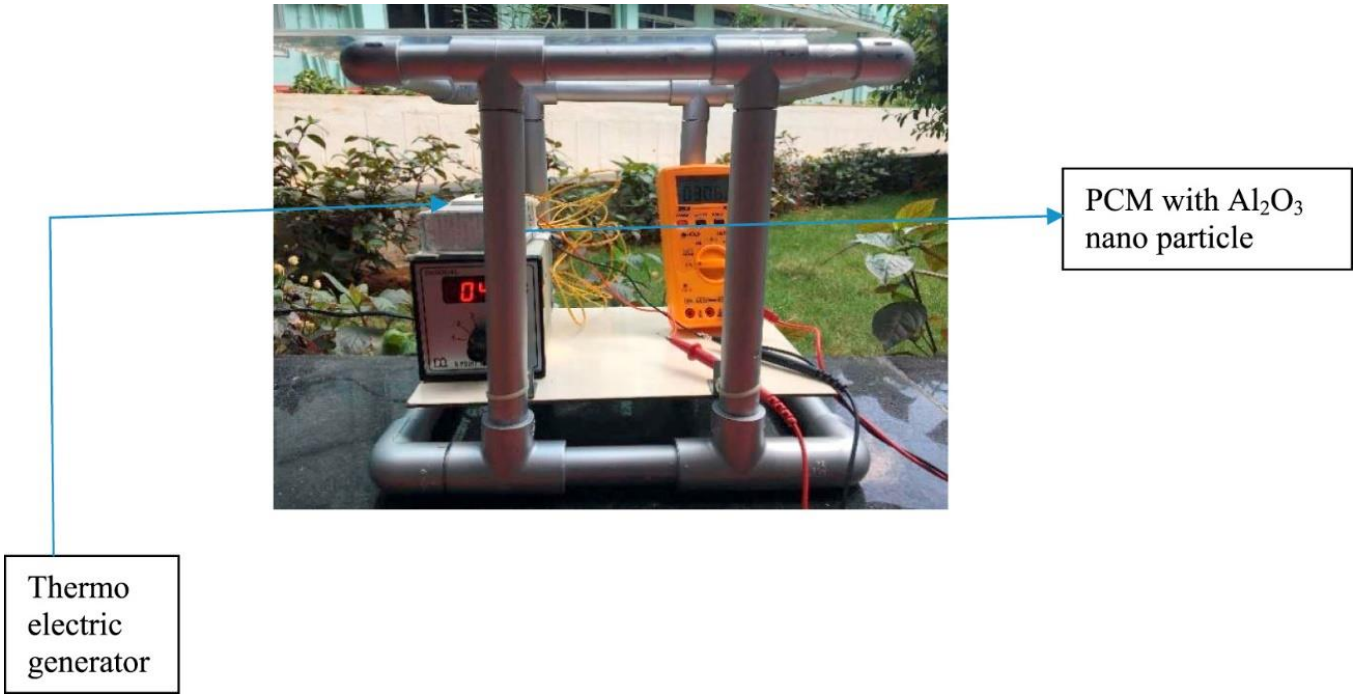

Figure 2.9: The hardware design of the CSTEG system [67]

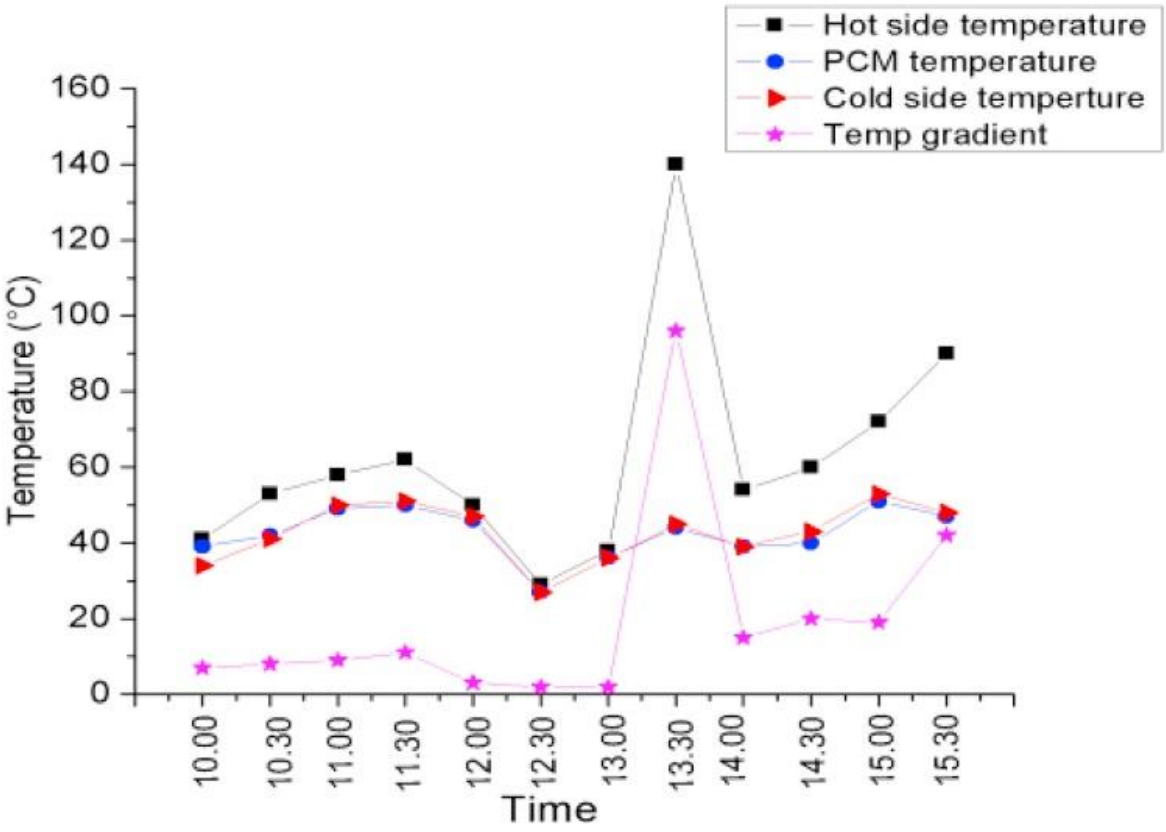

Figure 2.10: Graph displaying temperatures of TEG elements throughout the day [67]

Figure 2.11: The solar parabolic concentrator coupled with the TEM [68]

A similar study to Lertsatitthanakorn, et al was adopted by Eswaramoorthy and Shanmugam [69]. A parabolic concentrator STEG using a low-cost, recycled parabolic dish concentrator, lined with Aluminium sheeting and coupled with many TEMs, which are connected in parallel or series, depending on the voltage requirement, was presented. The hot and cold side were rigidly attached to metal plates. The hot side was painted with a dull, matt black paint and connected facing downward, so as to absob all the radiation concentrated by the dish reflector. A numerical analysis was adapted to study the possibilities of meeting an estimated rural house annual energy demand. The daily energy demand was met by a TEG capacity of 120W and the parabolic dish concentrator efficiency was found to be 80%. Furthermore, an excess of 24% energy was generated during peak solar radiation hours and this could be stored for night or emergency usage. Figure 2.12 shows a diagram of the CSTEG which was numerically tested.

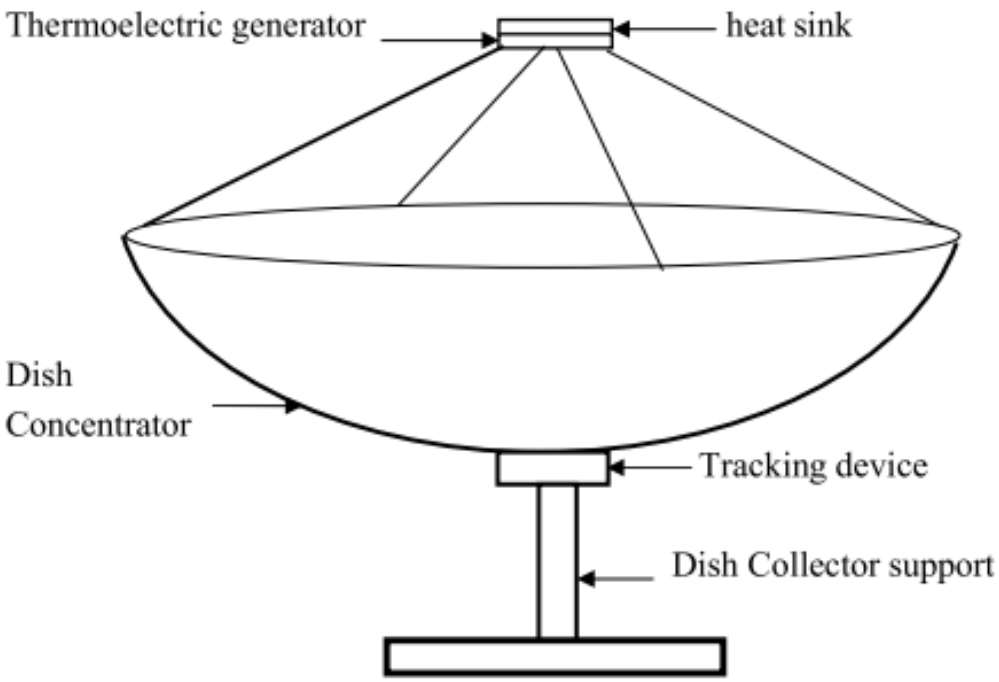

Figure 2.12: The CSTEG numerically tested [69]

Cheruvu, et al. [70] experimentally studied the temperature variation of a CSTEG using Fresnel lenses, a spectrally selective solar absorber, and a vacuum enclosure. A set of 3 TEG's connected in series wielded a maximum output power of 0.91W and a peak efficiency of 2.21% under a hot side temperature of 369°C.

Figure 2.13 shows (a) The experimental set-up and arrangement of the CSTEG, showing Fresnel lens, the vacuum chamber housing, (b) The schematic illustration of the set-up, (c) The schematics of TEM arrangement where TEMs are connected in series under optical concentration, and (d) The vacuum chamber.

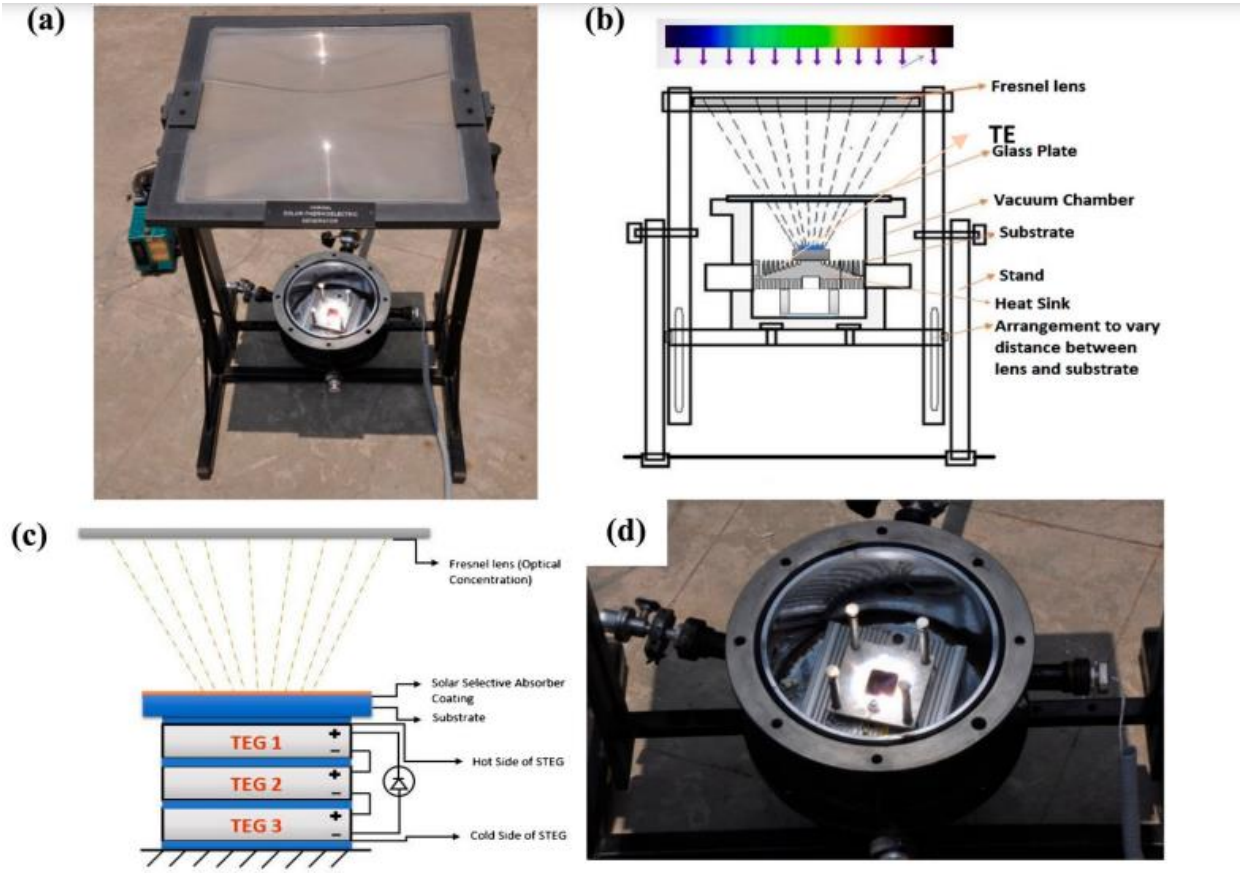

Figure 2.13: Experimental set-up and arrangement of the CSTEG [70]

Amatya and Ram [71] conducted experiments on a CSTEG that achieved 1.8W output power from 2 TEMs housed in a metal enclosure. The TEG system comprised of a solar concentrator, heat sink, selective surface, Fresnel lens and a thermal felt. Figure 2.14 shows (a) The CSTEG experimental set up, (b) The schematic of the enclosure housing the TEG, where a Fresnel lens is utilised to increase the solar flux concentration.

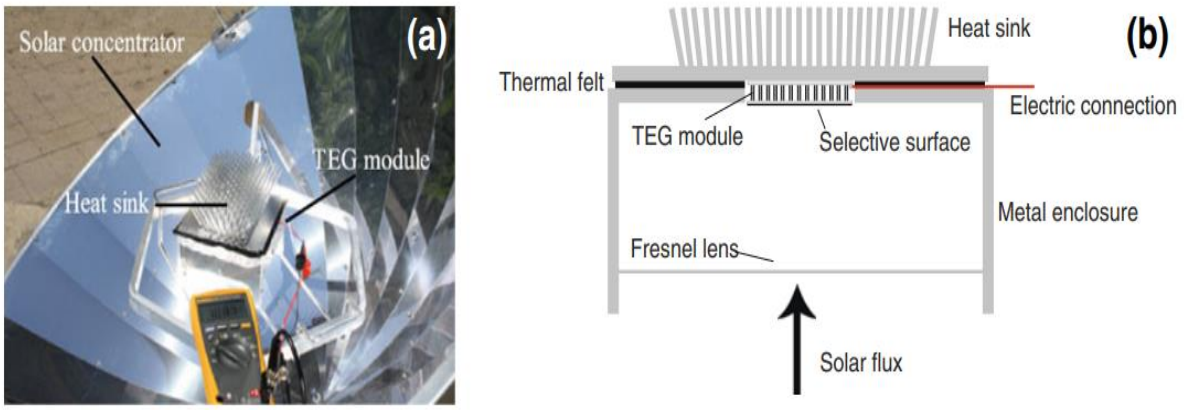

Figure 2.14: Shows the CSTEG experimental set up and schematic [71]

2.2.3 Solar thermoelectric co-generators (STECG)

A Solar Thermoelectric Co-Generator (STECG) was piloted by Zhang, et al. [72] to supply heat and electric power simultaneously, by including TE modules to the heat pipe in vacuum solar collectors. The STECG was found to generate $0.19kW\ h$ and could heat up $300l$ of water at 55°C within a day. Figure 2.15 shows a picture of the design. The structure of an evacuated glass tube with TEM is displayed, where: (a) A glass tube with TEM, (b) cross-section schematic view of tube and (c) top view of heat pipe.

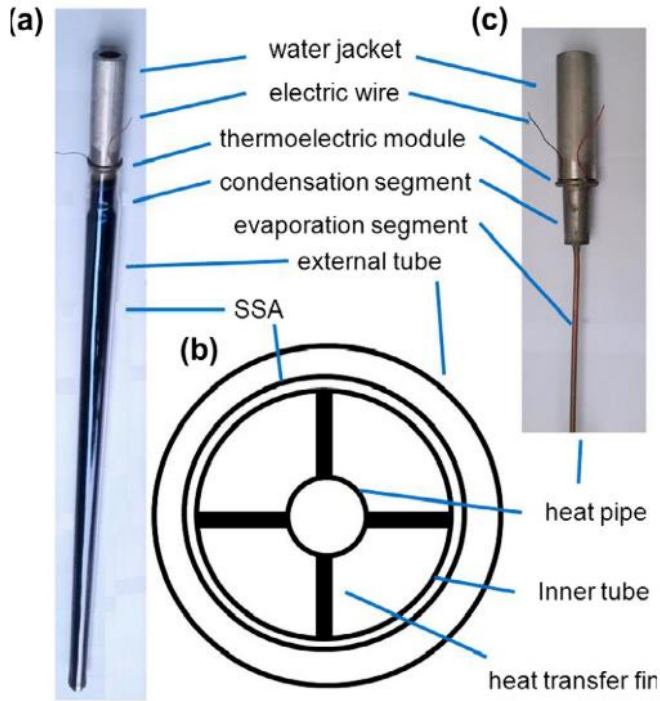

Figure 2.15: The STECG design [72]

2.3 Thermoelectric material study in TEGs

Contento, et al. [73] dives deeper into a comparative study of the thermoelectric materials found in thermoelectric modules which is an imperative characteristic that directly affects its' efficiency. TEG performance is derived empirically, therefore there was a need to test and investigate which configuration works best. The performance curves provided by the manufacturer of the TEM does not provide design equations. This is because TEGs are an innovative and relatively new field of research and is constantly evolving. Furthermore, the common applications of TEM involve applying a power to the TEM, which in turn allows for the TEM to be used in heating or cooling applications. However, we are testing the TEM for power generation by applying a temperature gradient and investigating the resultant power generated.

As per the above chapters 2.1 to 2.3, it is seen that the focus of existing literature and research is on optimising the efficiency and power output through impractical and costly methods. This research intends to shed light on an unexplored field, such as the relationship between the temperature gradient on the TEG system and the corresponding power output. Some factors that have not been discussed in existing TEG literature such as the comparison of the effect of roof sheeting with a black coating, in contrast to a neutral or commonly used colour, and its impact on the power output will be analysed and the electrical arrangement configuration that may produce the greatest power output in the scalability of the proposed TEG system will also be investigated.

Since the proposed design utilises renewable energy, the efficiency aspect may be less significant as opposed to if the energy source was being paid for, which would result in a large cost factor. Designs in the literature tend to establish multiple means to enhance TEG efficiency which are not practical design aspects for large scaled applications in the long run. Conversely, the proposed design explores an innovative, modular, and simple, yet practical application with a significantly low-cost factor in contrast to the existing literatures mentioned. The TEG is tested in the ideal vertical position, devoid of most thermal variables and hence would not reflect results that would be obtained in real application. Therefore, applications of different orientations and geographical locations require further investigation.

2.4 PV-TEG hybrid systems

PV cell efficiency majorly depends on whether the energy of the photons received by the PV, match the range of the band gap of the PV solar cells. Those photons holding lower energy than

the band gap is not absorbed at all and pass through the cells as dissipated heat energy. Photons that hold higher energy than the appropriate band gap are partially used, and the remainder energy passed through the cells in the form of heat as well [74]. These thermal losses in a PV cell due to heat dissipation cause an increase in cell temperature and therefore, a reduction in the cell efficiency. To utilise this heat dissipated by the PV cells and the wavelength range of the broad spectrum supplied by the sun, various designs of PV-TEG hybrids were introduced into the solar power industry as a means to increase efficiency and maximum power output [75].

An integrated PV-TEG hybrid system, as can be seen in Figure 2.16, comprises of a PV converter and a TEG in parallel arrangement. Radiations with energy within the appropriate band gap range are converted into electricity by the PV. The radiation is dissipated as heat by the PV are converted to electricity by the TEG. The PV is usually set up as the top component since it is required to absorb shorter wavelengths such as UV and visible light. The TEG is then fitted as the underlying component in the system, as it is required to absorb radiation of longer wavelength and the dissipated heat from the PV. The system then works as a unit to generate an improved power output [75].

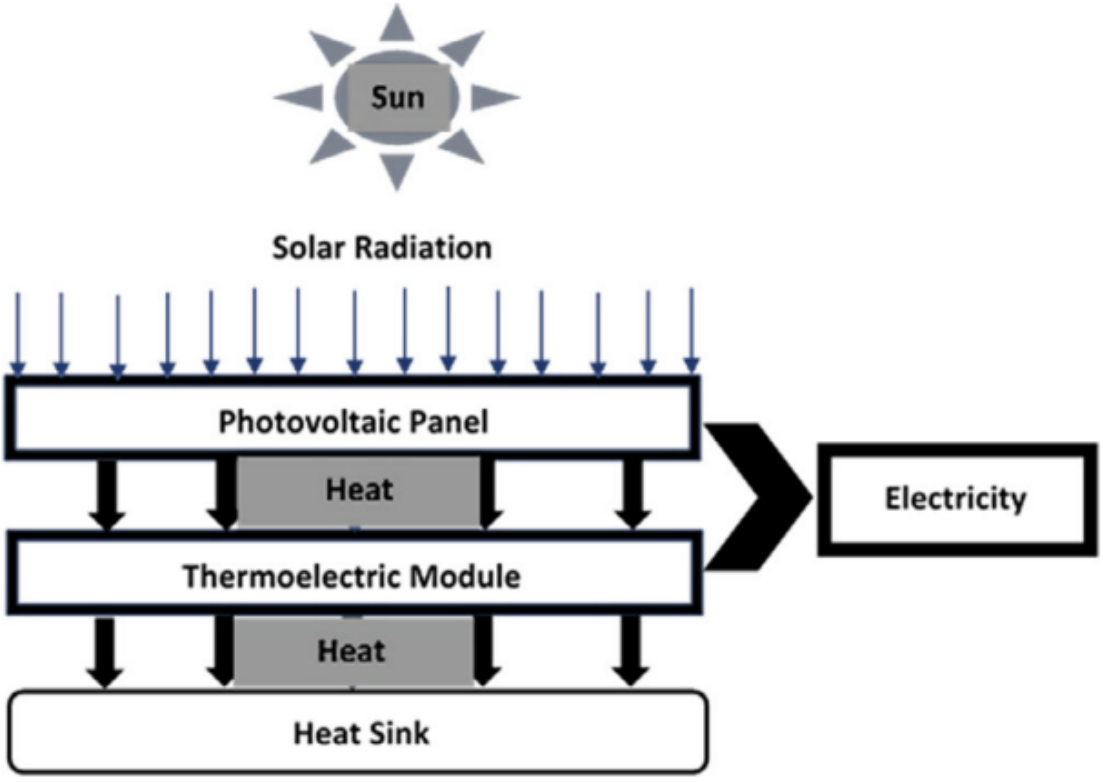

Figure 2.16: The integrated PV-TEG hybrid without a reflector [75]

By introducing a reflector in a PV-TEG hybrid system, the resultant power output can be enhanced further by efficiently making use of the entire solar spectrum. The solar radiation spectrum can be separated by means of a spectrum splitting technique using a wavelength segregator. The PV and TEG are arranged in a perpendicular configuration. In the hybrid system, the TEG enhances the overall electrical output power and increases the lifespan of the PV [76]. The resultant energy boost in the PV-TEG hybrid system could potentially reach up to 10% more, compared to that of a single PV cell [75].

Figure 2.17 displays the method of spectral splitting using a reflector such as the wavelength segregator for PV and thermal energy conversion. Figure 2.18 shows an image illustrating (a) The perpendicular configuration and set up of PV and TEG when a reflector is introduced and (b) Parallel arrangement without reflector. Components from both parts (a) and (b) are labelled as: 1-PV module, 2-TEG module, 3- Heatsink, and 4-Reflector. Figure 2.19 is an image which further illustrates the range of the solar spectrum that is split into components for thermal and PV energy conversion.

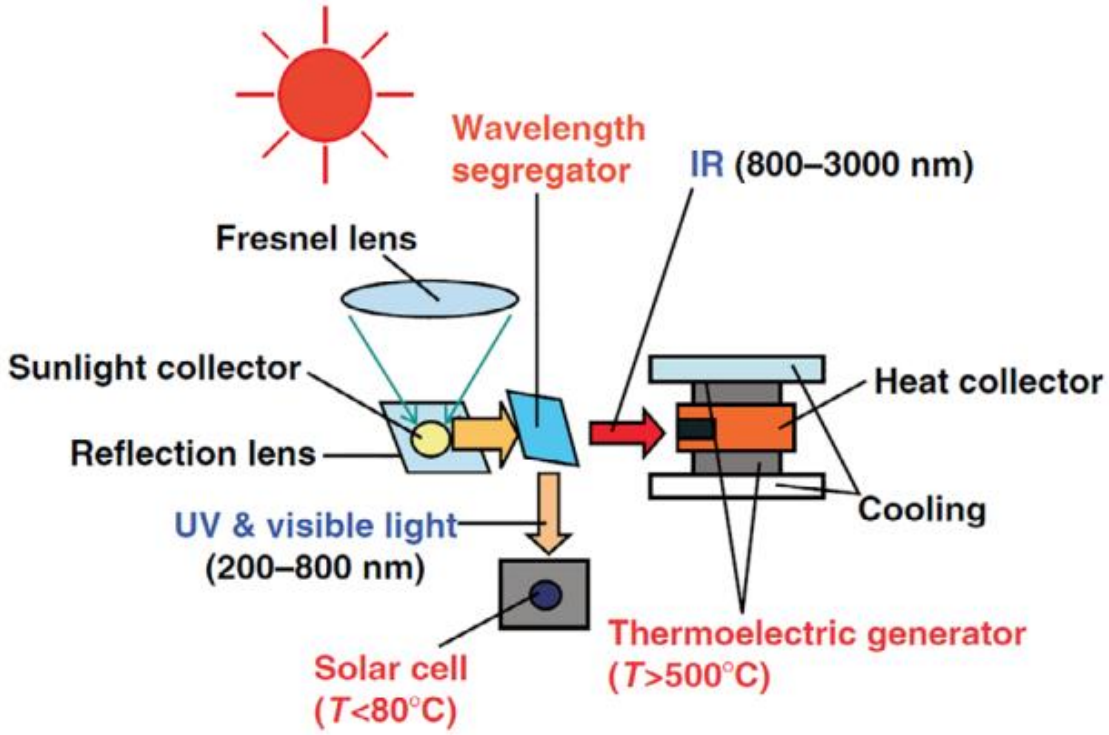

Figure 2.17: Method of spectral splitting using a reflector such as the wavelength segregator [75]

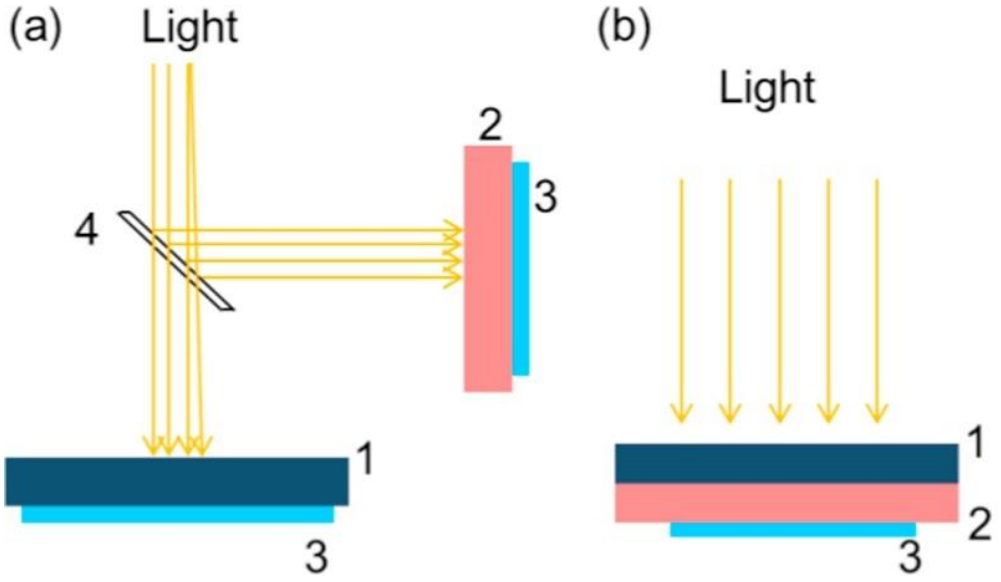

Figure 2.18: The perpendicular configuration with reflector versus parallel arrangement without reflector [76]

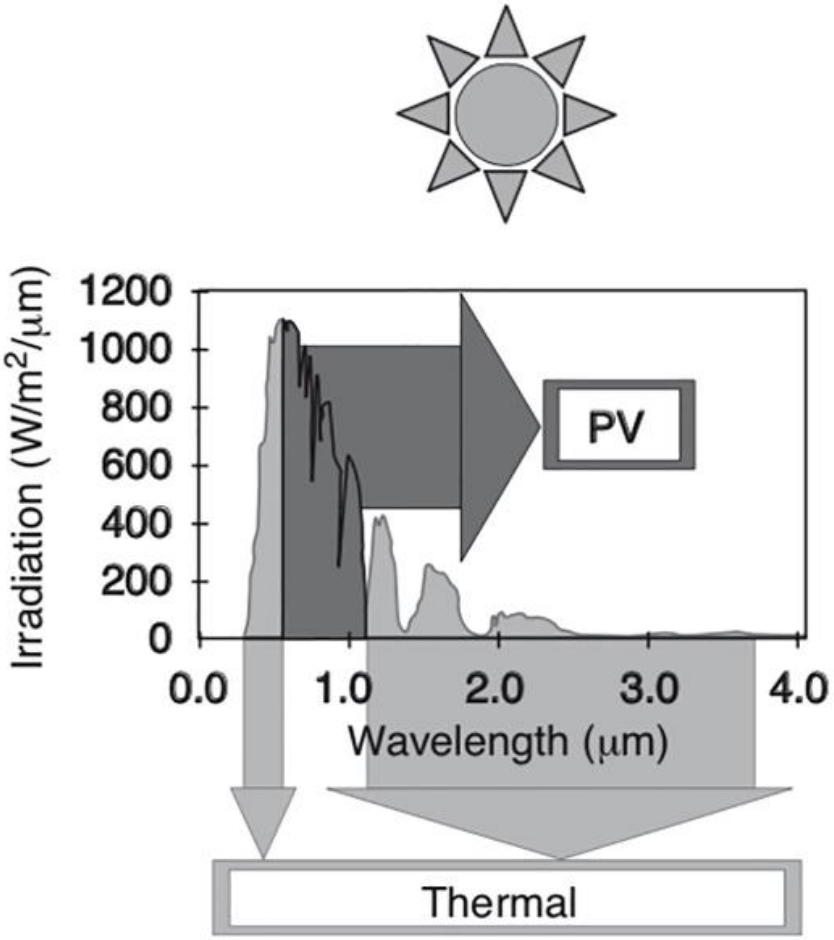

Figure 2.19: The solar spectrum range that is split for thermal and PV energy conversion [77]

A research team at Stanford university designed one such hybrid device that functions as a regular solar panel during daylight hours and as a TEG device when the evening temperature is below the air temperature. The atmosphere around the device is warmed naturally by the sun's warmth radiated onto Earth and then reflected into space. On a clear night, the device is predicted to generate $50\frac{mW^2}{m}$ of power, under an open circuit voltage of 100mV [78]. Figure 2.20 shows the PV/TEG device. Whereby (a) Shows the schematic illustration of the hybrid device and (b) Displays a picture of the device.

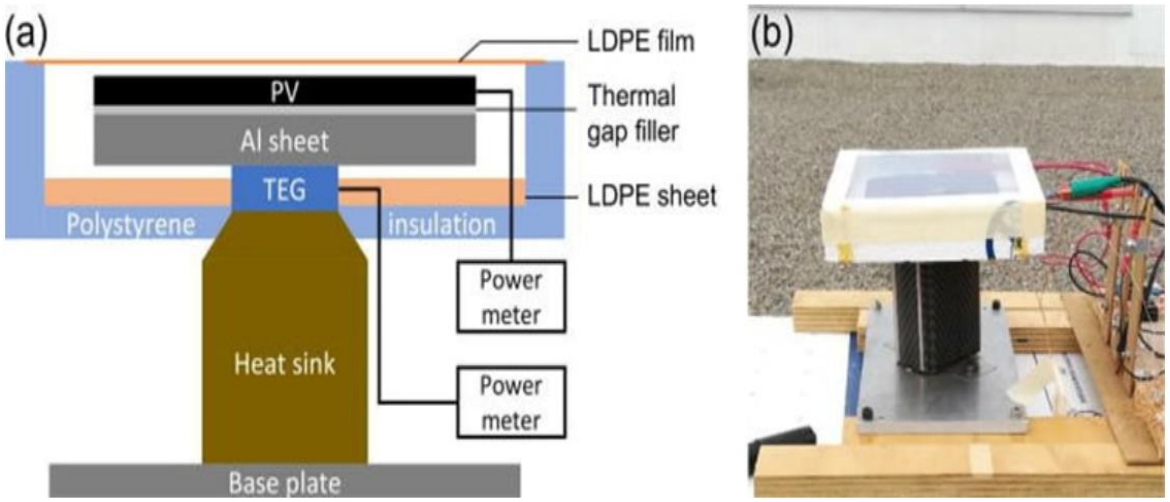

Figure 2.20: The dual PV/TEG device [78]

It is noteworthy that the above-mentioned hybrid device consists of an Aluminium sheet sandwiched between the PV and the TEG. This is then encapsulated in a polystyrene insulation, to prevent heat loss. The TEG is attached to a heat sink. The proposed TEG system in this research paper utilises 2 Aluminium L-bar rods as heat sinks attached onto the 'cool side' of the Peltier tile as well.

Ju, et al. [79] proposed a numerical model and analysis of a spectrum splitting PV-TEG hybrid system. The power generated as a unit was found to be 0.225W and the system achieved a good electrical performance under low operating temperatures. It was also found that the PV-TEG hybrid system is better suited for high concentration conditions and that the TEG sub-system contributed 10% of the output power in the hybrid system. Figure 2.21 shows a schematic of the numerical model simulated for the spectrum splitting PV-TEG hybrid.

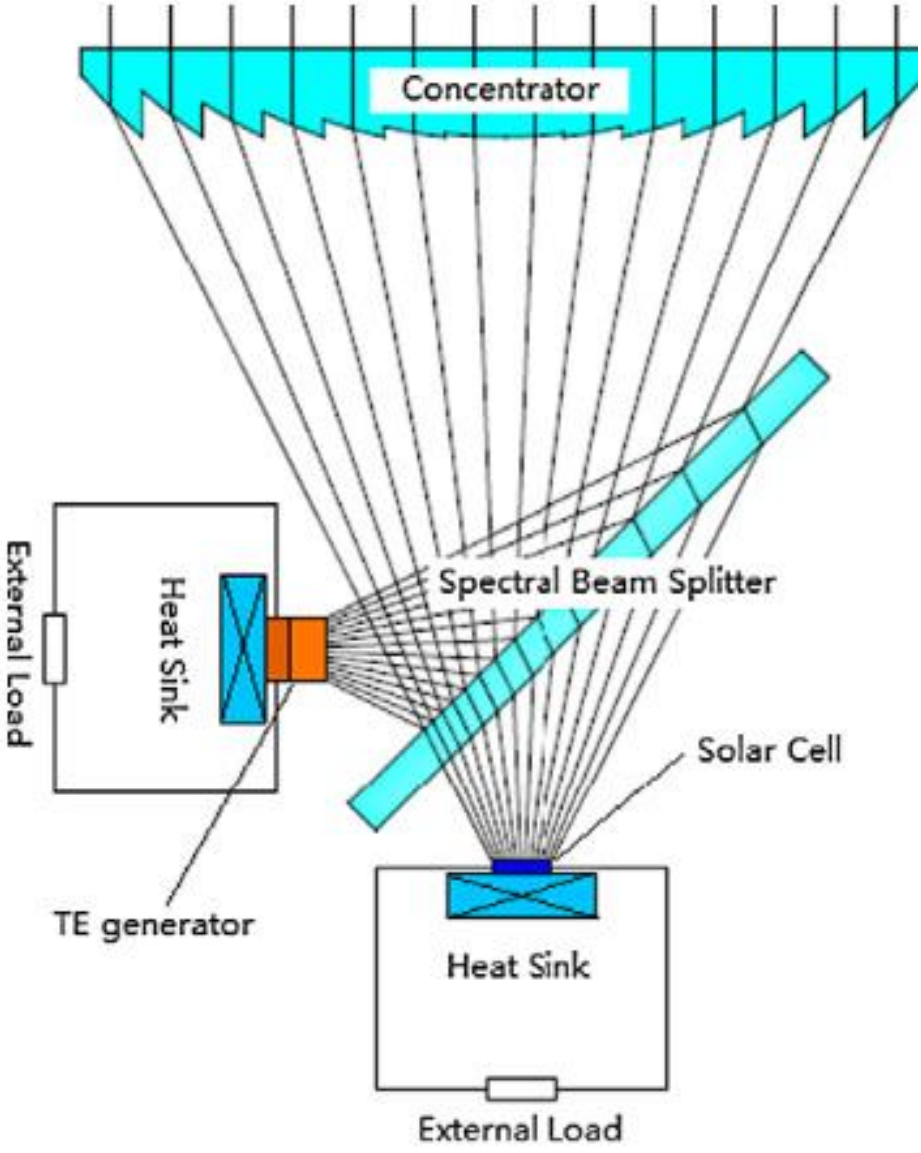

Figure 2.21: The spectrum splitting PV-TEG hybrid [79]

Zhu, et al. [80] fabricated a thermal concentrated PV-TEG hybrid system with optimized thermal management by utilising the thermal benefits of a copper plate as the thermal concentrator and conductor in the system. Theoretical and numerical calculations of temperature distribution and heat flow governed the optimised design. The copper plate ensured a large temperature difference between the hot and cold side of the TEG sub-system. It was found that the TEG sub-system enhanced the outdoor efficiency of the unit by 25%, compared to PV cells. Furthermore, the TEG sub-system generated an additional 648J of electrical energy during the absence of sunlight. Figure 2.22 is an image showing (a) Schematic of the PV-TEG model and (b) Heat flux and temperatures in the model.

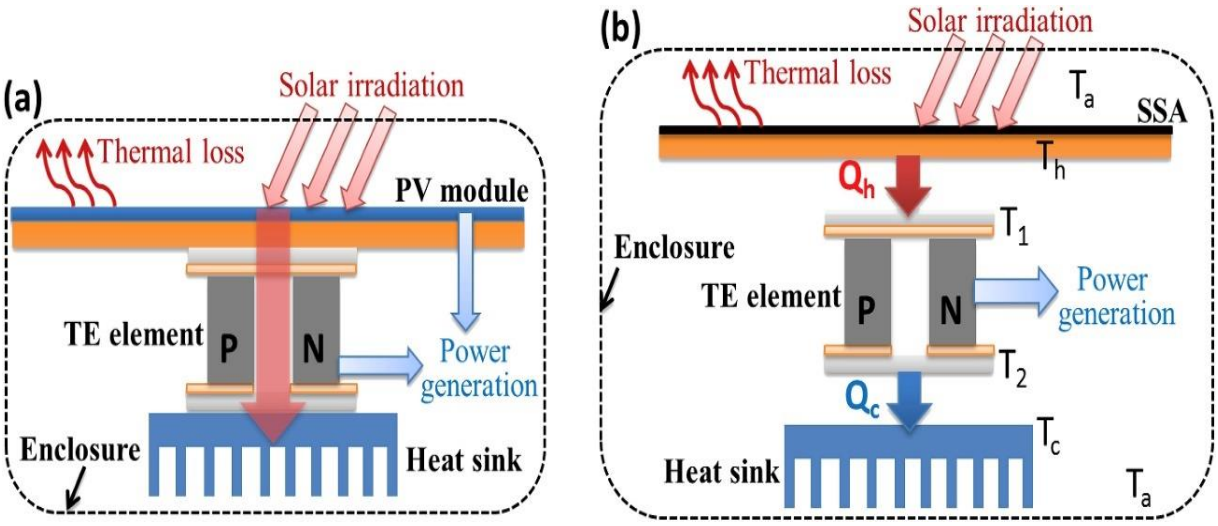

Figure 2.22: The concentrated PV/TEG model [80]

A new structure of a PV-TEG system was constructed using a parabolic trough collector along with PVs and TEGs connected in series [81]. The receiver of the system consists of a triangular channel of reflective material, with PVs and TEMs connected in a specific arrangement such that a large portion of solar radiation is converted directly into electricity. Twenty TEC1-12706 TEMs are connected in series and for higher thermal performance, silicone thermal paste was used in between the TEMs, the back of the 8 PV cells and the triangular receiver channel. A water bath cooling system was also integrated in the system via a water inlet and outlet pipe. The temperature of the water was kept constant with the help of temperature sensors and a thermometer data logger. The system is also equipped with a one-axis solar tracker which found that the average daily thermal and electrical efficiencies can be optimised to 46.16% and 4.83%, respectively.

Figure 2.23 shows (a) Photo of the TEM used, (b) The PV cells used, (c) The arrangement of the twenty TEMs on the receiver sides before PV array is attached and (d) The PV cells attached onto the system and enclosed in a glass casing. Figure 2.24 shows images of (a) The parabolic trough collector with the sun tracker, facing towards Earth's polar axis and corresponding major components of the system, (b) The receiver tube of the hybrid system without a glass cover and (c) The receiver tube of the hybrid system enclosed in a glass cover.

Figure 2.23: The PV/TEG system on the triangular receiver [81]

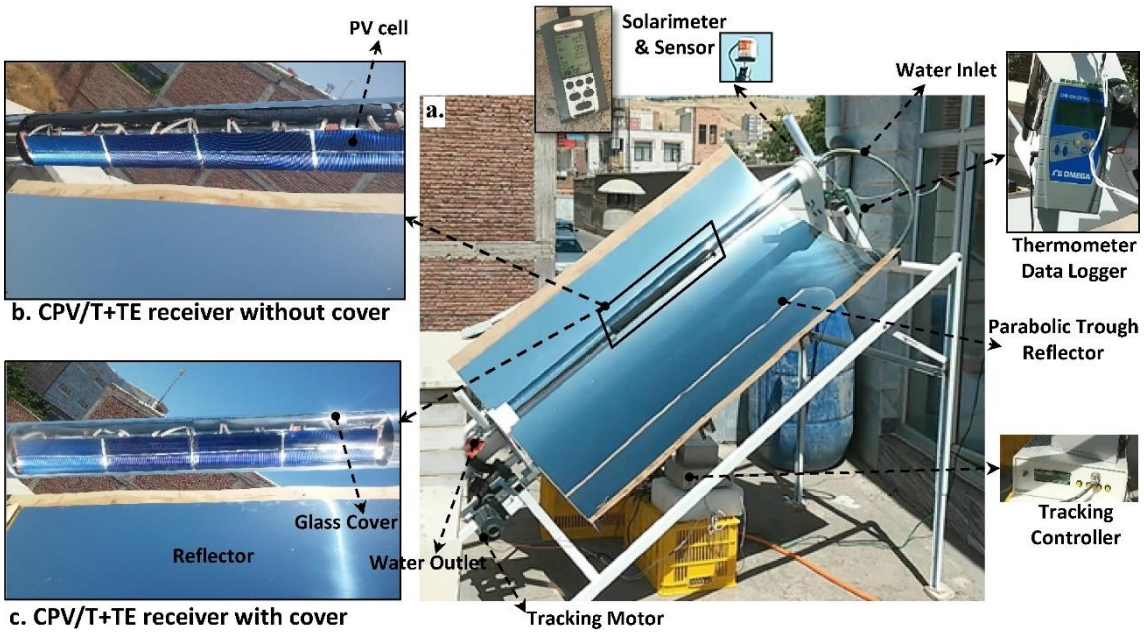

Figure 2.24: The PV/TEG system in application, with the parabolic trough reflector and solar tracking device [81]

Cui, et al. [82] presented an experimental-comparative study of a PV-TEG hybrid that utilises a phase changing material (PCM) as a heat sink and a pure PV system under the same conditions. The device encompasses a dual-axis sunlight tracking system to allow for the PV-TEG system to always be facing perpendicularly to sunlight. The system is exposed to a Fresnel lens and second prismatic glass is attached on the PV cell. A copper water cooling heat sink was compared to an aluminium air-cooled heat sink. The pure PV system is also concurrently placed on the dual axis tracker as a comparative study. A high precision electronic load measures the I-V curves of the system. Figure 2.25 shows the schematics of this design structure.

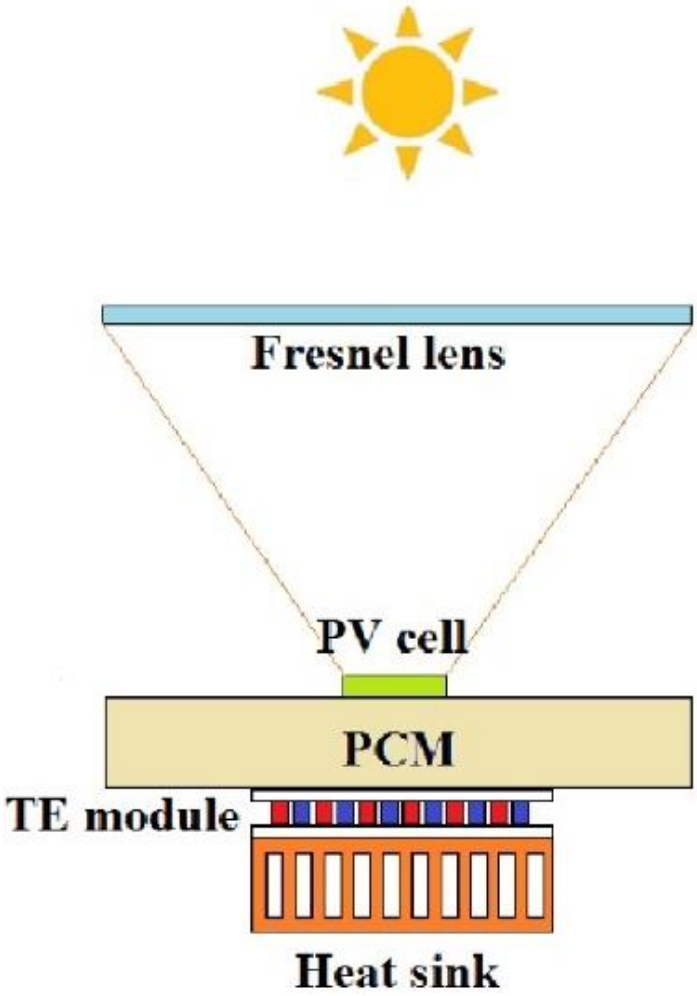

Figure 2.25: The PV/TEG system which is assembled on a dual axis solar tracking system [82]

2.5 Methods to calculate power output.

In this sub-chapter, the various methods adopted by researchers to calculate power output are discussed, as well as the methodology adopted in this research. Methods to calculate power output such as the IV Curve generation method, the load optimisation method, utilising an electronic load device and the maximum power point tracking (MPPT) method are focused on. Another method, which uses mathematical modelling, has been done in previous and ongoing research. However, this method is beyond the scope of the proposed research and will be touched on briefly.

2.5.1 Method adapted in this research-The IV curve generation method.

The power modelling method to calculate maximum power, experimentally, has been adopted from the work done by Lashin, et al. [64]. For the purposes of this research, the IV Curve Generation method was used to establish the parameters required to calculate P_{max} only. The generation of IV curves is beyond the scope of this work. A portion of the method is used as a technique to calculate P_{max} and thus, IV curves are not generated in this work. The experiment estimates certain TEG properties by measuring the open-circuit voltage, the short-circuit current, along with the temperature difference (ΔT) between the hot side(T_h) and the cold side(T_c) under two different conditions. These conditions are when the circuit terminals are (1) electrically open (2) electrically shorted. The heat flow (Q_{in}), and thus the ΔT was controlled and kept constant under both conditions by using a solar simulator.

The maximum power is given as a function of short circuit current and open circuit voltage in equation 2.1:

$P_{max} = \frac{1}{4} I_s \times V_o$ (Equation 2.1) [64]

Where P_{max} is the maximum power generated by the TEG system, I_s is the current measured in closed circuit position (A) and V_o is the open circuit voltage measured (V).

The method to establish the above currents and voltages under the 2 electrical conditions mentioned were found using the 'TEG performance IV curve generation' method by McCarty and Piper [83], which was also applied in Lashin's [64] work. A summary of this IV curve generation method is displayed in Table 2.1, which entails connecting the circuit shown in Figure 2.26 and running the experiment to obtain 4 subsequent pairs of data points.

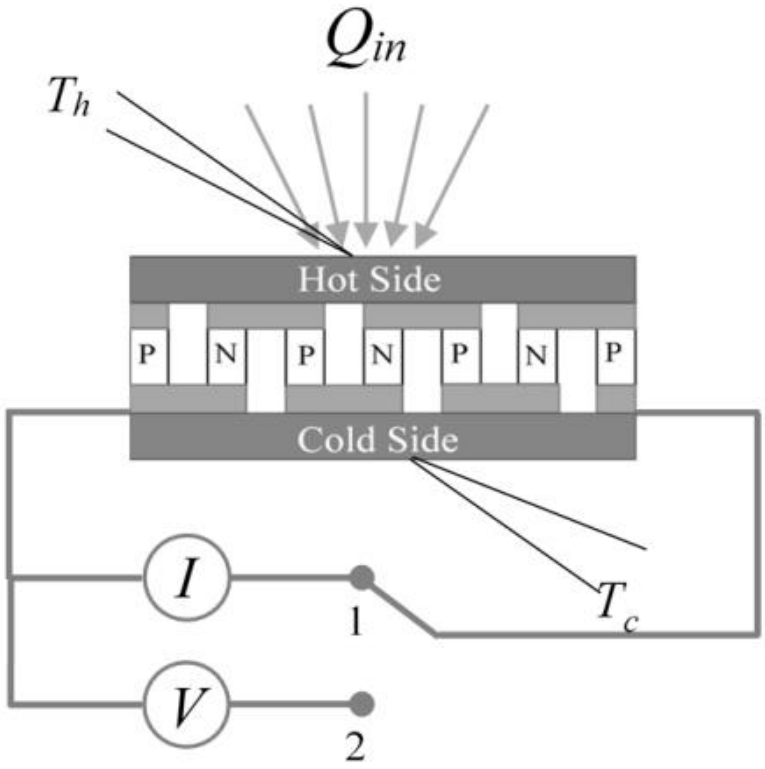

Figure 2.26: The circuit connection used in the IV curve generation method [64]

Table 2.1: The summarised steps in the IV curve generation method.

	Circuit condition in Figure 2.35	**Points to be measured**
Step 1	Position 1	a.) I_s is measured after the desired ΔT is reached b.) Initial Voltage is observed to be 0V and then V_s is measured.
Step 2	Position 2	c.) V_{s-o} is measured promptly after opening the circuit d.) I_{s-o} is measured and the current is observed to then fall to 0A.
Step 3	Still in position 2	e.) Desired ΔT from step (a) is established, V_o is measured f.) Initial current is seen as 0A and the resulting I_o is measured.
Step 4	Returns to position 1	g.) I_{o-s} is measured immediately as the switch is closed. h.) V_{o-s} is measured immediately as the switch is closed.

P_{max} is then calculated using Equation 2.1 and these results can be graphed to display the maximum power output under different conditions. The effect of the 2 parameters on P_{max} tested and investigated in this research are discussed in Chapter 1.2.

2.5.2 The load optimisation method

In contrast, previous researchers mentioned in chapters 2.1-2.2 calculate an output power by using equations 2.2 or 2.3.

$P = VI$ (Equation 2.2)

$P_{out} = I^2 R_{load}$ (Equation 2.3)

Load optimisation is required to maximise the power output of TEGs, like PVs. The optimal load is determined by using a current source as the variable resistor, the current and voltage drop are simultaneously measured across copper electrodes on the cold side. Equation 2.2 is then used to calculate the maximum power output under optimal load conditions [56, 57].

The miniature TEG device fabricated after an optimised design established through Finite Element Method (FEM) simulations by Shen, et al. [84], also followed a similar approach as the aforementioned load optimisation method. During experimentation, maximum current (short circuit current) and the resulting maximum power obtained, was observed under the same load resistance i.e., when the internal resistance of the TEG matched the external load resistance. Resulting power was also calculated using Equation 2.2.

Jeyashree, et al. [67] measured voltages and the respective currents generated by the proposed design, throughout the day, within a time frame of 10H00 and 13H30. The maximum readings generated by 44 TEGs in series with 66 parallel paths at peak sun was 25V and 20A. The resulting Power of 500W is calculated using Equation 2.2.

2.5.3 Mathematical modelling

An equation for maximum power was incorporated in the general equation mathematically modelled and formulated by Mgbemene, et al. [62] for the device performance of the proposed 3D compound concentrator and the TEM hybrid system.

Mathematical modelling such as the above, equations generated and further analysis into power generation, thermal studies and resulting relationships were investigated by more researchers mentioned in chapters 2.1-2.2 [62, 63, 65, 66].

2.5.4 Electronic load device

Typically used to measure the IV curve output of a PV solar cell, the IV curve measurement is done by applying various voltages to the device. For each voltage applied, the corresponding current flowing through is measured. The voltage supplied is measured by a voltmeter connected in parallel and the current is measured by an ammeter connected in series. An electronic load device such as the high precision N3302A, by Keysight Technology inc., previously mentioned in chapter 2.3, is used by Cui, et al. [82]. Electronic load devices measure the IV curve using this method.

2.5.5 Maximum Power Point Tracking (MPPT)

To increase the output power of a TEG and its subsequent efficiency, a MPPT algorithm may be adopted. The algorithm pushes the operating point of a TEG to its 'optimum location'. A TEG may be modelled by a DC voltage source (V_{oc}) found in series with its internal resistance (R_{TEG}). By way of explanation, the MPPT algorithm fulfils the role of adaptively changing the load to match the TEGs internal resistance, thus leading to a maximum power transfer i.e., $R_{TEG} = R_L$ [85]. Figure 2.27 shows the electrical equivalent diagram and circuit of the TEM.

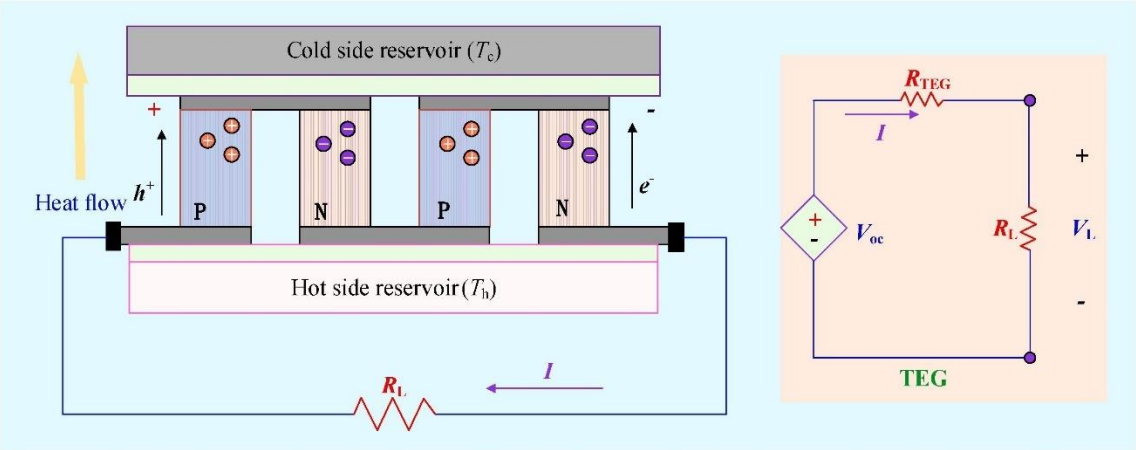

Figure 2.27: Image of the electrical equivalent circuit of a TEM [85]

When a TEG's output power is at this 'optimum location' (the MPP point), V_{oc} (voltage reading when $I = 0$) and I_{sc} (current reading when $V = 0$) are found at their half-values, as shown in Equation 2.4 and Equation 2.5 respectively [86]. A technique to measure these critical points, called the IV curve generation method is explained in chapter 2.5.1.

$V_{MP} = \frac{V_{oc}}{2}$ (Equation 2.4)

$I_{MP} = \frac{I_{sc}}{2}$ (Equation 2.5)

The resultant maximum power is given by the product of V_{MP} and I_{MP} as shown in Equation 2.6 (this is derived from Equation 2.2).

$P_{MP} = \frac{V_{oc} \times I_s}{4}$ (Equation 2.6) [87]

It is noteworthy to point out that the maximum power equation from the IV curve generation method used by Lashin, et al. [64] in Equation 2.1 presented in chapter 2.5.1 ties up with the maximum power equation from the aforementioned MPPT method. However, the MPPT theorem uses derivatives and substitution to attain the P_{max} equation used.

Conventional MPPT power electronic converters in PVs and TEGs use the MPPT method. The drawback is that it necessitates a disconnection between TEG and converter for the measurement of V_{oc} and I_{sc}, i.e., energy does not flow from the TEG to the converter and so, power is not harvested during this time. However, MPPT schemes have been implemented to avoid this drawback. One such scheme was presented by Dalala, et al. [85] who employed a microcontroller-based technique while holding MPPT capability. The MPPT harvesting system was validated experimentally and analytically. Figure 2.28 and Figure 2.29 shows the voltage versus power graph of results obtained from the MPPT harvesting technique and the voltage versus current graph of results obtained, respectively.

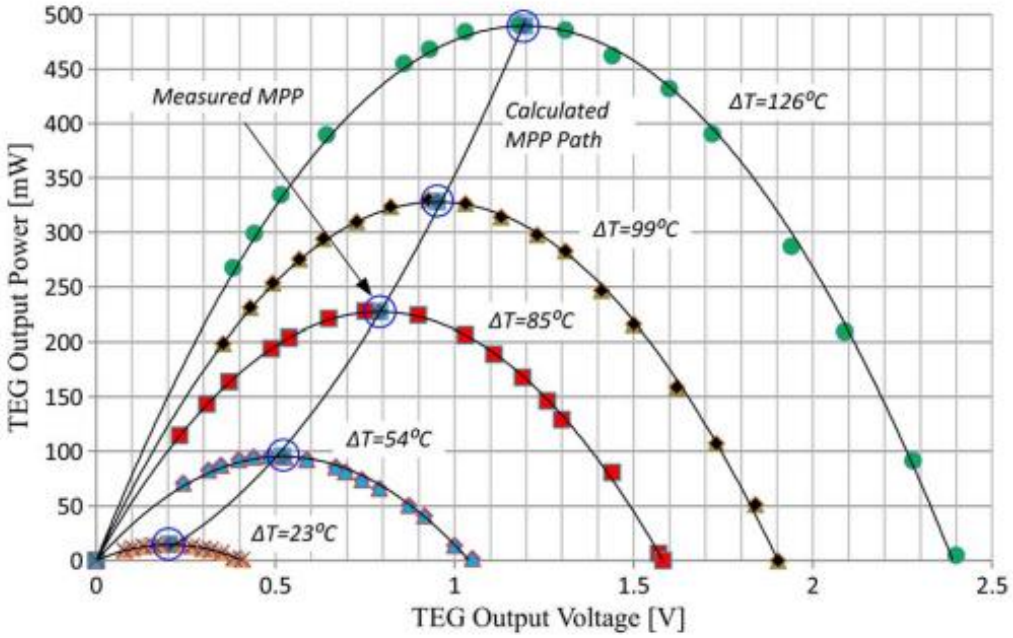

Figure 2.28: Voltage versus power graph of results obtained from the MPPT harvesting technique [85]

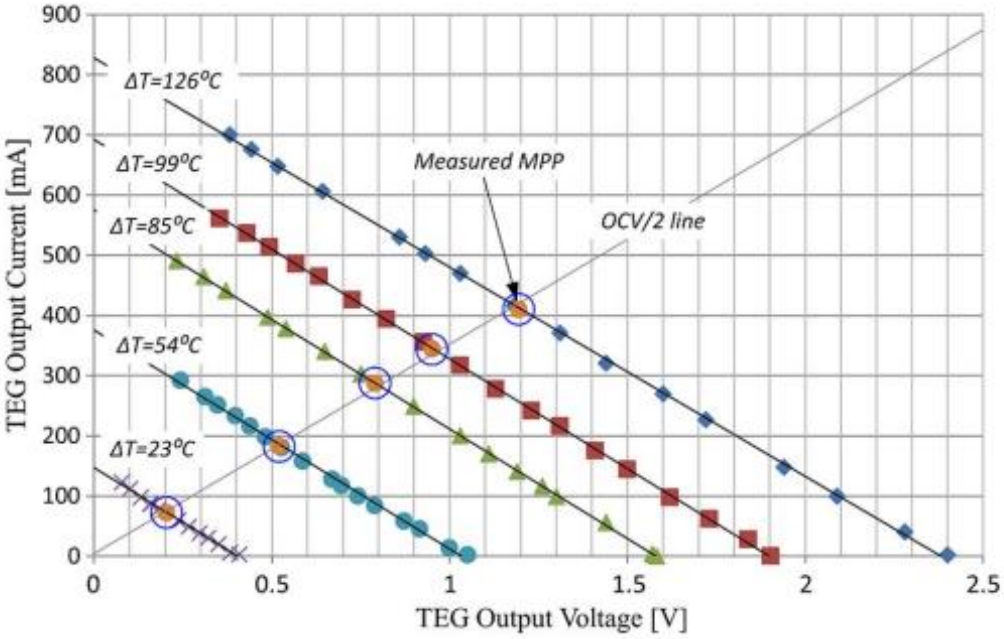

Figure 2.29: Voltage vs current graph of results obtained from the MPPT harvesting technique [85]

Figure 2.28, crosschecked with Figure 2.29 for any ΔT generated in the TEG, verifies that the maximum power is the product of V_{MP} and I_{MP} as shown in Equation 2.6. It is also verified that the TEG's power is at this optimum location when V_{oc} and I_{sc} are found at their half-values, as shown in Equation 2.4 and Equation 2.5, respectively.

2.6 Series vs Parallel electrical connection of TEMs

An array is formed when several TEMs are electrically connected in series and/or parallel to supply the required voltage and/or current. Since TEMs are modular in nature, connecting an array can scale up a TEG system depending on the required output. The output power required is strongly dependent on the application, but this generally ranges from microwatts (mW) to kilowatts (kW). When the power requirements of a system exceed a few Watts, the required number of TEMs are employed in series or parallel electrical arrangement. The type of electrical connection required in the array depends on the voltage and/or current required [88]. The TEGs may be connected in series to enhance the voltage output and may be connected in parallel to enhance the current output [86].

The series arrangement of TEMs as an array can be seen in Figure 2.30. Each TEM in Figure 2.30 is represented by a Voltage source V in series and an internal resistance R. Vs is the voltage at the terminals for the series array. Under realistic and practical thermal operating conditions,

each TEM may be experiencing a different ΔT, hence, a different voltage and internal resistance per TEM may be generated. Therefore, the voltages and internal resistances will not be the same. The total internal resistances equivalent is R_{int} and the load resistance is denoted by R_{load}.The output voltage in the series array is given by Equation 2.7 [89]. Figure 2.30 shows the circuit diagrams of a TEG array, where 3 TEMs are connected in series and circuit (b) is the condensed equivalent of circuit (a).

$Voc = V_1 + V_2 + V_3$ (Equation 2.7)

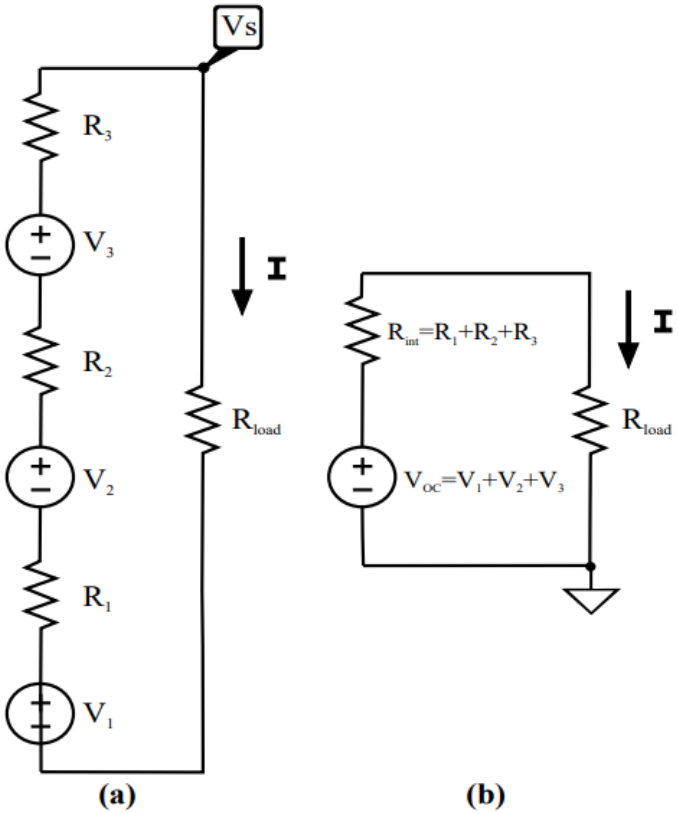

Figure 2.30: Circuit diagram of 3 TEMs connected in series and its equivalent circuit [89]

Vp is the voltage at the terminals for the parallel array. The currents in the parallel array can be given by Equations 2.8, 2.9 and 2.10. Figure 2.31 shows a circuit diagram of 3 TEMs connected electrically, in parallel.

$I_1 = \frac{V_1 - Vp}{R_1}$ (Equation 2.8)

$I_2 = \frac{V_2 - Vp}{R_2}$ (Equation 2.9)

$I_3 = -I_1 - I_2$ (Equation 2.10)

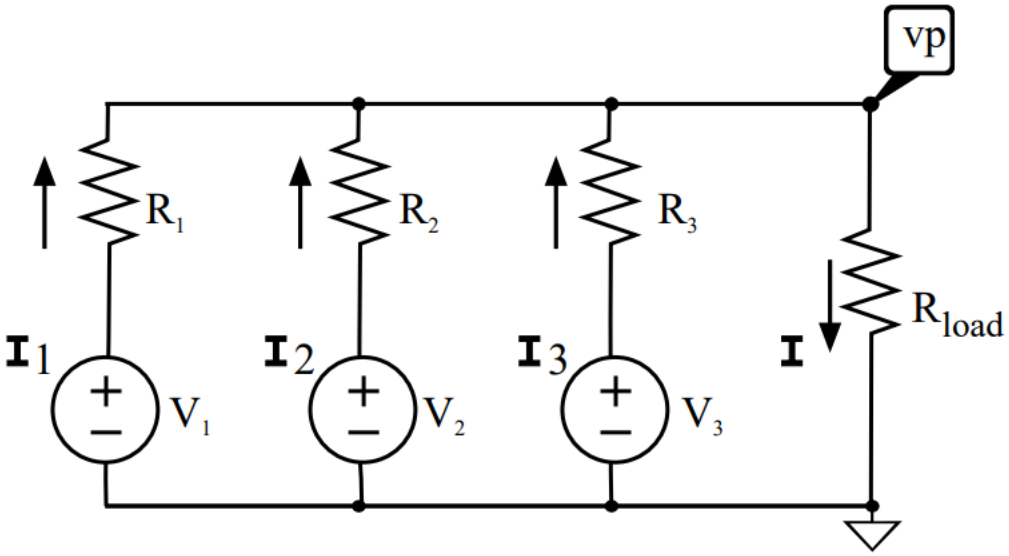

Figure 2.31: Circuit diagram of 3 TEMs connected in parallel [89]

Chen, et al. [90] conducted experiments to understand TEM characteristics and performance on power generation. One of the characteristics tested was the effect that the number of TEMs electrically connected in series have on the power generated. When four TEMs containing 127 thermoelectric couples of the same size were connected in series to test output power generation, it was found that the higher the number of TEMs in series, the higher the maximum power obtained. Theoretically, a linear relationship between number of TEMs connected in series and the power output is expected. However, the results obtained show that the relationship between the number of TEMS in series under large currents, and the output power differ from the expected linear relationship. This anomaly was attributed to the non-uniform properties of the TEMs from uncertainties that may have occurred during manufacturing processes. It was concluded that the number of TEMs electrically connected in series are linearly proportional to the open circuit voltage and maximum power only when under appropriate operating conditions such as under low electrical current.

Morais, et al. [91] presented an electronic circuit designed to measure the maximum power harvested by utilising low voltage TEGs in connection with a DC-DC converter. A precise yet low temperature gradient was applied between the hot and cold sides under different TEG configurations and copper heat sinks were used. It was found that for a high ΔT, the output power measured directly at the output terminals is higher when TEGs are connected in series as compared to when the same TEGs are electrically connected in parallel.

2.7 Industrial applications of TEGs.

2.7.1 TEGs in industrial sectors.

A major contribution to greenhouse gases is by the industrial sector. High amounts and high temperatures of thermal energy is released into the environment as a by-product. This thermal energy can be recovered to an extent which is advantageous to the industry sector due to its economic opportunities and the subsequent lack of greenhouse gases is advantageous to the environment. Industrial organic cycles, boiler technologies, burners and factories can harvest this otherwise wasted thermal energy and convert it into a much-needed source of power [92].

Araiz, et al. [93] developed a computational model to design and predict behaviours of the heat exchangers on a TEG system. Their prototype design was then tested to validate the performance of the computational model.

Another set of experiments were conducted on a factory exhaust duct of a combustion chamber, to validate a computational methodology in harvesting waste heat via thermoelectric generation [94]. The TEG system is comprised of 32 TEMs suited for high heat applications. The testing utilised thermocouple type temperature sensors at different locations on the system to monitor temperature fluctuations. To investigate the maximum output power, 2 ammeters and 2 voltmeters were used to measure the voltage and current deviations by applying variable resistances. Forced convection from fans are used for air circulation on the 'cold side' of the TEG system. A total P_{max} of 24.59W was established from two locations when the inlet temperature was 560°C. Figure 2.32 shows a picture of the TEG application on the exhaust of a combustion chamber. The TEG is compartmentalised into four sets of thermoelectric units (TEUs). Each TEU is comprised of eight TEMs.

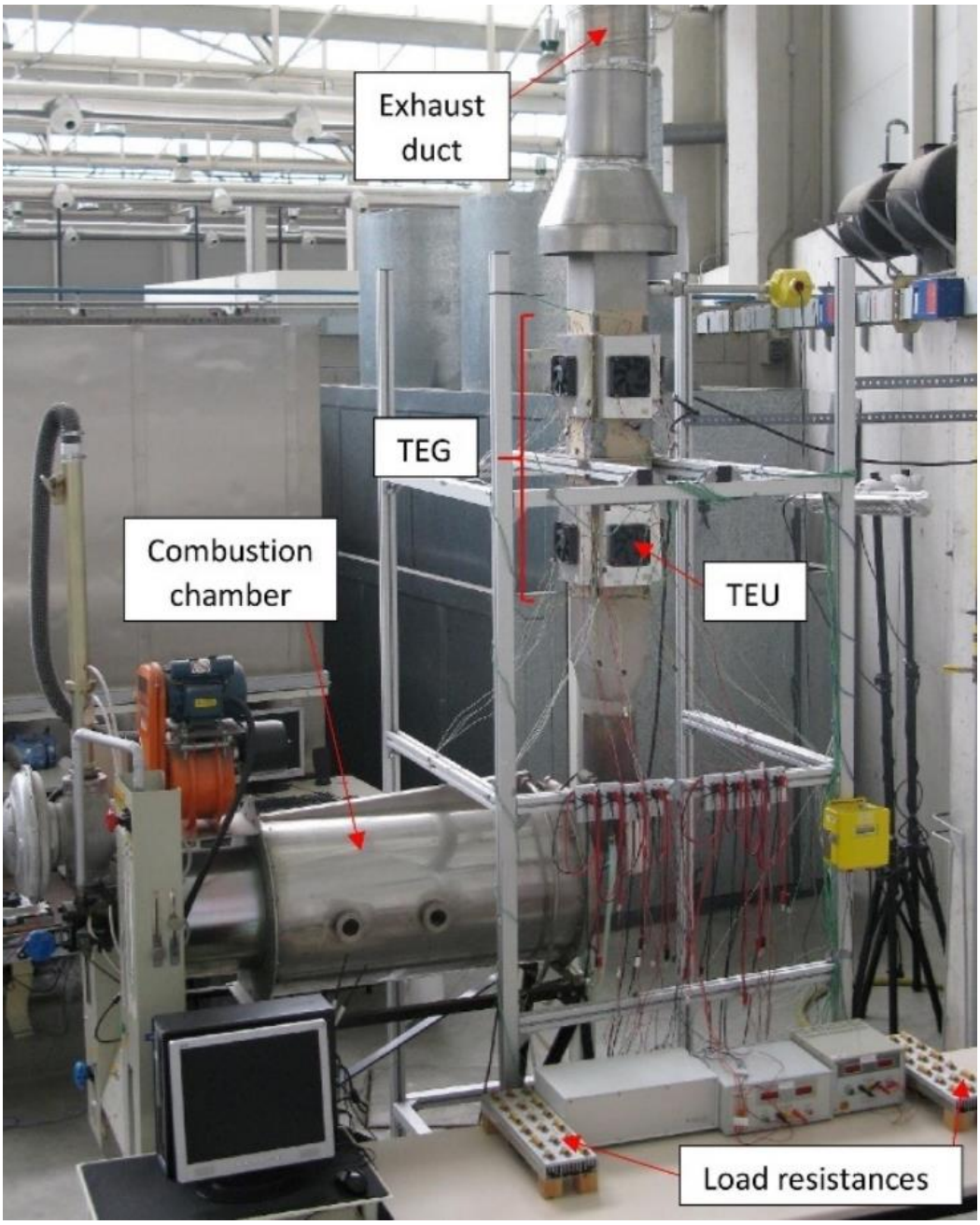

Figure 2.32: The TEG system during application, set up on an exhaust of a combustion chamber [94]

Araiz, et al. [95] then proposed the use of commercially produced TEGs in a stone wool manufacturing plant which successfully converts waste-heat harvested from hot gas flow, into electricity. A curing oven exhaust pipe in the manufacturing plant was selected for the testing of the proposed design which adopted a combination of their previously validated mathematical models [93, 94]. A maximum output power of 45 838W was generated under certain parameters. Figure 2.33 illustrates a schematic of the combination design presented.

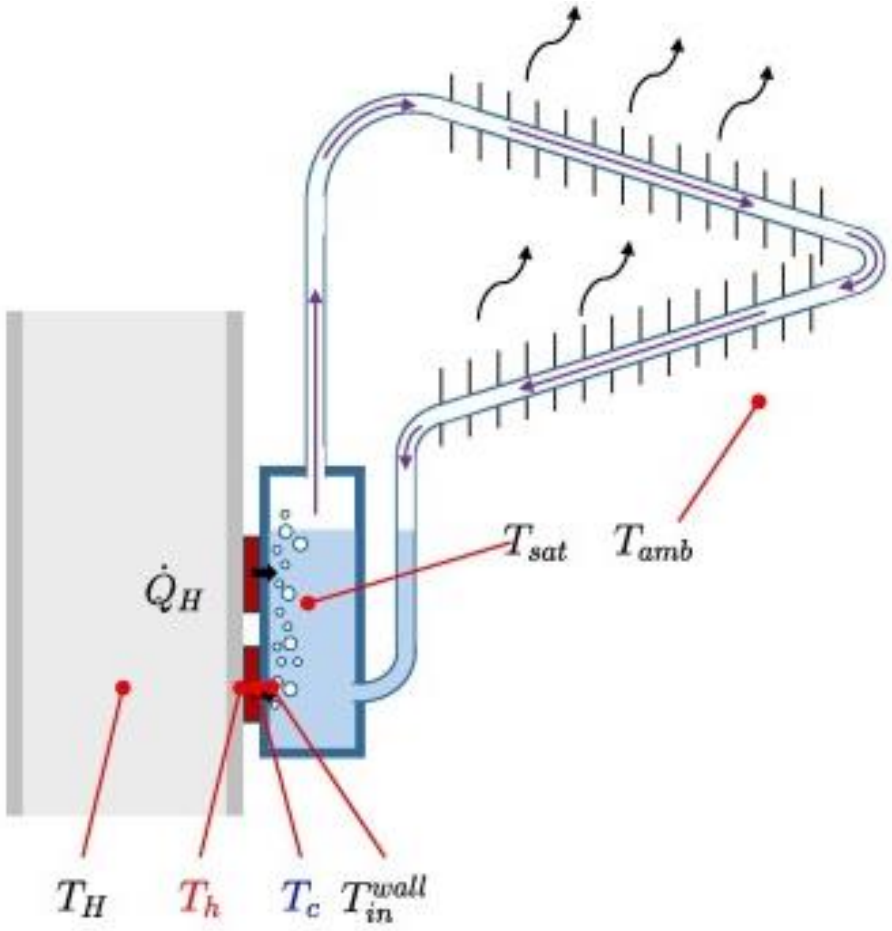

Figure 2.33: The combination design applied in a stone wool manufacturing plant [95]

TEGs have been adopted for lighting where industrial waste heat is the heat source. For this application, the recent energy-efficient light bulbs make use of TEGs. Approximately, 33% of energy given off by the manufacturing industry is wasted, which could be harvested by TEGs into $0.9TWh$ to $2.8TWh$ of electrical power, per year. A TEG system comprised of 40 commercially available TEMs, liquid metal heatsinks, and an electromagnetic pump, was found to generate $23.09V$ when the stabilised heat source temperature was $190°C$ [96]. Four thermocouple type temperature sensors and a voltage transducer were employed. Electrical heaters with a power rating of 2500W in total, were used as the heat source and a data acquisition system was utilised to measure the temperature and voltage. 8 TEMs were connected in series, and this was replicated into 5 groups, electrically connected in a parallel arrangement. The ensemble provided the required 120W to power 4 LEDs. Figure 2.34 shows a picture of the liquid metal-based TEG system designed to provide power to 4 LEDs.

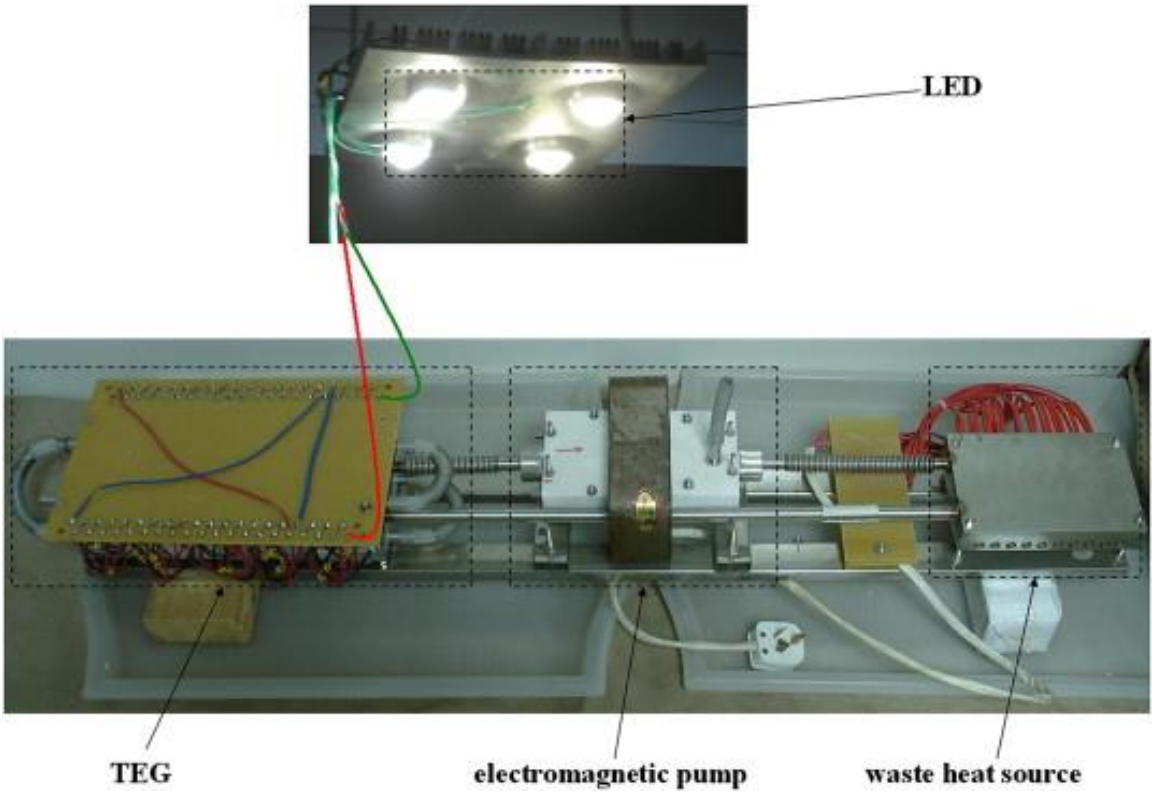

Figure 2.34: The liquid metal-based TEG system designed to provide power to 4 LEDs [96]

Another major industrial process that contributes to thermal energy wastage is the hot forming process of steel. Approximate temperatures of 1300°C is required in the process, most of which is lost to the environment when the forged parts are required to cool to room temperature. A TEG system equipped with 50 TEMs, 5 inverters and 5 cold plates was run under industrial production conditions. The surface area dimensions employed are $0.5m \times 1m$. Five MPPT based micro-inverters were utilised to connect the TEG system to the power grid. The system successfully harvested 14.8kW of heat radiation and subsequently generated 388W of power, which was fed directly into the power grid [97]. Figure 2.35 is a schematic of the TEG system designed for waste energy retrieval from the industrial hot forming process of steel. Figure 2.36 are pictures of this system in application whereby (a) is the TEG system in application during the hot forming process (TEG system can be seen stationary above the hot steel) and (b) is the hot forming process of steel on the conveyor belts.

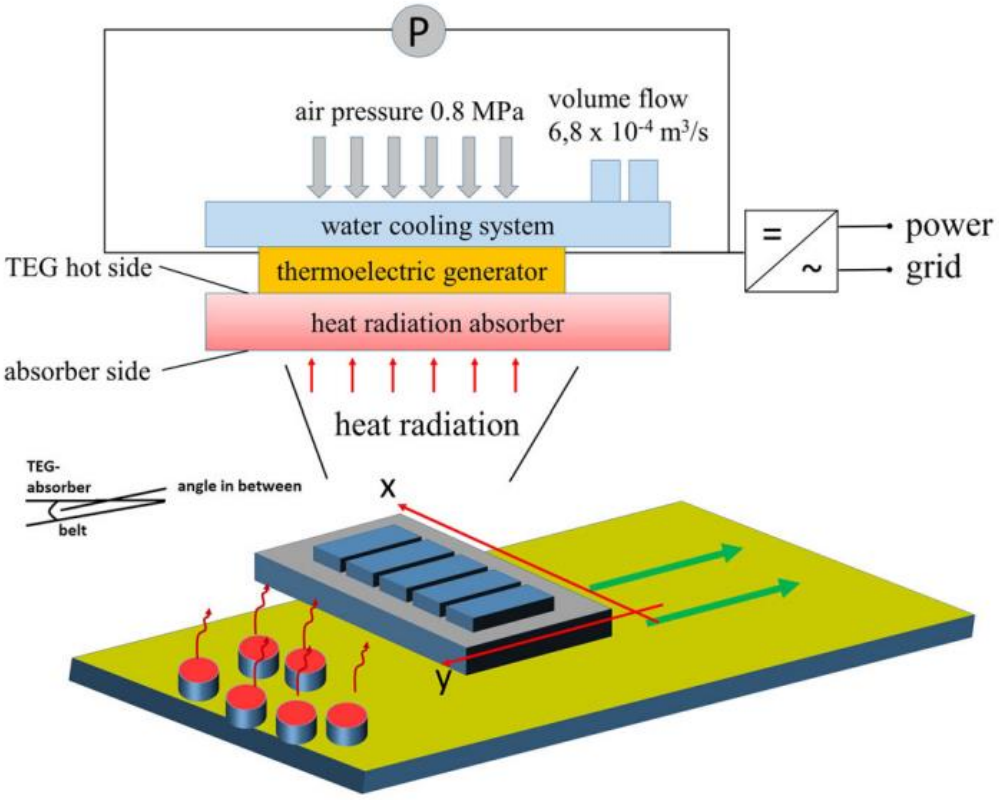

Figure 2.35: Schematic of the TEG system designed for waste energy retrieval from the industrial hot forming process of steel [97]

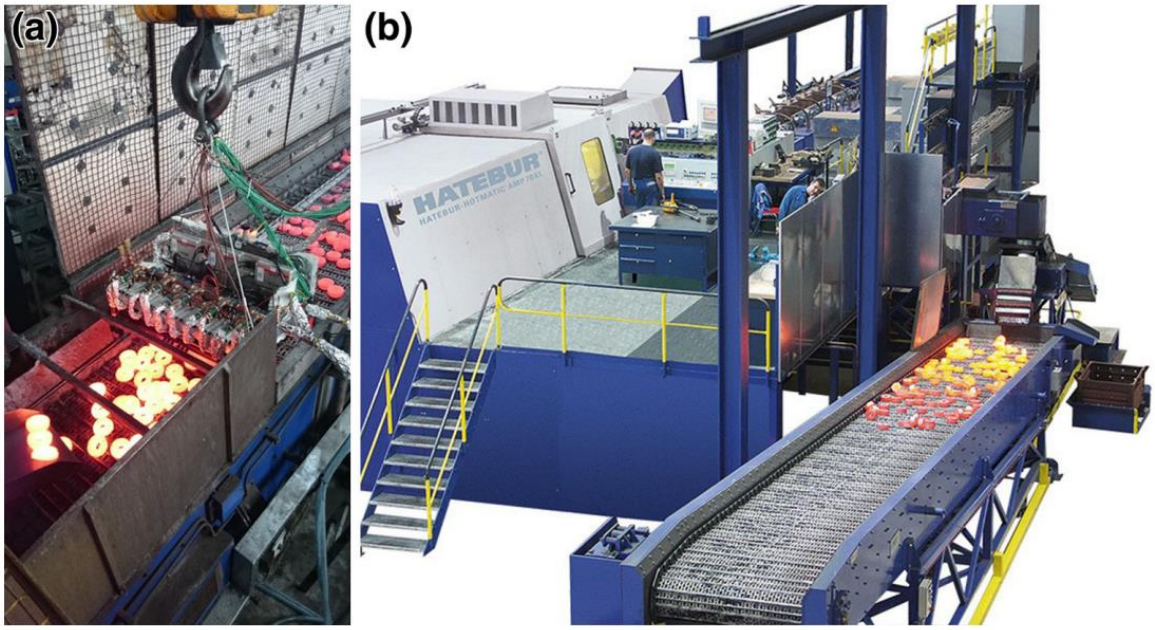

Figure 2.36: The TEG system in application during the hot forming process [97]

2.7.2 TEGs in the medical field

Body heat is a sustainable energy and can be exploited to supply energy to emerging wearables and implanted medical devices (IMDs). These devices and wearables allow for a variety of applications in the medical field including health tracking and monitoring systems, fitness wearables, health examinations for athletes and general daily calorie and sleep trackers [23].

2.7.2.1 Medical devices

Pacemakers

Pacemakers or cardiac pacing devices are small devices that generate electrical pulses to contract the heart at the correct rhythm for an adequate heart rate, and thus pump blood. Currently, the surgically implanted pacemakers employ batteries that generally last approximately 10 years and needs to be replaced surgically. Ongoing research has been conducted to replace the need for batteries with TEGs [98].

Implantable medical devices such as pacemakers have a major drawback due to the life-threatening risk and discomfort during the battery replacement surgery. Pacemakers have a 6V voltage requirement during a heart failure. Bhatia, et al. [99] conducted a feasibility study on a $6cm^2$ 'biothermal battery' TEG-recharger containing 4000 thermocouples in series. The TEG generates 4V for a ΔT of 1°C. The study envisions that the pacemaker with the TEG-recharger can increase the lifespan of the pacemaker by 30 years if it is continuously charged with a ΔT of 2°C. The required ΔT can be established if the device is placed a few millimetres below the surface of the skin. Figure 2.46 is an illustration of the implanted biothermal battery for the pacemaker.

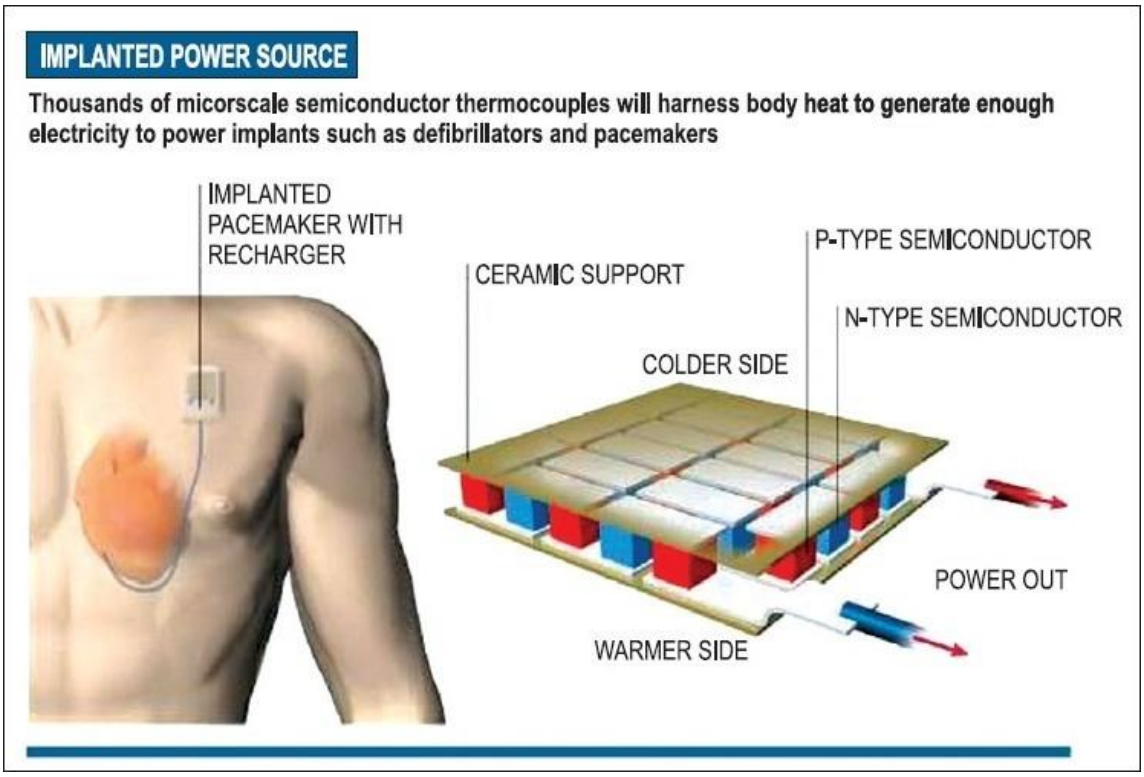

Figure 2.37: The implanted biothermal battery for the pacemaker [99]

Electrocardiographic (ECG) monitoring systems

Electrocardiographic (ECG) monitoring systems are meant to monitor heart function to manage and determine health conditions. Advances in electronic miniaturisation and thermoelectric materials have paved the way for a new era of ECG monitoring devices powered by TEGs. Rigid and flexible TEGs have been incorporated in ECG monitoring systems in the past, however, new wearable designs in practical applications have been found to provide a stable power supply as well.

Leonov, et al. [100] employed 14 miniature TEGs to create a thermoelectric powered shirt with a wireless ECG system. Under an ambient office condition of 23°C, the TEG generated an output power of 0.8-1mW while the wearer was stationary. Power requirement to sufficiently run a wearable ECG system is 1mW. This power output has the potential to be enhanced by 203mW when the wearer is active.

Kim, et al. [101] designed a wearable ECG monitoring system which incorporated a flexible TEG and a polymer-based flexible heat sink (PHS). The TEG is powered by the wearer's body heat and contains a flexible ECG sensing circuit. The output power generated was higher than 38µW per cm^2 for the first 10 minutes of the run and this power reduced to 13µW for another 22 hours of use. This power level was found to be sufficient to continuously run the entire

wearable ECG system. Figure 2.38 is an illustration of the self-powered wearable ECG monitoring.

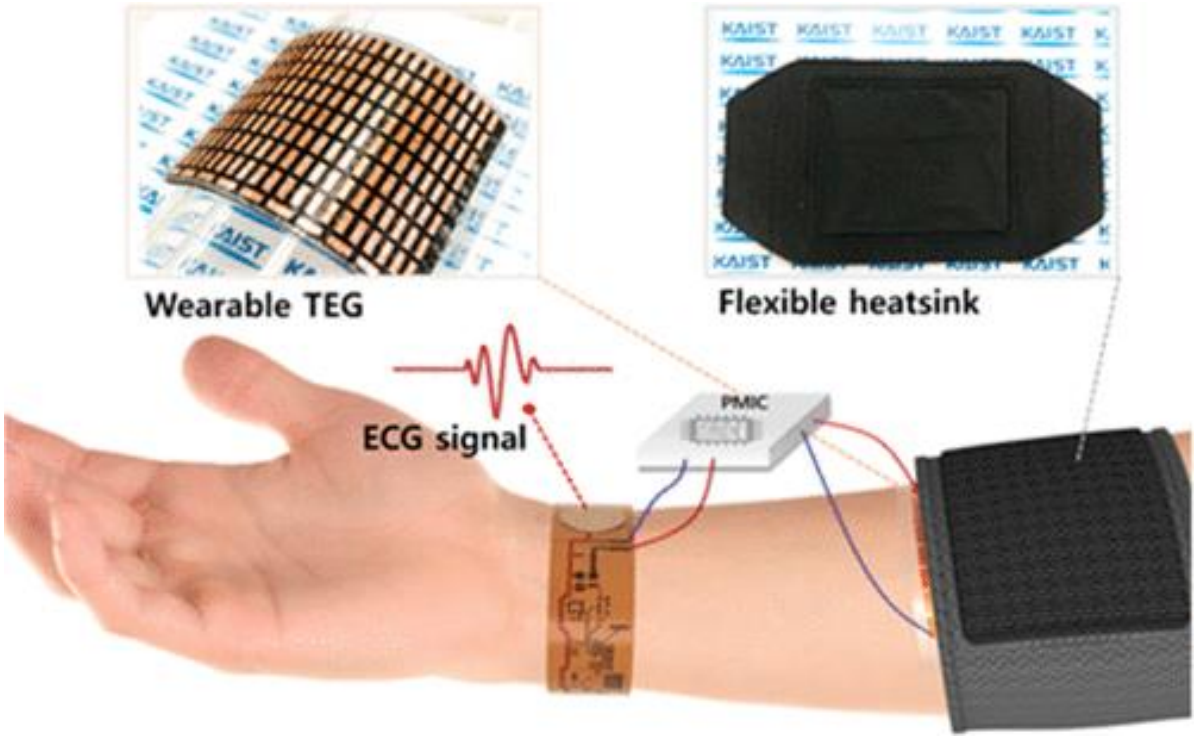

Figure 2.38: The self-powered wearable ECG monitoring system [101]

Human health monitoring systems

A wearable device was designed to monitor blood pressure, body temperature and pulse [102]. An integrated TEG is used to charge a zinc polymer power bank battery which runs the monitoring system. Human body heat is used to drive the TEG and an aluminium rigid heatsink is employed in the prototype. An intelligence was created to send and receive signal messages with a cloud service available on an android app designed to be used by medical staff. The power generated is utilised in the design to power the necessary sensors. No further information into the TEG design and experimental aspects were provided. Figure 2.48 shows a picture of the health monitoring system experiment during prototype stages.

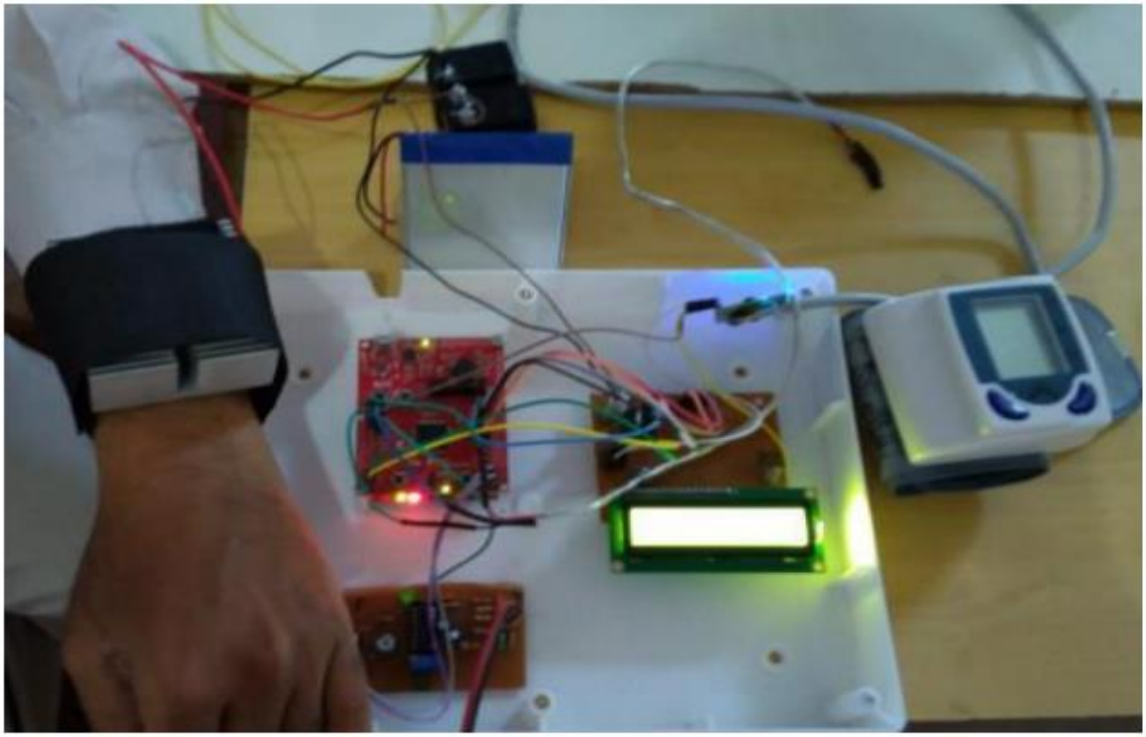

Figure 2.39: The health monitoring system experiment [102]

2.7.3 TEGs in wearables and textiles as energy harvesters.

The human body releases roughly 200-525W of thermal energy which could be converted to electrical energy by utilising the proper techniques in energy conversion [103]. Due to the small size and power output generation advantages of TEGs, TEGs are considered suitable devices as wearables to harvest the thermal energy provided by body heat [104]. These TEG-based wearables should be worn on body parts that provide a significantly large heat range such as at the inner knee, chest, forehead, neck and armpits [105].

The average ΔT between body temperature and the ambient air is approximately 13°C, depending on bodily location, body activity and environmental conditions. The electrical power required to sufficiently supply wearable medical devices and IMDs is less than 5mW [23], hence, the wearables mentioned here produce sufficient energy for this purpose.

Theoretically, TEG-based wearables can generate a maximum of 180µW per square centimeter of skin at an ambient temperature of 22°C [106]. However, to overcome the small ΔT produced across the surfaces of the TEG, Settaluri, et al. [106] incorporated a 'copper heat spreader' heatsink of 1 mm thickness in the design of the TEG-based wearable. The thin design also utilised a DC-DC converter, and the resultant TEG ensemble was found to generate 4.18V when

the heatsink thickness was less than 5 mm. Figure 2.40 is an illustration of the thin TEG-based wearable infused with a DC-DC converter. The wearable is a thin elasticated band.

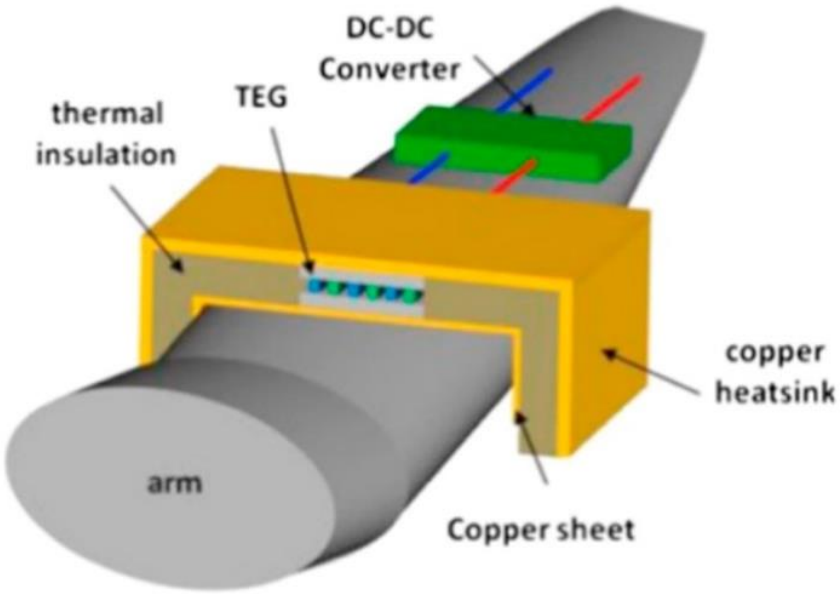

Figure 2.40: The TEG-based wearable [106]

Shen, et al. [84] fabricated a miniature flexible device ideal for wearable electronic devices comprised of a planar TEG on a polyimide film to reduce thermal losses from the substrate. The design was first optimised using the finite element method. The optimised design concentrates heat from solar radiation through a solar absorber and cools it off using a heatsink in a water bath to establish a temperature differential of $6°C$ and hence, a power output of $2.3\mu W$. Figure 2.41 shows a schematic diagram of the STEG whereby, (a) Solar absorber absorbs and generates heat on the inner side. (b) Cross-sectional view illustrating the lateral heat flow to the substrate. Figure 2.42 shows the experimental set up to measure the STEG performance whereby (a) Overview of the set up during experimentation, (b) STEG device with the sun-blocking plate, and (c) STEG device with sun blocking device removed.

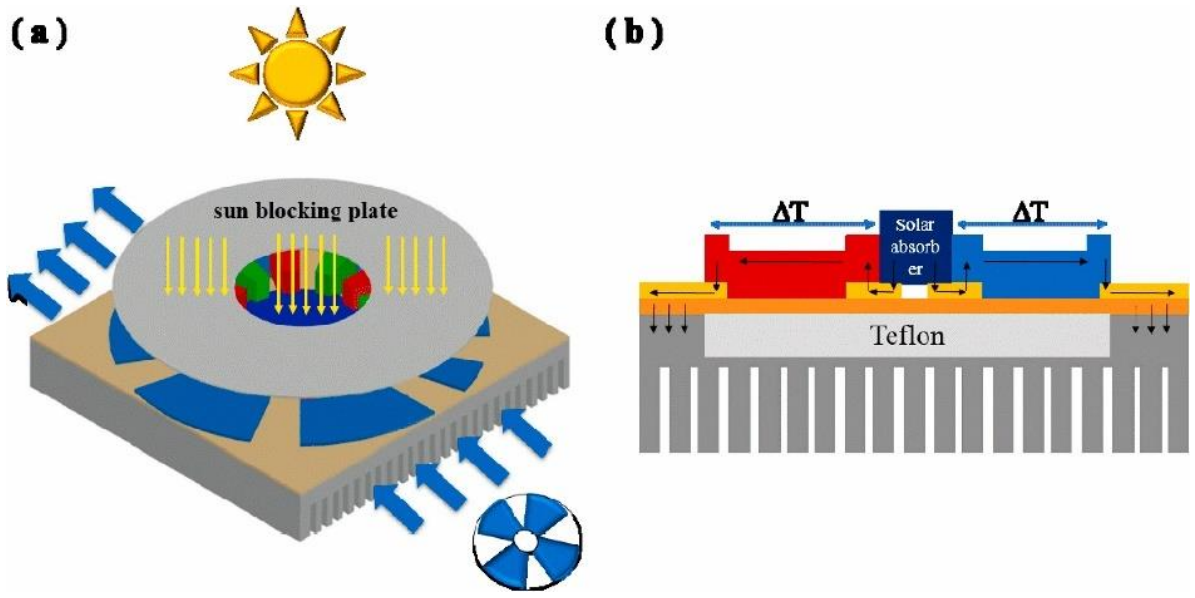

Figure 2.41: Schematic of the STEG wearable [84]

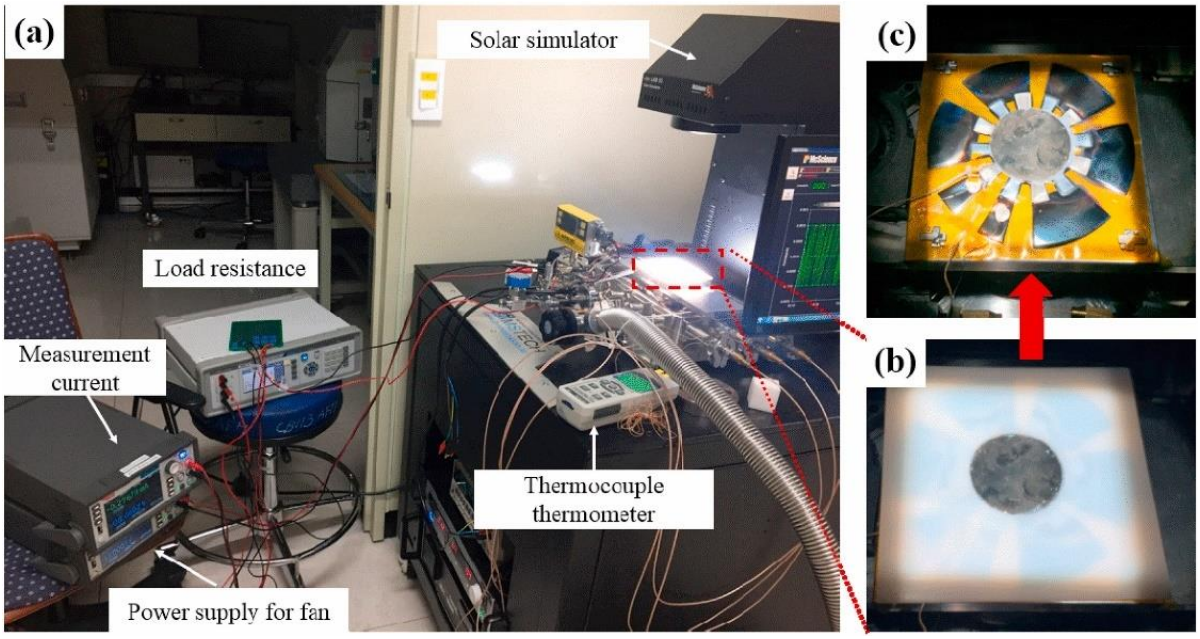

Figure 2.42: Experimental set up of the STEG wearable [84]

The above set up has some noteworthy characteristics in comparison to the set up established in this work. The proposed design was also tested indoors while using a lamp as a heat source. The thermometer was designed and connected using voltage regulators as heat sensors in an Arduino which was coded to measure and display the inner and outer temperatures of the TEGs on an LCD screen. Instead of a forced convection method to cool off the 'cold side', the proposed design utilises natural convection by testing the sheet in a vertical position.

Multimeters were used to measure and display the resultant voltages and currents. The experiments were recorded, and the acquired data was logged manually on Microsoft excel and the data is further analysed and presented using MATLAB.

A human-body based wearable device designed and tested by Wahbah, et al. [107] on a human wrist achieved an output voltage of $12mV$ at a P_{max} of $20\mu W$ when the ΔT across the TEG was a mere $0.5°C$. These output readings would have significantly increased if the experiment was conducted outdoors while the wearer was walking, due to a larger temperature difference obtained between a heated-up, active body and a wind exposed wearable. A picture of the TEG-based wearable with heatsink during prototype test is shown in Figure 2.43.

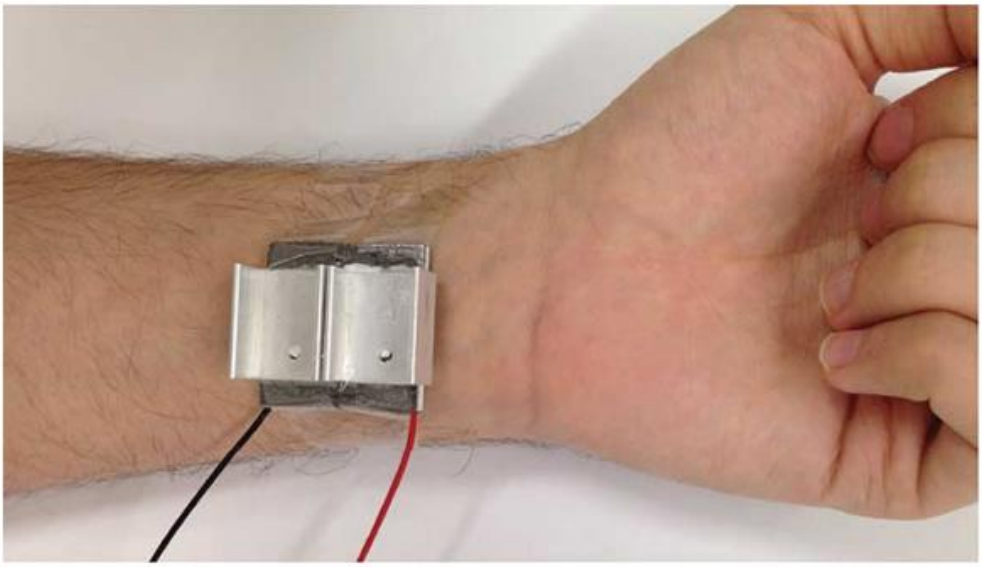

Figure 2.43: The TEG-based wearable with heatsink [107]

Proto, et al. [108] investigated the performance of a new-age flexible TEG-based wearable placed at four large skin locations on the body while wearers conducted daily activities. A 3cm×3cm TEM was encapsulated in a band which allowed for proper contact of skin and the TEG. A power output ranges from 5-50μW was generated.

Leonov [109] went a step further and integrated a TEG into a store-bought office shirt and ran field tests. It was found to generate 0.5-5 mW of power under ambient temperatures of $27°C$ and $15°C$ respectively. The TEG consists of a 5 mm thick and 3 cm wide round, hot plate with 256 BiTe thermocouples and cold plate of 40×30×1 mm dimension, encapsulated in polyethylene. The thermoelectric shirt produced a higher energy range over a span of 9 months, than its' similar sized competitive alkaline batteries. It was also concluded that the

thermoelectric shirt serves as a reliable power supply for wearable electronics of low-power requirement. A picture of four thermopiles assembled on the shirt fabric, where the remaining four are sewn and glued onto the reverse side, can be seen in Figure 2.44.

Figure 2.44: TEG integrated textile with four thermopiles assembly [109]

In summary, it may be seen that TEGs are indeed a potential method in harvesting energy. Literature that explored and investigated TEG parameters such as the investigation of ΔT readings achieved, the electrical arrangements of TEGs for required power output, the components utilized in the system during experimentation, and research methodologies adopted was discussed. While the power output per TEG tile is small in magnitude, further advancements in TEG technology may allow for higher efficiency and hence, a better power output.

3 Design and experimentation

3.1 STEG based roof sheeting design components.

This chapter highlights the key design features, equipment and components involved in the proposed design. The component selection process was also elaborated on, and necessary images are provided to establish an understanding of the system presented in this design. The design was broken down into 3 major design components. Figure 3.1 shows the major components in the TEG system design. Figure 3.2 shows the top view of the TEG system.

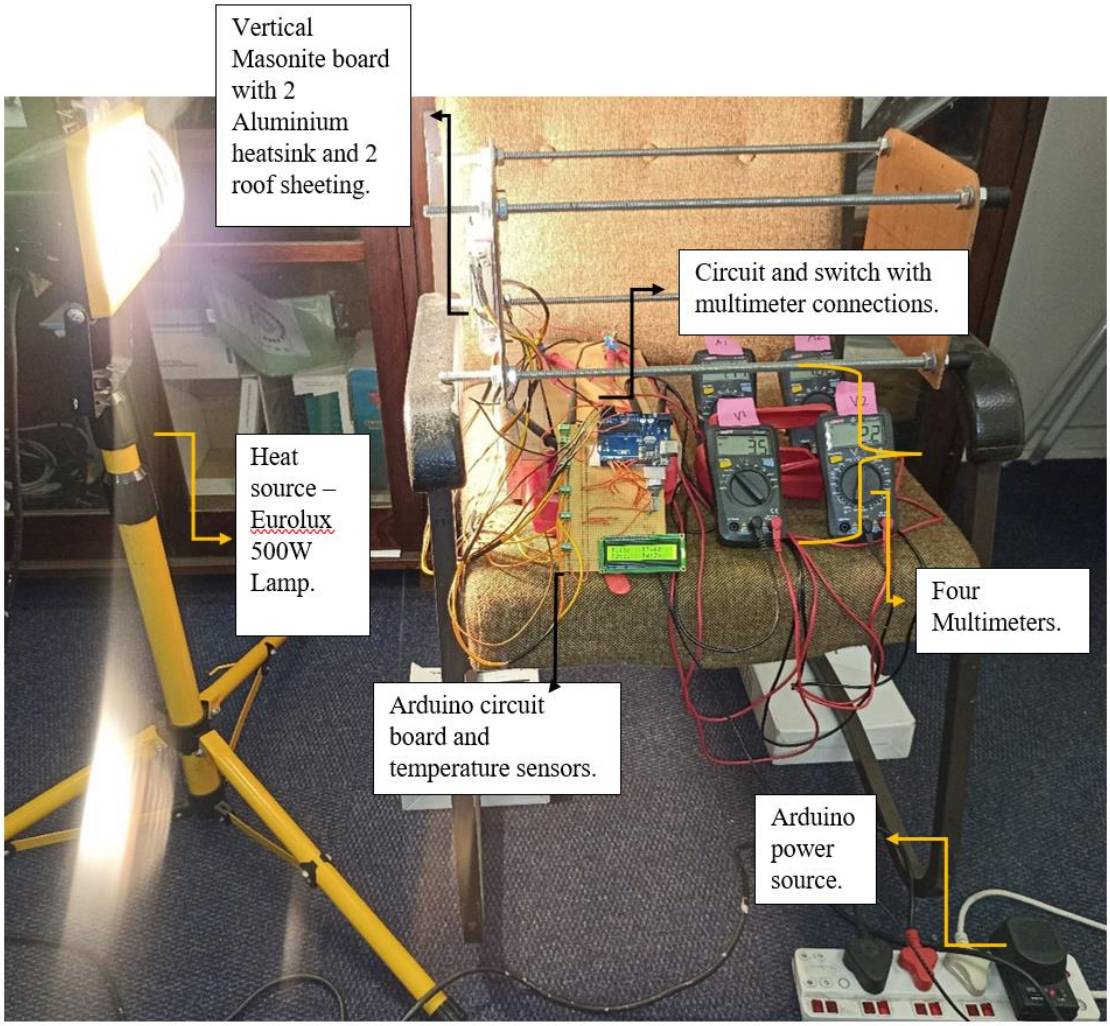

Figure 3.1: Labelled picture of the experiment apparatus during testing

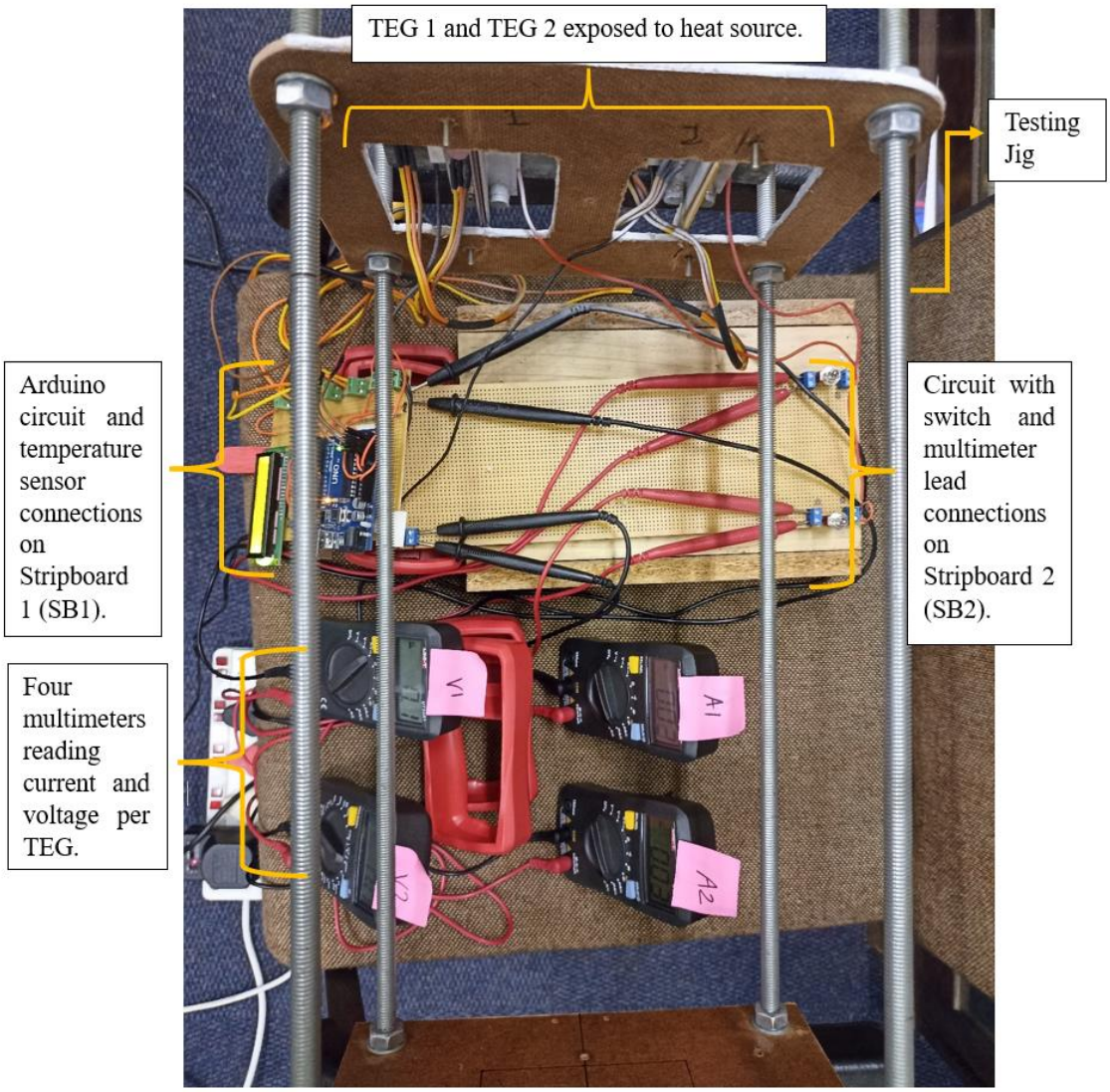

Figure 3.2: Top view of the major components in the TEG system

3.1.1 Testing jig and IBR sheeting.

The proposed TEG system consisted of two vertical TEGs, which were exposed to the heat source. Each TEG was comprised of a square IBR galvanised sheet, attached to the hot side of a TEM and 2 Aluminium L-Bars, facing back-to-back, were attached to the cool side of the TEM. The dimensions chosen for the experiments will be elaborated on in the IBR sheeting sub-chapter 3.2.2.3 to follow.

An off-set fixed onto the reverse side of the vertical Masonite board allows for the L-bars to be positioned, back-to-back and are secured in place using strong circular magnets. This can be seen in Figure 3.3 and 3.5. The off-set was built using wooden sticks attached to the Masonite board via L-Bracket corner braces. Magnets were used to secure the Aluminium L-Bars onto

the off-set due to their conductive nature and ease of application. The magnet location and system layout may be seen in Figures 3.5 and 3.7.

3.1.2 Arduino microcontroller and temperature sensors (SB1).

A stripboard is a widely used type of prototyping board for circuit building with regular grid holes and parallel strips of copper cladding. These boards are used to permanently assemble circuit prototypes. Connections may be made by soldering electronic components onto the stripboard.

Each TEG has a pair of LM35 temperature sensors, of which one sensor is placed on the reverse side of the sheet (T_h) and the other is placed on the heat sink (T_c). These sensors were secured in place using magnets. The temperature sensors were wired and connected into the terminals on a copper strip board (SB1). SB1 was comprised of an Arduino Uno, an LCD screen, 4 temperature sensors, 6 terminals, a 220 Ω resistor and a potentiometer. An Arduino microcontroller was coded to display the corresponding temperature measured by the temperature sensors in degrees Celsius. Figure 3.2 shows SB1 in the TEG system during experimentation. Figure 3.3 demonstrates the temperature sensor locations and its' corresponding data reading.

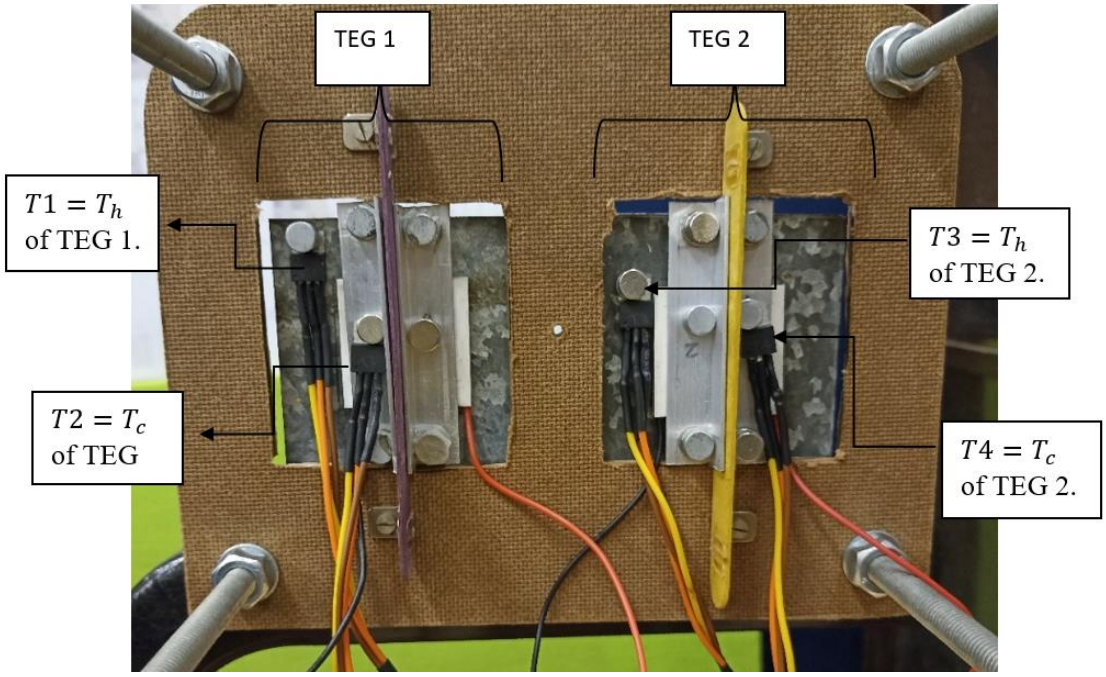

Figure 3.3: Photograph of the reverse side of the TEG system

3.1.3 Circuit with switch and 4 Multimeters (SB2)

SB2 is another stripboard comprised of terminals for the leads, which formed a circuit with a switch. This circuit was completed using 4 pairs of Multimeters leads. The two Multimeters were connected and set to measure the voltages generated per TEM and two Multimeters were connected to measure the currents generated per TEM. SB2 may be seen in Figure 3.2.

3.2 Design components selection and material selection.

In this sub-chapter, the design component and material selection are discussed. The focus is to elaborate on the considerations and decisions involved in selecting suitable components for the intended operation. The various design components of the system are broken down, inspected, and discussed. This sub-chapter aims to offer a comprehensive understanding of the design development.

3.2.1 Heat source

A 500W Eurolux flood lamp was used as the heat source for the indoor experiments. The selected lamp is available commercially.

3.2.2 Testing jig and IBR sheeting of the TEG system.

The testing jig utilised in this research was designed to position the square roof sheeting in a vertical manner while exposing one side of the roof sheeting to the heat source and shielding the reverse side from direct heat. Cut-outs on the vertical surface, sized to fit the sheets resting on an offset, allowed for this. At the same time, to prevent malfunction due to overheating, the electronic components were required to be shielded from direct heat. To fulfil this, the major electronic components were placed on the “cool side’ of the jig. Figure 3.6 illustrates the isometric view of the testing jig, coupled with the IBR sheeting.

3.2.2.1 Vertical surface

Since scalability is one of the three factors being tested in this research, precise surface area measurements of IBR sheeting where heat absorption and transfer occurs, were considered. Therefore, the material chosen for the vertical surface which held the TEGs, was Masonite, due to its relatively ideal insulating properties. This drastically reduced heat transfer that may have occurred on the surface exposed to the heat, other than on the roof sheeting being tested. Furthermore, the surface of the Masonite board that was exposed to the heat source was painted matte white to reduce heat transfer. The IBR sheeting position was chosen to be vertical to facilitate natural convection, which was elaborated on in chapter 1.1.3.

3.2.2.2 Steel thread bars

Four threaded steel bars were used as support mechanisms for the Masonite board. Another Masonite board situated at the end of the steel bars completed the jig design. A length of 500 mm was chosen for the steel bars as this was the width of the chair on hand, upon which the jig was meant to rest horizontally during experimentation. The lamp heat source' height was adjusted to face perpendicularly to the roof sheeting.

3.2.2.3 IBR sheeting

Standard IBR galvanized roof sheeting discussed in chapter 1.1.2 was used in this research due to its ideal flat surface size. The 103 mm surface shown in Figure 1.2 would be ideal for the selected TEM to fit on. However, the flat surface, devoid of any curvature amounts to ±90 mm. Hence, an 80 mm×80 mm square IBR sheeting, each, was selected for the experiments. This is shown in Figure 3.4.

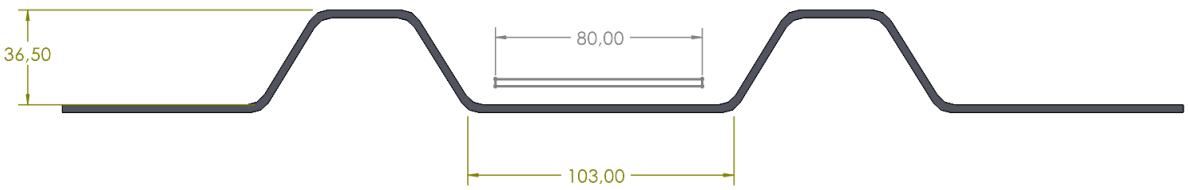

Figure 3.4: CAD cross sectional drawing of a standard IBR sheeting

The hot side of a TEM was attached to the IBR sheeting, using magnets. The characteristic behaviour and dimensions of the TEM chosen for this design, may be seen in Appendix A.

3.2.2.4 Heat sinks

Aluminium L-bars placed back to back, were used as the heat sink in this design as its light weight, non-magnetic, cost effective and good thermal conductive nature makes it ideal for this application [110]. For these purposes, Aluminium heat sinks are widely used and readily available. The shape of the L-Bars made this heat sink an ideal fit for this design as it allowed for the bars to be placed back-to-back and for magnets to hold them securely onto the off-set. Magnets were used to hold these heat sinks against the roof sheeting, with the TEM sandwiched between them. This can be seen in Figure 3.6 and Figure 3.8. This allowed for the 'hot side' of the TEM to be positioned flush, against the IBR sheeting and the 'cool side' of the TEM to be positioned against the heat sinks. The length of the heat sinks was the exact length of the IBR sheeting. Electrically connecting the TEGs vertically, allows for the aluminium bars to serve as

an electrical conductor as well to connect one TEM to another, thus completing the TEG system.

3.2.2.5 Magnets

It was vital to ensure that the heat received on the ‘hot side’ of the sheets does not transfer through any holes and mechanical fasteners to the ‘cool side’ of the TEG system. Since using magnets would not require drilling holes through the heat sinks or the sheets, heat will not be conducted via any metal bolts, nuts, or rivets, over to the cool side. Holes would compromise the weather proofing of the design; therefore, magnets were used instead. Furthermore, the lack of holes and mechanical fasteners in the surface area of the sheets exposed to the sun, prevents any effect on the scalability function of the design. Magnets are also simple to use, easy to position and connect the heat sinks onto the offset. Magnets were also used to position the temperature sensors onto the roof sheeting and heatsink quickly and without hassle.

A picture of the magnets and dimensions are shown in Figure 3.5 [111]. Figure 3.6 shows the locations of the magnets on the IBR sheeting and heat sinks. Four magnets were used to position the 4 temperature sensors and 16 magnets (double magnets placed on each end of the L-bar) were used to place the L-Bar heat sinks onto the offset (back-to-back) and simultaneously hold the TEM sandwiched between the heat sinks and roof sheeting.

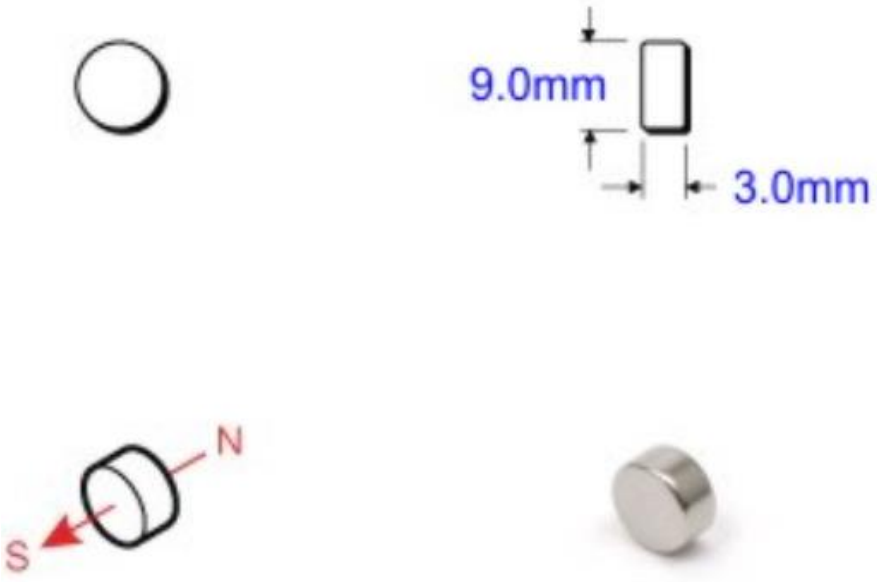

Figure 3.5: Selected magnet picture and dimensions

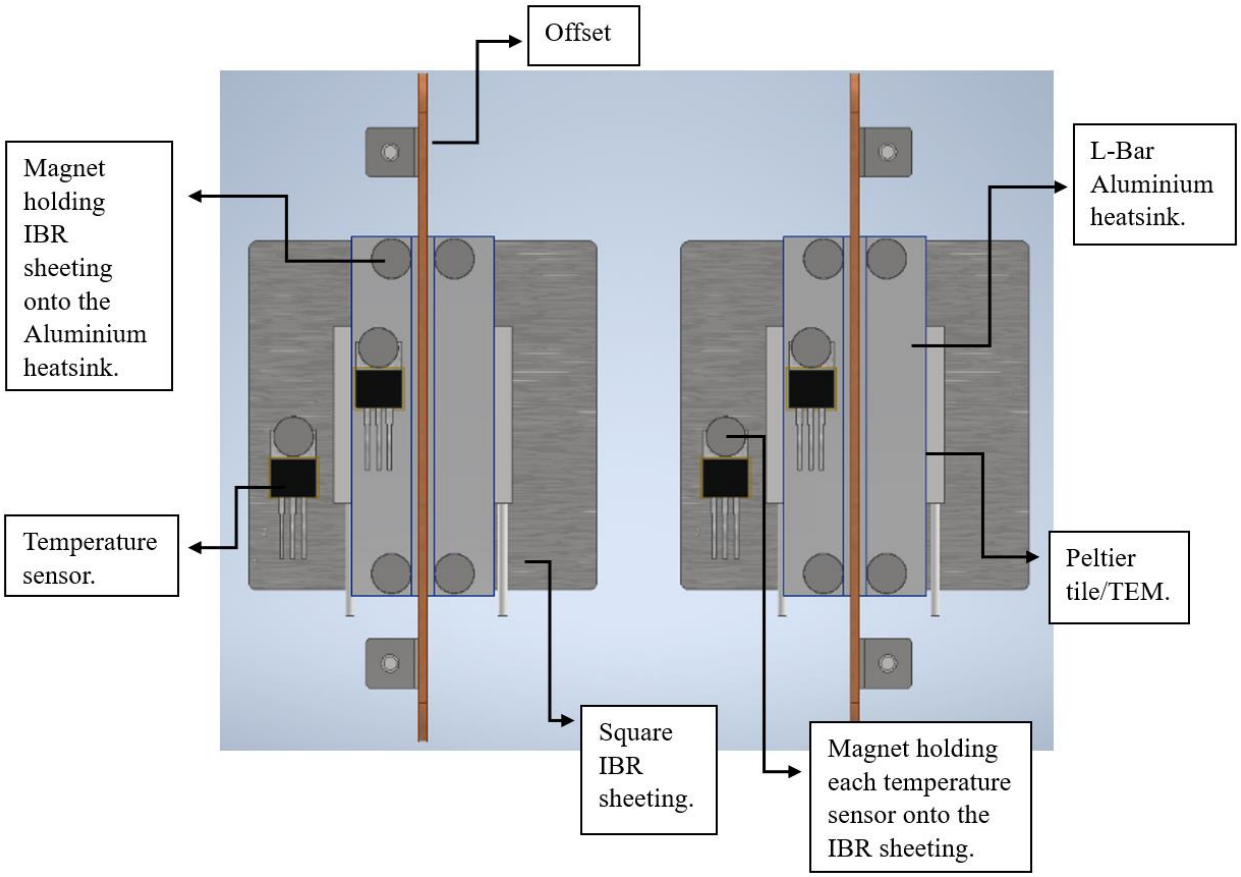

Figure 3.6: CAD drawing showing the position of magnets on the TEGs

3.2.2.6 Offsets

Wooden sticks were used to serve as the offset for the TEGs. Again, wood was chosen due to its relatively high insulating properties which would remove the possibility of any major unwanted heat transfer occurring. Figure 3.7 shows the complete isometric view of the TEG system's jig and coupled components. Figure 3.8 presents the focused CAD isometric view of the Masonite board, together with the offsets, heatsinks and TEMs. The IBR sheeting is made transparent for part viewing purposes. Figure 3.9 shows the side view of the jig with components.

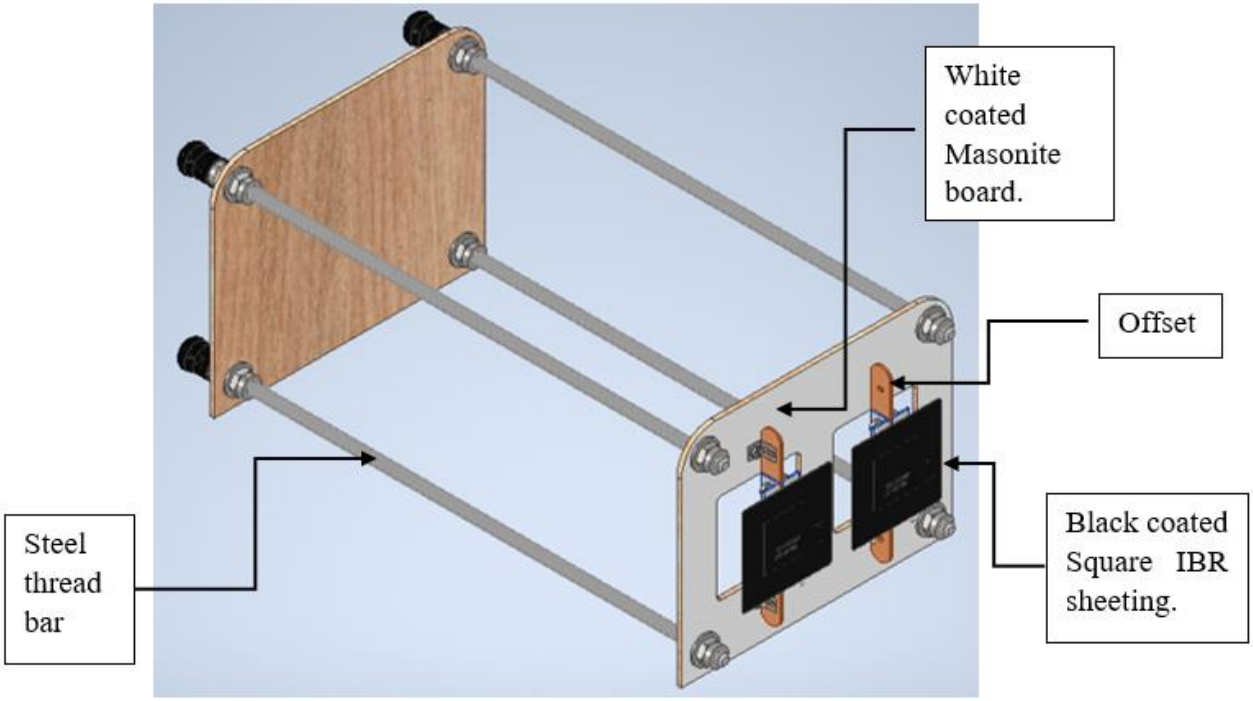

Figure 3.7: CAD drawing isometric view of the testing jig design with components

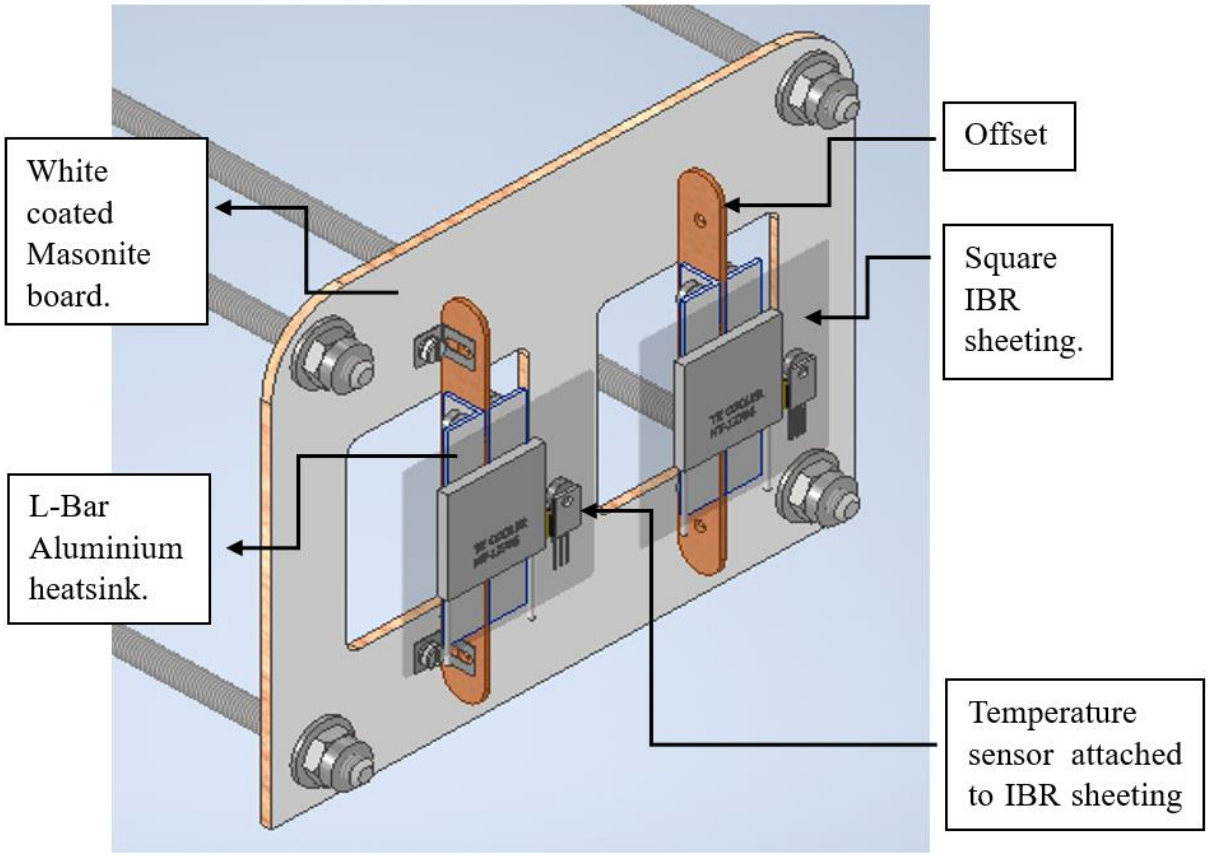

Figure 3.8: The focused CAD isometric view of the vertical Masonite board and coupled components

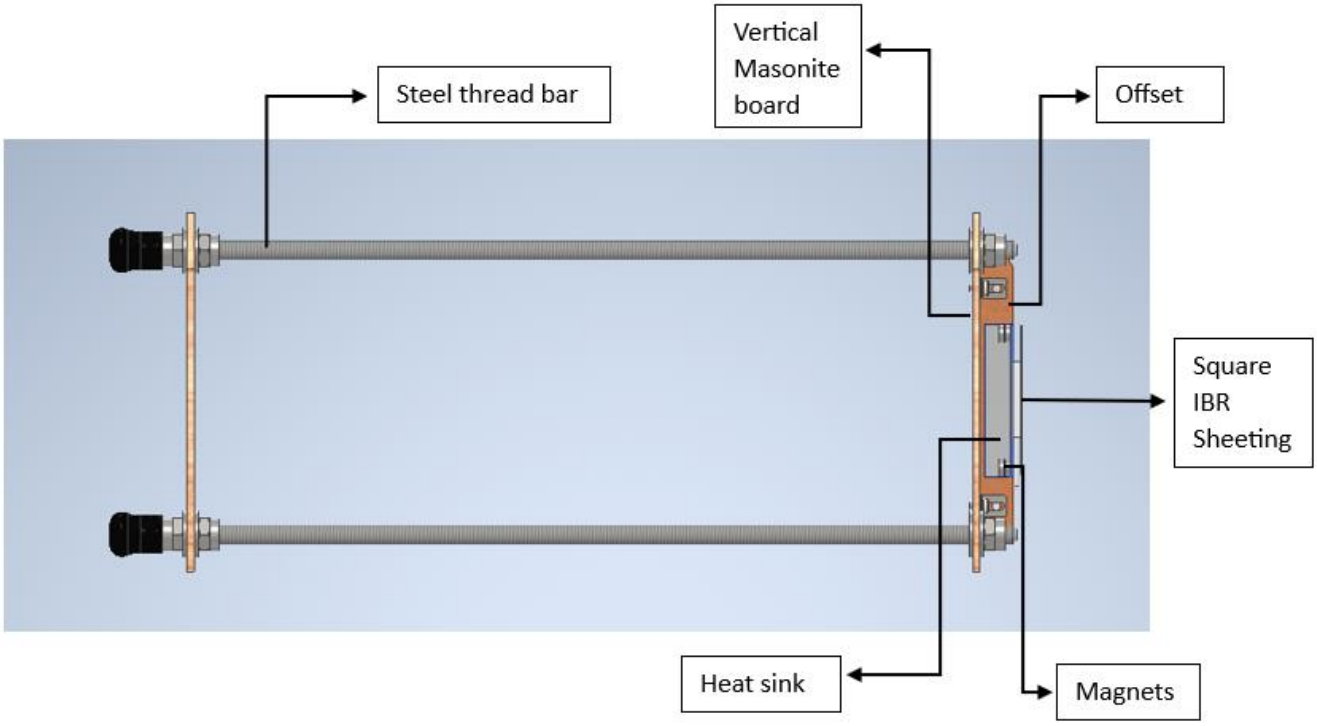

Figure 3.9: Side view of the jig design with components

3.2.3 Arduino microcontroller and temperature sensors (SB1).

3.2.3.1 Arduino Uno microcontroller and LCD screen

A programmable microcontroller was required to measure and display the temperatures of the TEG system. An Arduino UNO was chosen for this purpose due to its numerous advantages such as its' user-friendly nature, cost effectiveness, flexibility, it is an open source program and has an extensive software and hardware [112]. The technical parameters and picture of the Arduino Uno microcontroller are attached in Appendix B. The Arduino UNO was connected to SB1 via plastic spacers with adhesive, to prevent electronic interference.

The Arduino was connected and coded to read temperatures measured by four temperature sensors. These readings were displayed on the 16×2 Liquid Crystal Display (LCD) screen. The Arduino code that measures and displays temperatures are attached in Appendix C. A 16×2 LCD provided 16 columns and 2 rows of characters which displayed readings for T1, T2, T3 and T4. T1 and T2 are coded to be displayed one below the other and the same is done for T3 and T4. The character size of 16 columns and 2 rows is suitable for the required display of the four temperatures.

A potentiometer of 10 kΩ rating was required to adjust the contrast of the writing displayed on the LCD. This requirement was provided by the LCD connections followed on the Arduino

project page [113]. These components and their connections on SB1 may be seen in Figure 3.9. Figure 3.2 shows SB1 in the TEG system during experimentation.

3.2.3.2 Resistor

When connecting and wiring SB1, a resistor was required to limit the current through the LED backlight of the LCD screen. It was noted that connecting a resistor of 220 Ω was too high, since the backlight of the LCD was not bright enough for the display to be distinctly visible in the video recording of the experiment. A 120 Ω was then introduced into SB1 which then provided the correct amount of backlight brightness for clarity in the video recording.

3.2.3.3 Temperature sensors and calibration.

LM35DT temperature sensors were chosen as these sensors have a flat metal head which could be easily sandwiched between the roof sheeting and magnets for ease of application and cost effectiveness. The LM35DT working temperature range of ±0°C-100°C also suited the temperature requirements of the application. Appendix D provides the applications and electrical characteristics of the LM35DT temperature sensor. Further information on temperature sensors and the chosen LM35DT temperature sensor was provided in chapter 1.1.9.4. Figure 3.10 shows the electronic components and connections on SB1.

The calibration process involved testing the resultant temperature sensor reading at three known temperatures to establish a line equation for each sensor calibration. This converted the output reading of the sensor into the corresponding temperatures in the code. These temperature readings will be displayed on the LCD screen.

Two such stripboards were used in this design i.e., SB1 and SB2. The temperature sensors were connected on a stripboard, herein referred to as SB1. The code to display the readings on the LCD was run on Arduino Uno.

The apparatus utilised was a tin container, hot water, a temperature sensor attached to the outside of the container, a mercury thermometer to read the water temperature and a plastic spoon to stir.

The calibration process had the following steps:

1. The tin was filled with hot water and the temperature of the water was read using the thermometer. Temperature reading was noted.
2. The resultant reading from the sensor, at that temperature was also noted in units.

3. Steps 1 and 2 were repeated 2 more times to obtain a pair of 3 readings. For each iteration, more hot water was added to increase the temperature and the water was stirred before taking down the reading, to allow for a stable temperature reading.
4. The temperature was plotted on the x axis of a graph (in $°C$) against the output sensor reading (in units) on the y axis. Since the response of LM35DT is linear, the gradient m was calculated.
5. Using the remaining point of temperature vs unit, the remaining parameters of the line equation were established.

The equation was tested on the remaining 3 temperature sensors and necessary changes were made to the calibration equation corresponding to its temperature sensor. These equations were used in the code on Arduino UNO to convert the 4 sensor readings into real-time temperatures in degrees Celsius, which was then displayed on the LCD screen.

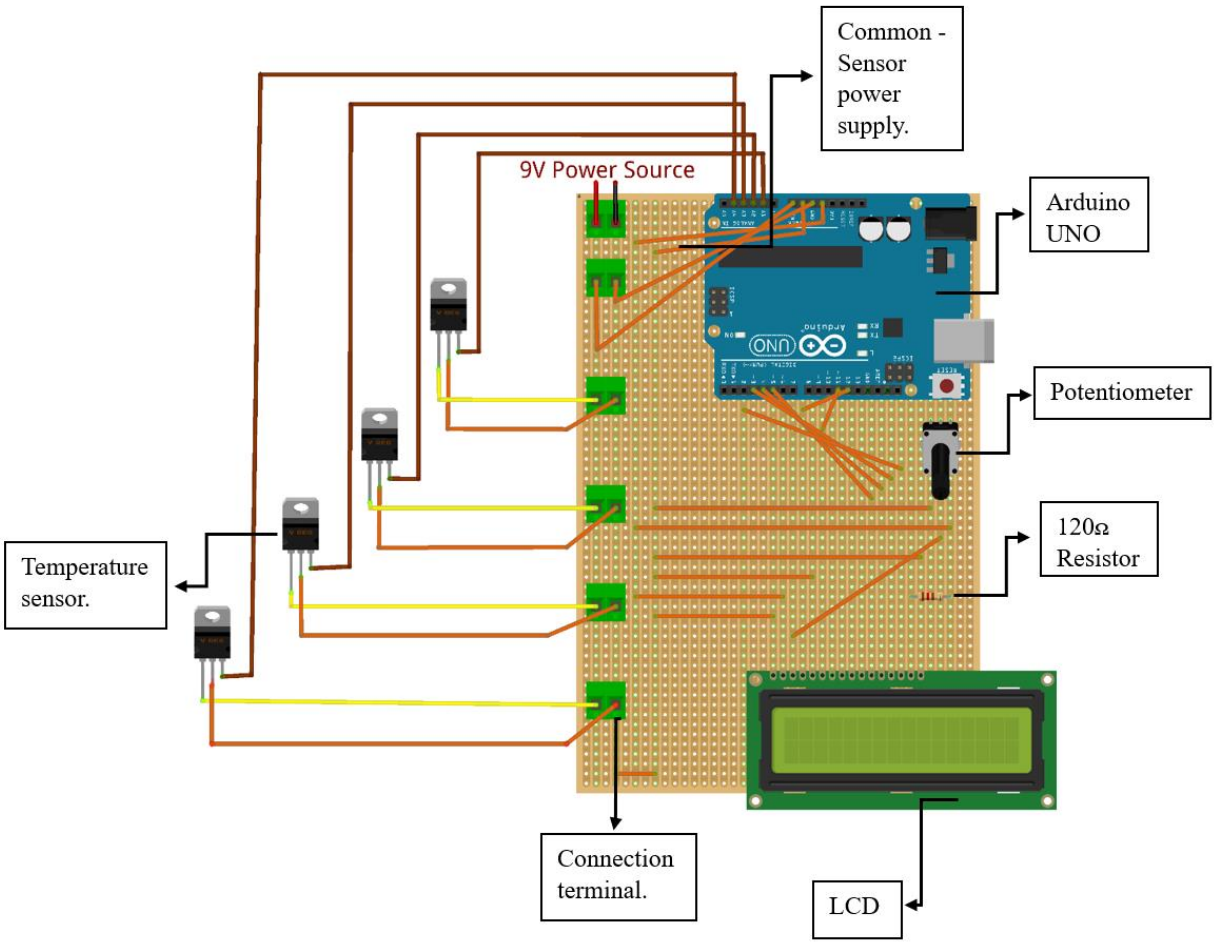

Figure 3.10: Illustration of wiring connections and electronic components on SB1

3.2.4 Circuit with switch and 4 Multimeters (SB2)

3.2.4.1 Switches

This research adopts the 4-step IV Curve generation method, used by Lashin, et al. [64] which requires a switch, to open and close the circuit, during experiments (Previously explained in chapter 2.5.1 on methodology adapted in this research and the required circuit connections). A two-way toggle switch was used to allow for the 'open or closed position' to be clear, as opposed to a button switch which would not show the positions.

3.2.4.2 Stripboard 2 (SB2)

The stripboard with terminals for connection of the TEMs, multimeter leads, and switches was used to build the circuit with switch and Multimeters on – Herein referred to as SB2. The 2 switches and 8 two-way terminals were soldered onto the SB2. SB2 can be seen in Figure 3.11, without a circuit connection.

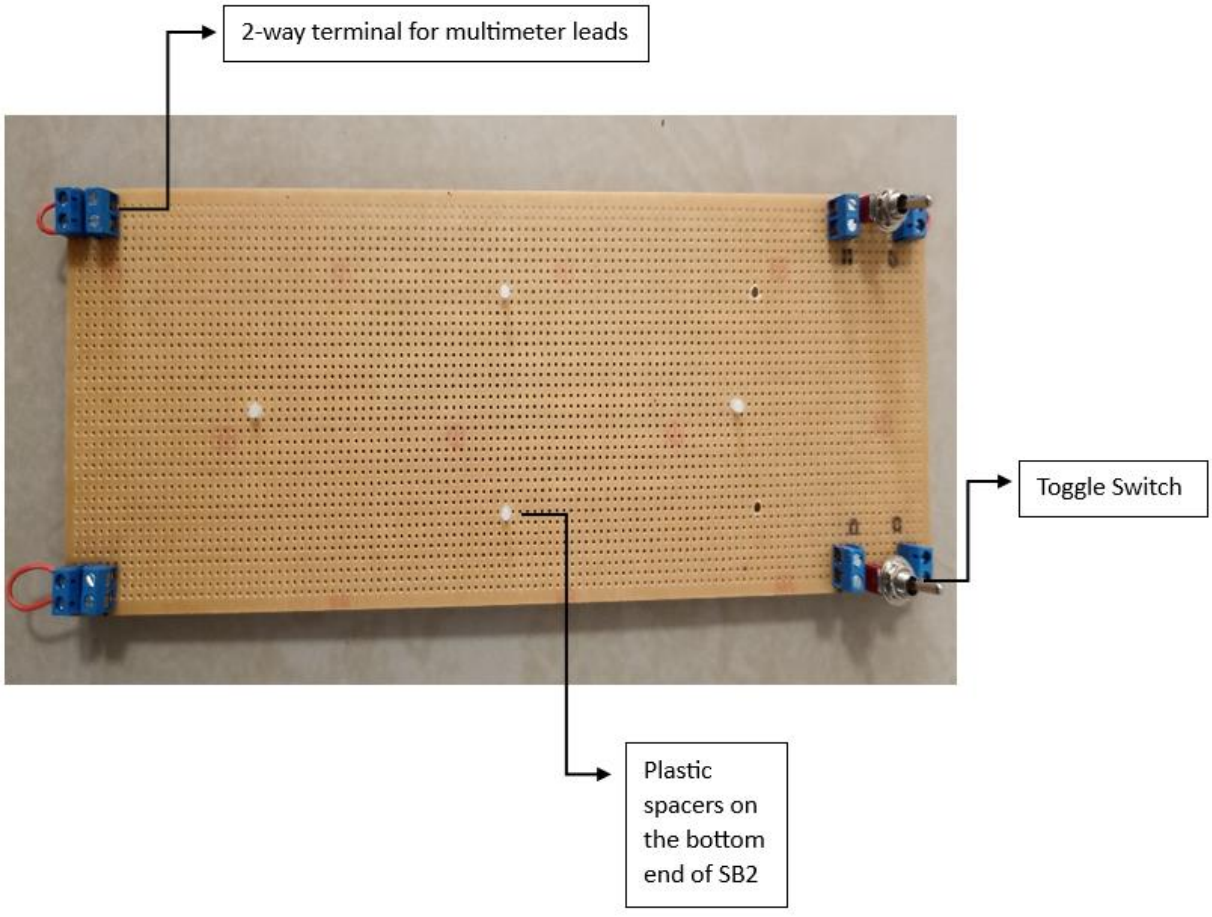

Figure 3.11: Photograph of the multi-purpose SB2 without a configured circuit

A TEM can be connected onto SB2 as a unit. For the unit configuration, a toggle switch was needed. SB2 had 4 plastic spacers drilled onto the reverse side to prevent electrical interference

when placed on a surface during experimentation. Figure 3.12 shows the circuit diagram connected onto SB2 as a unit.

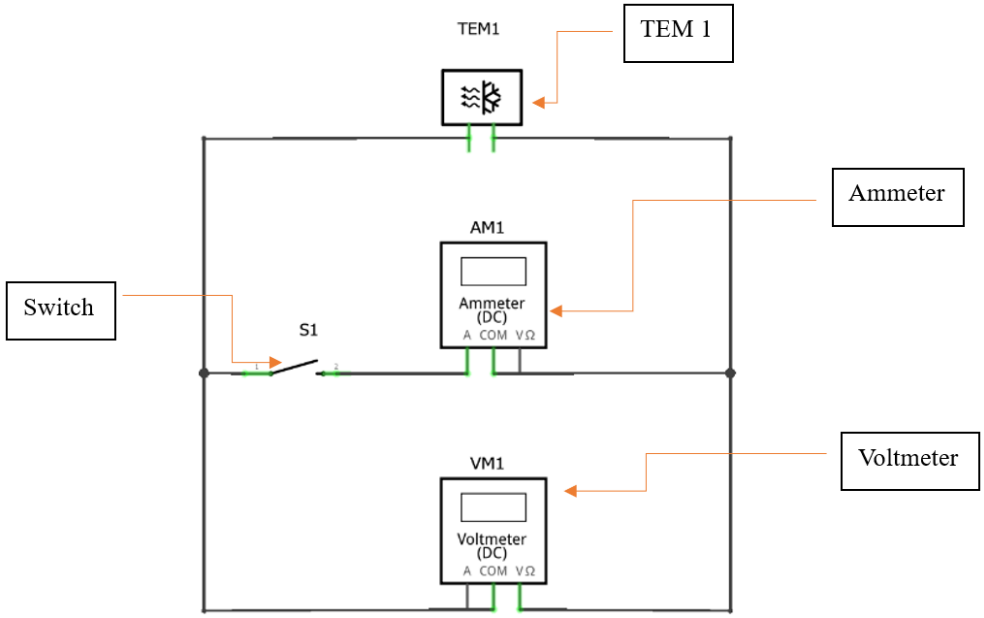

Figure 3.12: Circuit schematic diagram illustrating TEM1 connected onto SB2 as an independent unit

However, for the series and parallel arrangements of TEMs on SB2, the circuits displayed in Figure 3.13 and 3.14 respectively, were wired and connected using 0.34 mm solid wire, terminal blocks for nodes, alligator clips and a large push button switch.

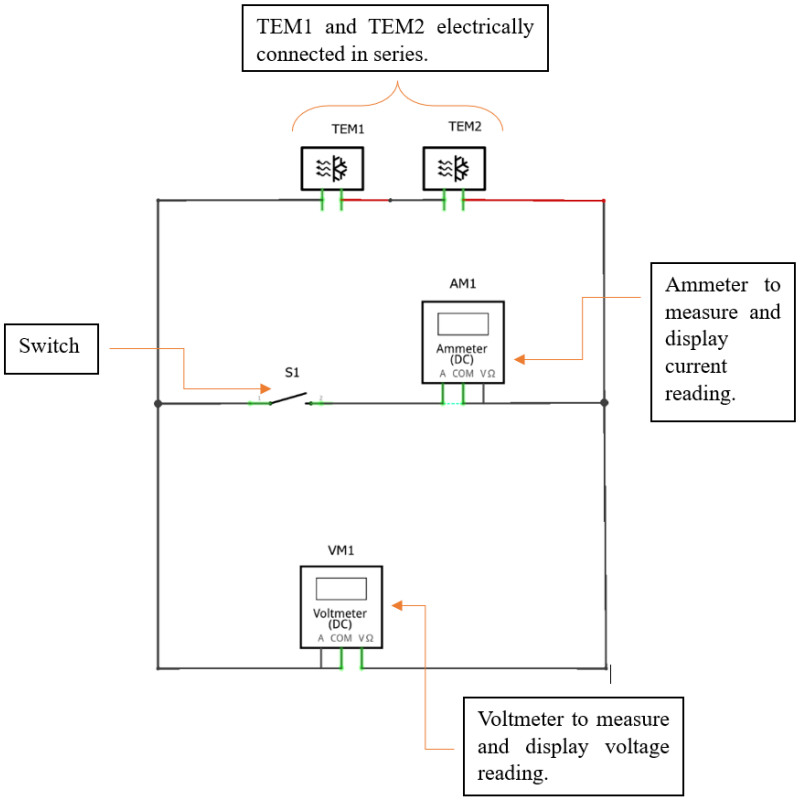

Figure 3.13: Circuit diagram of SB2, when 2 TEMs are electrically connected in series arrangement

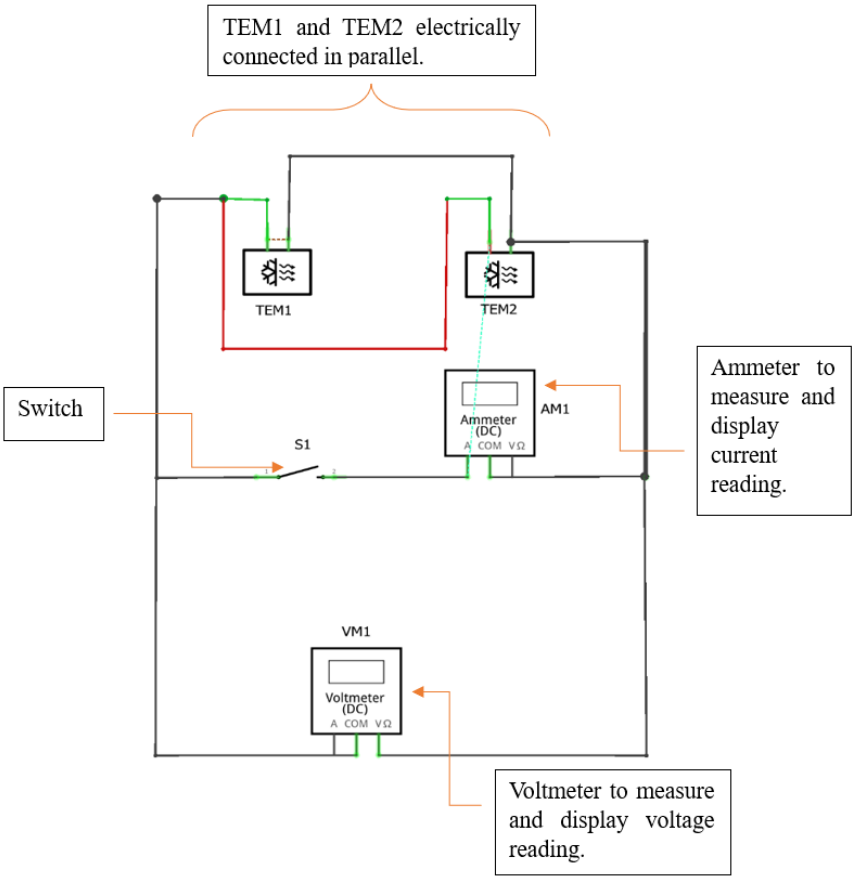

Figure 3.14: Circuit diagram of SB2, when 2 TEMs are electrically connected in parallel arrangement

3.2.4.3 Multimeters

Four UNI-T UT33+ series palm size Multimeters were used for measuring critical voltage and current readings generated by the TEG.

3.2.5 TEG1 and TEG2

Each TEG ensemble was comprised of the IBR sheet, a TEM, 2 aluminium L-Bar rods faced back-to-back to form a heatsink, 2 temperature sensors connected to SB1 and the required number of Multimeters (depending on the electrical configuration of the TEMs) connected on SB2. Both TEGs were exact replicas and were run simultaneously under the same conditions. The choice of IBR sheeting was discussed in chapter 3.2.2.3 and is illustrated in Figure 3.4. When unit configuration experiments are run, TEG1 is used in the set-up.

3.3 Testing methodology

The following testing methodology was adopted in this research to study and analyse the 2 parameters tested i.e., The effect of roof sheeting colours on power output and the most effective

electrical arrangement for scalability. The experiments were broken down into 3 phases, where each phase tested different variables. Phase 1 tested the colour variable while varying the distance from the heat source to the sheeting. Phase 2 was an outdoor experiment that aimed to achieve realistic data on the expected temperature gradient (ΔT) which may be achieved under the sun. Phase 3 tested the ideal electrical connections of TEMs for maximum power output of the TEG system. Electrical connection of the TEM as a unit, two TEMs in series and two TEMs in parallel were tested. Phase 3 allowed for a foundational understanding on the best type of electrical arrangement required, for maximum power output, when TEMs were scaled up.

3.3.1 Phase 1 – Colour and distance varied indoor experiments.

Galvanised, white, and black were chosen as the test colours because the proposed research may have a possible application of generating power on the sheeting of large warehouses. These warehouses are either galvanised or painted white to help cool the warehouse [3]. The colour black was introduced to test whether coating the sheeting black would enhance the power output.

The starting point of the experiments carried out entailed running a series of 9 indoor experiments. The galvanised roof sheeting was exposed to the heat source at 3 distances i.e., 300 mm, 600 mm and 900 mm. TEG1 was connected on SB2 as an independent unit and the 4-step, IV curve generation method from chapter 2.4.1 was followed. The distance varied experiments were then repeated for the remaining colours of roof sheeting. The data was continuously acquired. In addition to the data achieved by this method, the corresponding ΔT values were also video recorded, and the generated parameter readings were logged manually.

The output power generated during each switch was calculated on a spreadsheet in Microsoft Excel. The effect of distance (between the heat source and the TEG system), and the effect of the 3 colour sheets on the output power generated by the system was then analysed. One such colour and distance varied experimental set-up is shown in Figure 3.15. Table 3.1 presents a summary of experiments run in phase 1.

Figure 3.15: A picture of the TEG system with black coated roof sheets in closed circuit position during experiments at 600 mm

Table 3.1: Summary of experiments run in phase 1.

Experiment number	Roof sheeting colour	Distance between TEG and lamp(mm)	Electrical configuration	Outcome parameters
1	Galvanized	300	Unit	ΔT, V_o, I_s and the resultant P_{max} derived from the TEG.
2		600		
3		900		
4	Black	300	Unit	
5		600		
6		900		
7	White	300	Unit	
8		600		
9		900		

Figure 3.16 shows pictures of the 3 different colour coated sheets in phase 1 testing, whereby, a.) Galvanised, b.) Matt white coated sheets and c.) Matt black coated sheets

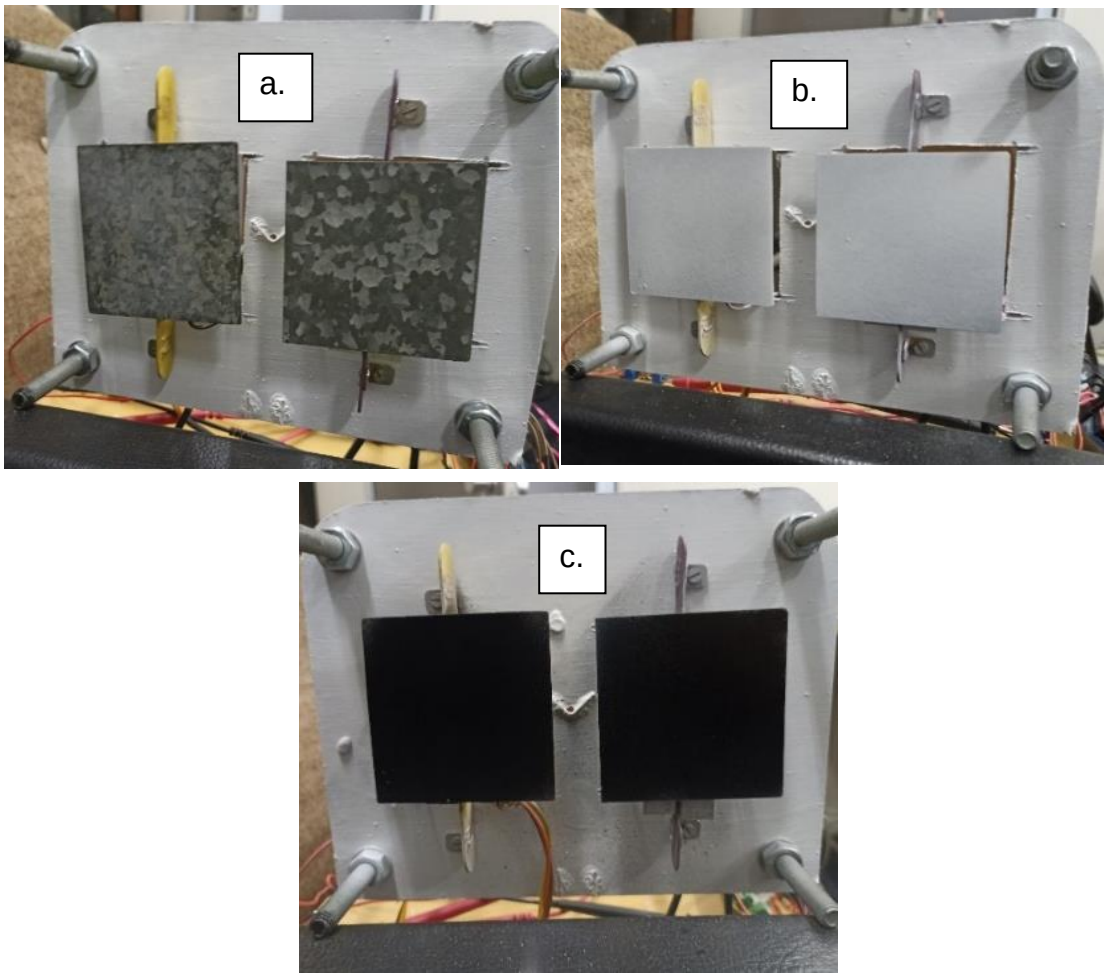

Figure 3.16: Pictures of the 3 different colour coated sheets in phase 1 testing

3.3.2 Phase 2 – Outdoor weather conditions

Next, to achieve realistic data on the expected ΔT range in the sun, the experiment of black sheets outdoors when exposed to sunlight was run. The same experiment set-up which was used in phase 1 was then shifted outside, under the sun. The resultant ΔT readings over a span of 150 minutes were acquired. Figure 3.17 shows pictures of the outdoor experiment in phase 2 whereby a.) Side view of the set up outdoors, b.) Front view of TEG system exposed to sunlight. Table 3.2 shows a summary of the experiment run in phase 2.

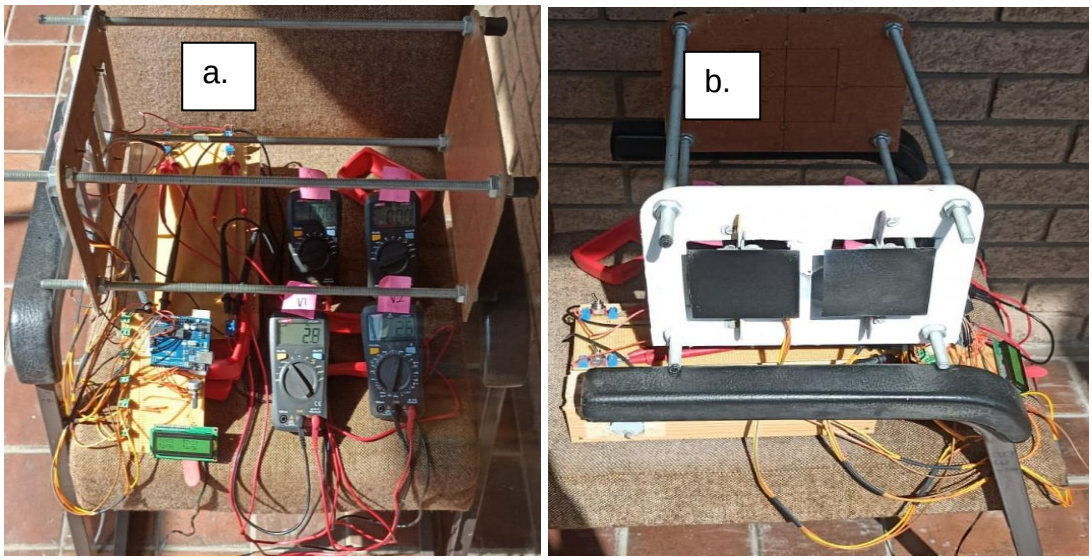

Figure 3.17: Pictures of the outdoor experiment in phase 2

Table 3.2: Summary of experiments run in phase 2

Experiment number	Roof sheeting colour	Electrical configuration	Outcome parameters
1	Black	Unit	T_h, T_c and ΔT achieved by the TEG over a span of 150 minutes.

3.3.3 Phase 3 – TEM arrangement for maximum power output and scalability

The TEG was then set-up using the colour sheet that performed best i.e., generated the highest P_{max}. The TEM was connected electrically as a unit and was run indoors at the three distance variations i.e., at 300 mm, 600 mm and 900 mm. The same was done for the remaining 2 arrangements, i.e., 2 TEMs electrically connected in series and then 2 TEMs electrically connected in parallel. The resultant power output from each distance and configuration was studied, compared, and analysed. This was done to extract the best possible electrical arrangement of TEGs, when scaled up, for maximum power generation.

The results from this experiment may also predict the expected solar power generated when electrically connected in the 'ideal' electrical arrangement for maximum power output. Table 3.3 shows a summary of the experiment run in phase 3.

Table 3.3: Summary of experiments run in phase 3

Experiment number	Roof sheeting colour	Distance between TEG and lamp(mm)	Electrical configuration	Outcome parameters
1	Black	300	Unit	ΔT, V_o, I_s and the resultant P_{max} derived by the TEG.
2		600		
3		900		
4	Black	300	Series	
5		600		
6		900		
7	Black	300	Parallel	
8		600		
9		900		

4 Results and analysis.

In this section, the results and findings established from this research are graphically displayed, analysed, and discussed. The data presented is supported using graphs and charts in the "data presentation" sub-section. The results and data are then analysed and discussed in the "findings" sub-section. This is done for each phase of experiments carried out in this research.

4.1 Phase 1 – Colour and distance varied indoor experiments.

Galvanised, white, and black were chosen as the test colours because the proposed research may have a possible application of generating power on the sheeting of large warehouses. These warehouses are either made with standard galvanised sheeting or are painted white to help cool the warehouse [3]. The colour black was introduced to test whether coating the sheeting black would enhance the power output. The temperature absorbed by the system was varied by varying the distance between heat source and the TEG system.

4.1.1 Data presentation

Figure 4.1 graphically displays the P_{max} vs ΔT data acquired from phase 1 of the experiments as a bar graph. The colour and distance variations have been shown on the x axis where:

- G300-Galvanised sheet at 300 mm away from the heat source.
- G600-Galvanised sheet at 600 mm from heat source.
- G900-Galvanised sheet at 900 mm from the heat source.
- W300-White coated sheet at 300 mm from the heat source.
- W600-White coated sheet at 600 mm from the heat source.
- W900- White coated sheet at 900 mm from the heat source.
- B300-Black coated sheet at 300 mm from the heat source.
- B600-Black coated sheet at 600 mm from the heat source.
- B900- Black coated sheet at 900 mm from the heat source.

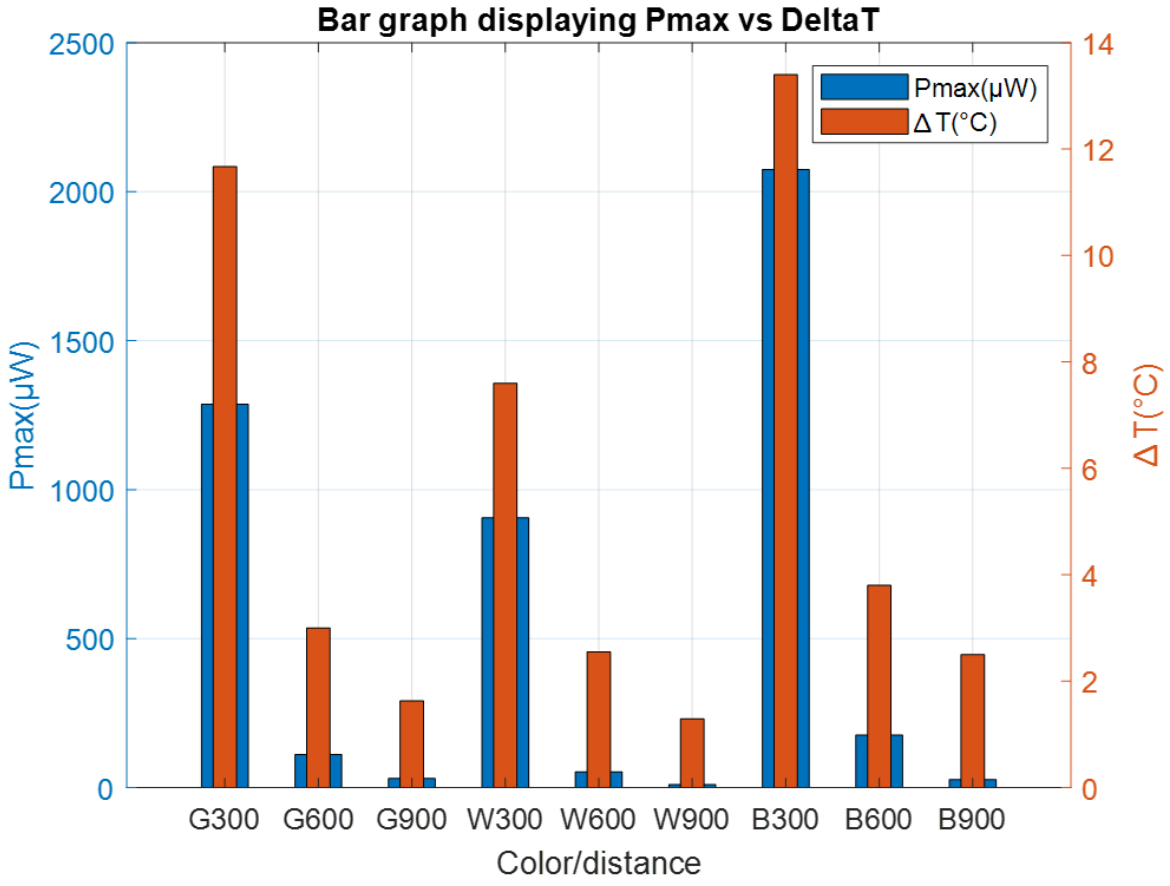

Figure 4.1: Graph displaying averaged results obtained for the colour and distance varied tests

The dual y-axes display the corresponding P_{max} values of the blue bars on the left-hand side y axis and the corresponding ΔT values of the orange bars on the right-hand side y axis. P_{max} and ΔT is measured in microwatts (μW) and degrees Celsius ($°C$) respectively. The TEG1 experiment consists of 10 data sets per switch (derived from the IV curve generation method from chapter 2.4.1) that were averaged into a data pair (ΔT and corresponding P_{max}) for each colour/distance experiment shown on the x axis.

4.1.2 Findings

The primary outcome was that the black coated sheets of TEG1 outperformed both the galvanised and white coated sheets. The black sheets positioned at all 3 distances had a higher output ΔT and resultant P_{max}, than the comparative galvanised and white coated sheets, at the same distances. The black sheets performance was then followed by galvanised sheets and then white coated sheets. This is an expected outcome due to the findings established by Ehsan and Kianmehr [14]. This behaviour is also in line with the principle that the colour black in general will absorb heat entirely, thus achieving the highest temperature [15].

It is noteworthy that the galvanised sheets outperformed the white sheets. It can be concluded that when this TEG is applied to the warehouse side roofing and wall cladding, an optimum output may be established by coating the roof sheeting with a matte black paint.

4.2 Phase 2 – Outdoor weather conditions

To achieve realistic data on the expected ΔT range outdoors, the experiment of black sheets when exposed to the sunlight was run. The results are presented and discussed.

4.2.1 Data presentation

Figure 4.2 graphically displays the T_h, T_c and ΔT solar data acquired from phase 2 of experiments as 3-line graphs on the same axes. A black coated IBR sheet was used in this experiment, since the black coated sheets achieved the highest output in phase 1. The x axis displays the time lapse in minutes, over a span of 150 minutes, and the y axis displays the resultant ΔT generated by the TEG in the sun. The solar experimental data displayed in the graph outlines the TEG's characteristic behaviour in accordance with its temperature parameters throughout the span of 150 minutes on a cool day.

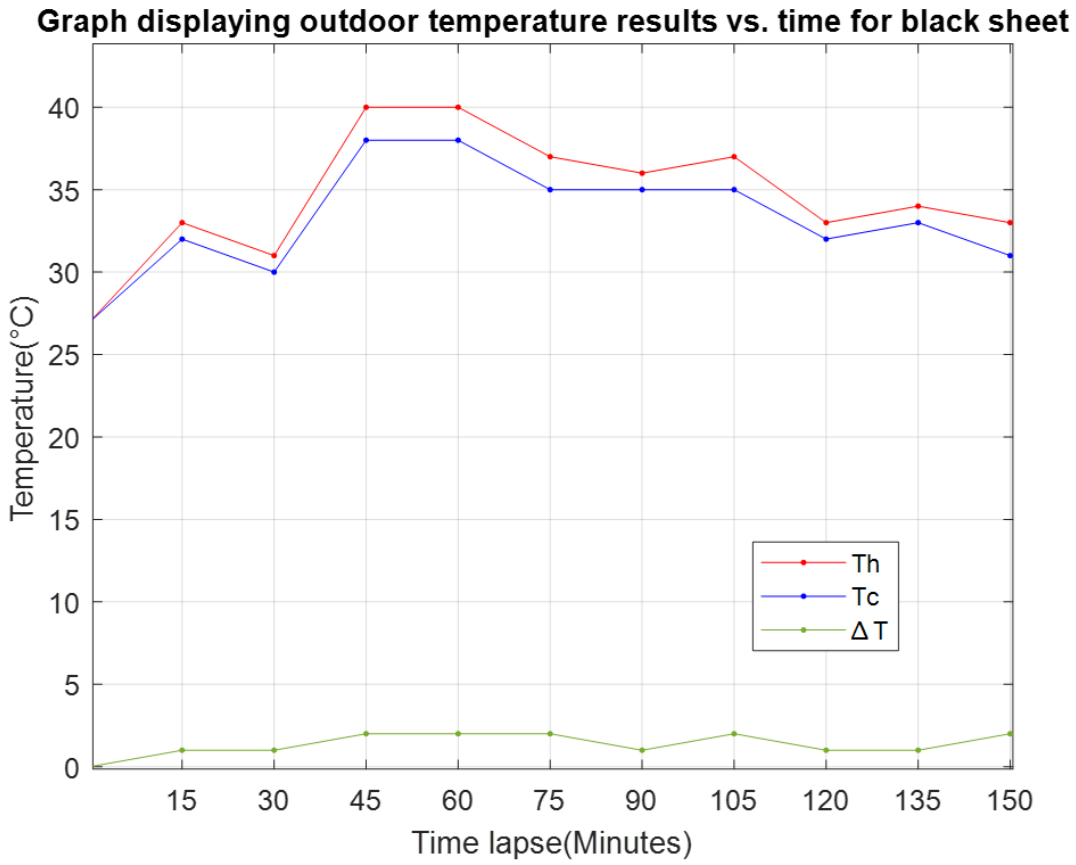

Figure 4.2: Graph displaying temperature vs time results obtained outdoors on a cool day when the experiment was run for 150 minutes

4.2.2 Findings

Since the output ΔT was found to be relatively consistent in a range of 1-2$°C$ in the experiment, it was found that the aluminium L-bars performed well as heat sinks. This verified that Aluminium is a well suitable metal to be used as a heatsink since it has a high thermal conductivity [17], previously discussed in chapter 1.1.6. An average T_h, T_c and ΔT over a span of 150 minutes of 34.55$°C$, 33.19$°C$ and 1.35$°C$ was established in the sun on a cool day, respectively.

4.3 Phase 3 – TEM arrangement for maximum power output and scalability.

The experiments in phase 3 were carried out to extract the best possible electrical arrangement of TEGs, when scaled up, for maximum power generation. This sub-chapter presents the data and discusses the scalability of a TEG unit, 2 TEMs connected in series and 2 TEMs connected in parallel.

4.3.1 Scalability of TEG as a unit, in series and in parallel.

4.3.1.1 Data presentation

It was found from phase 1 that the black coated sheets greatly enhanced the TEG output. Therefore, the experimental set up for phase 3 utilised black sheets to test for the 'ideal' electrical arrangement of TEGs for maximum output.

Figure 4.3 graphically displays the acquired data from phase 3 as a bar graph. The stabilised response from the experimental data for black sheets was plotted as a bar graph. The configuration and distance variations are displayed on the x axis as the following labels:

- U900 – TEG as a unit, set 900 mm from the heat source.
- U600 – TEG as a unit, set 600 mm from the heat source.
- U300 – TEG as a unit, set 300 mm from the heat source.
- P900 – 2 TEGs connected in parallel at 900 mm from the heat source.
- P600 – 2 TEGs connected in parallel at 600 mm from the heat source.
- P300 – 2 TEGs are connected in parallel at 300 mm from the heat source.
- S900 – 2 TEGs are connected in series at 900 mm from the heat source.
- S600 – 2 TEGs are connected in series at 600 mm from the heat source.
- S300 – 2 TEGs are connected in series at 300 mm from the heat source.

The dual y-axes display the corresponding P_{max} values of the blue bars on the left-hand side y axis and the corresponding ΔT values of the orange bars on the right-hand side y axis. P_{max} and ΔT is measured in microwatts (μW) and degrees Celsius ($^{\circ}C$) respectively.

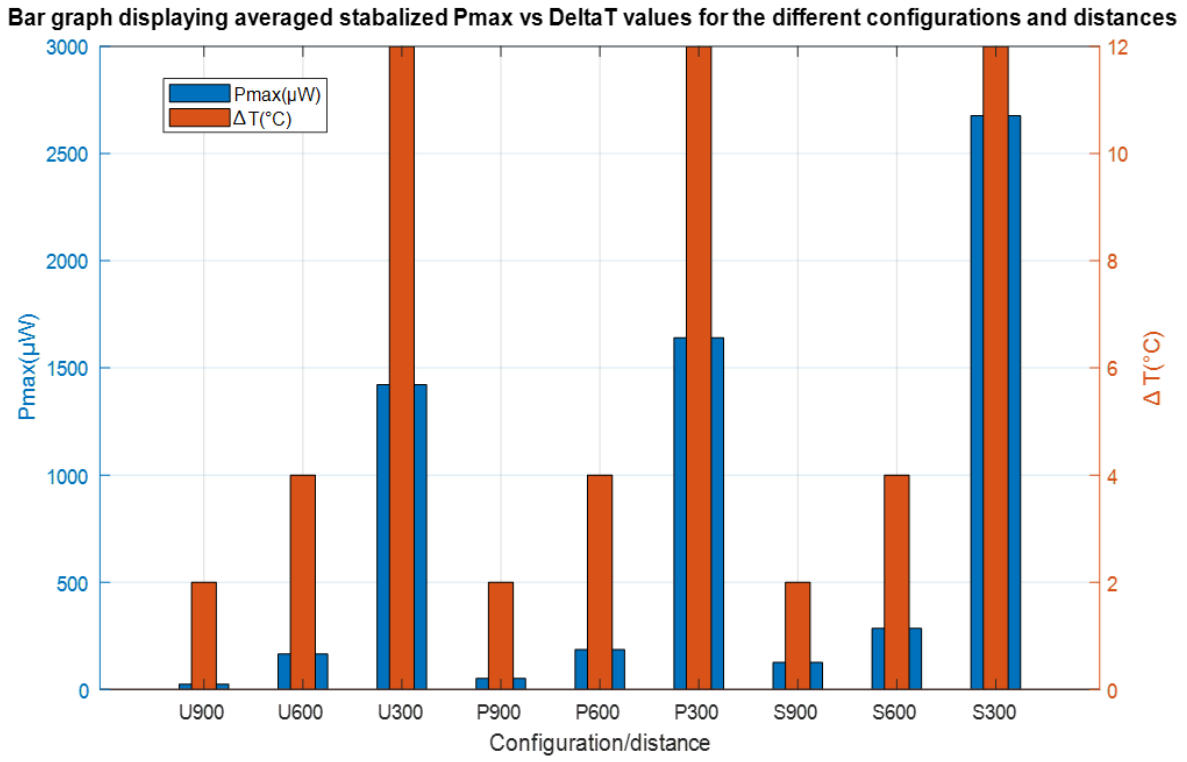

Figure 4.3: Bar graph displaying averaged results once readings were stabilised, for the different configurations and distances for black sheets

The data acquired from phase 3 which was illustrated graphically as a bar graph in Figure 4.3, was then plotted as points on axes in Figure 4.4. In Figure 4.4, P_{max} on the y axis and ΔT on the x axis is measured in microwatts (μW) and degrees Celsius ($°C$), respectively. The data acquired from the unit, parallel and series electrical configuration is indicated by red dots, green crosses, and blue squares, respectively.

Steps 1-4 of the IV Curve generation method were carried out during the experiments, and the resultant pairs of data were used to calculate the P_{max} generated. The raw measured data is voluminous and is therefore, not provided in the work. Sample calculations for P_{max} are provided below and is calculated using Equation 2.1, where I_s was measured in mA and V_o was measured in mV:

P_{max} calculated for a black unit TEM when placed 300mm from the heat source:

$$P_{max} = \frac{1}{4} I_s \times V_o$$

$$= \frac{1}{4} 31.25 \times 189.95$$

$$= 1483.86\ \mu W$$

P_{max} calculated for 2 black TEMs connected in parallel and placed 300mm from the heat source:

$$P_{max} = \frac{1}{4} I_s \times V_o$$

$$= \frac{1}{4} 37.65 \times 174.85$$

$$= 1645.77\ \mu W$$

P_{max} calculated for 2 black TEMs connected in series and placed 300mm from the heat source:

$$P_{max} = \frac{1}{4} I_s \times V_o$$

$$= \frac{1}{4} 33.4 \times 0.3293$$

$$= 2749.66\ \mu W$$

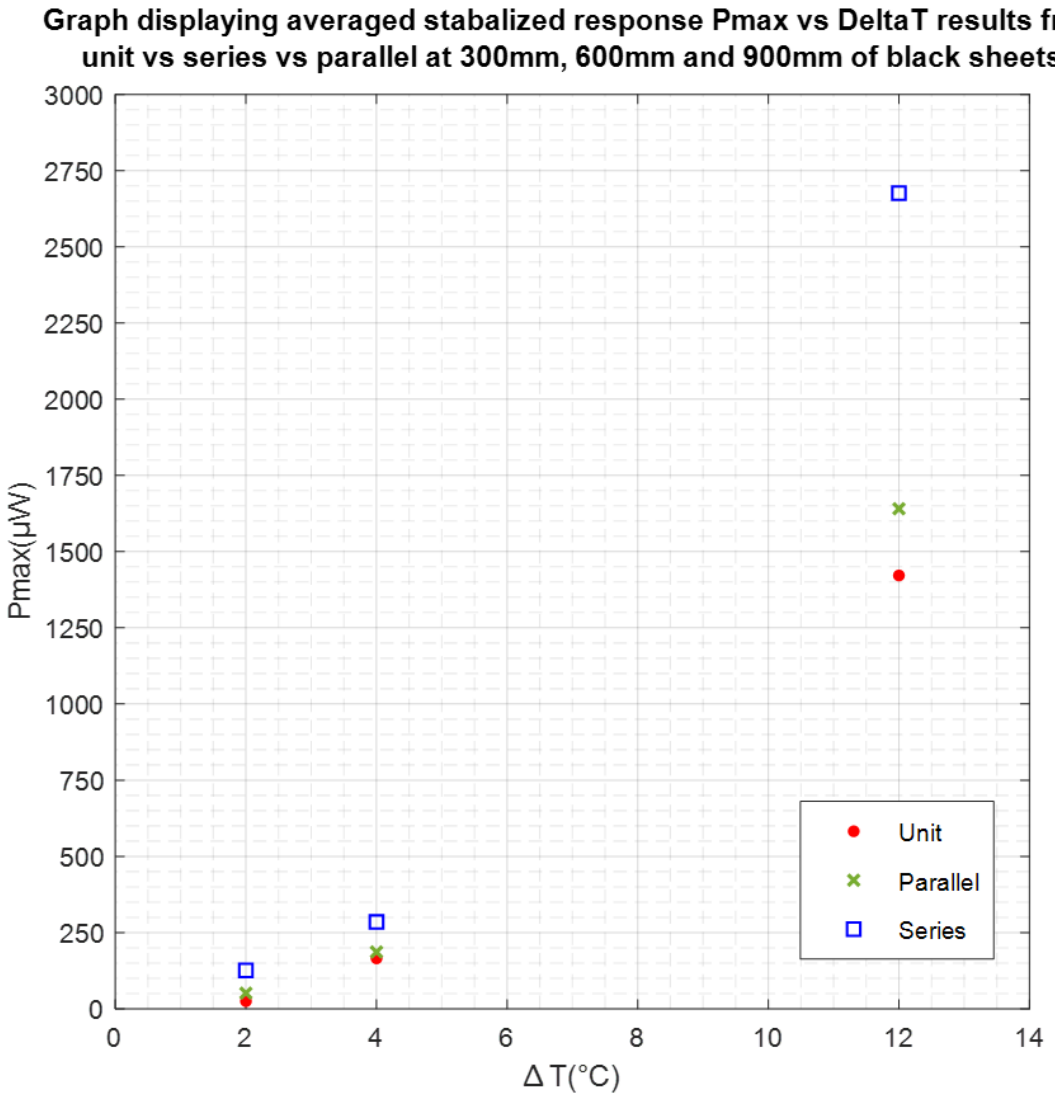

Figure 4.4: Plot displaying averaged results once readings were stabilised, for the different configurations, colours, and distances.

4.3.1.2 Findings

If Figure 4.3 and Figure 4.4 are cross checked, it is evident that the TEG in series configuration generated the highest P_{max} when located 300 mm from the heat source, followed by 600 mm and lastly, 900 mm. The same pattern was found for the unit and parallel configurations. This ties up with the findings, mentioned in Section 2 that Lashin, et al. [64] established i.e., the highest intensity of heat will generate the highest power output.

The data shows that the TEG system, when placed 900 mm from the heat source, experienced a ΔT of 2 $°C$. This was doubled at 600 mm and increased 6-fold when positioned at 300 mm.

Similarly, when placed at 900 mm from the heat source, the TEG system as a unit configuration, generated a P_{max} of 24.89 μW. This was doubled when connected in parallel and increased 5-fold when in a series arrangement.

When the TEG system was placed at 600 mm, a P_{max} of 165.23 μW was generated by the unit configuration. This increased by a factor of 1.12 when connected in a parallel arrangement and by a factor of 1,72 when connected in series arrangement.

For the 300 mm placement, the TEG system generated a P_{max} of 1421.74 μW as a unit. This increased by a factor of 1.15 when connected in parallel and by a factor of 1.88 times when connected in series arrangement.

The above analysis of phase 3 data acquisition is summarised and presented in Table 4.1. The distance is varied and the resultant output parameter's factor of increase, under different electrical configurations are tabulated. While the power output per TEG tile is small in magnitude, the proposed configuration lends itself to the coupling of multiple units to increase power output. The current work shows potential for the use of TEGs in this application. Through further investigation, refinement and cost analysis, the system may prove to be a practical method of solar energy harvesting.

Table 4.1: Tabulated analysis of results acquired from phase 3 of experiments.

Distance(mm)	Parameter	Electrical connection	Factor of increase
900	ΔT	Unit, parallel and series.	0
600			2
300			6
900	P_{max}	Unit	0
		Parallel	2
		Series	5
600	P_{max}	Unit	0
		Parallel	1.12
		Series	1.72
300	P_{max}	Unit	0
		Parallel	1.15
		Series	1.88

4.3.2 Scalability of TEGs for maximum power output.

The presented solar data show that an 80 mm×80 mm black square IBR sheeting in the TEG unit, developed an average ΔT of 1.35 $°C$. The indoor experiment data which developed a ΔT closest to the solar experiment, was an average of 2$°C$, when the lamp was situated 900 mm away from the black coated TEG. The resultant average V_{oc} was 26.96 mV, I_s was 4.24 mA and P_{max} was 29.24 µW. Therefore, the average P_{max} expected from solar applications on a cool day, by the black TEG as a unit, is 29.24 µW. This amounts to 4.57 nW/mm^2.

Data acquired from phase 3 show that, under an average ΔT of 2$°C$, 2 TEGs of 80 mm×80 mm square IBR sheeting each, which were electrically connected in series, generated a P_{max} of 125.71 µW. When 2 TEGs of 80 mm×80 mm square IBR sheeting were connected in parallel, a P_{max} of 51.29 µW was generated. Based on the result from phase 2, it is evident that connecting TEGs in series generates maximum power output. Electrically connecting the TEGs vertically, allows for the aluminium bars to serve as an electrical conductor as well to connect one TEM to another, thus completing the TEG system. This configuration allows for ease of assembly. The vertical assembly may be placed side by side with more vertical assemblies, to enhance the power output due to larger surface areas. Figure 4.5 presents in this configuration in the form of a CAD drawing.

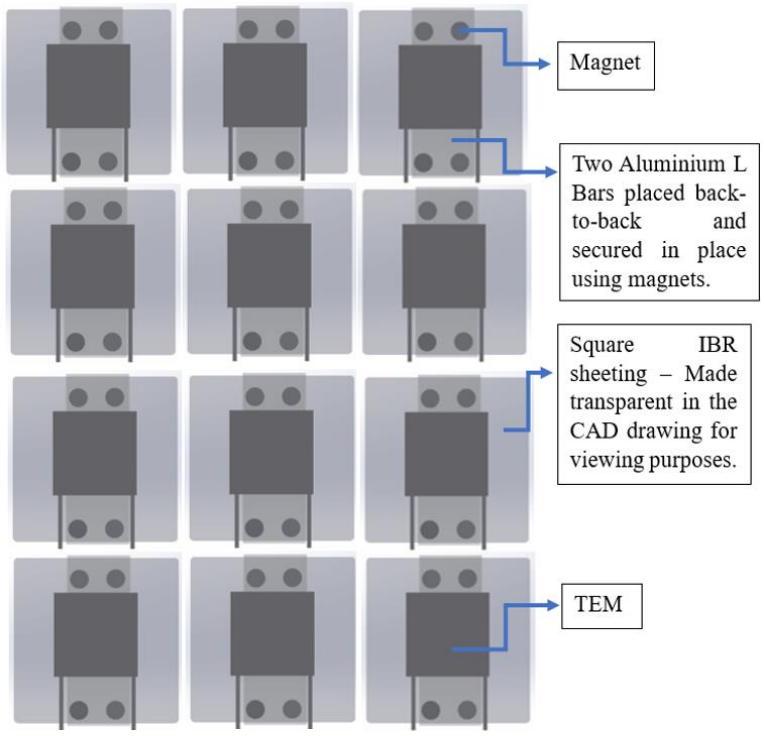

Figure 4.5: CAD assembly of TEG system for scalability.

As mentioned earlier, the highest P_{max} generated by a unit TEM, from the experiments conducted in this work, was found to be 1421.74 µW. This P_{max} was established by the 40 mm ×40 mm TEM in the TEG system. For normalising purposes, it may be predicted that on a surface area of one square metre, a resultant 625 TEMs as units are required and may generate a P_{max} of 0.89W/m^2. This is a theoretical extrapolation based on the experimental results achieved from this research, since the research conducted is a preliminary study in the investigation of power output of TEGs. The TEG system may generate 0.89W/m^2 on black coated IBR sheeting. Furthermore, it is acknowledged that the power output is low and may not be economical, currently. Some applications for this TEG system may be to power low power wearables, power storage in batteries for later use, or low power lighting applications. Therefore, the scaling of TEGs electrically connected in series, merits further investigation.

TEG devices may improve in efficiency through future technological advancements which may result in improved power output generation. The scalability option provides potential in generating larger amount of energy on large surface areas. Therefore, the results show that the TEG system may show potential for use in warehouses, when the warehouse sheeting is painted matte black.

5 Conclusion and Recommendations

5.1 Conclusion

The focus of the presented preliminary study was to investigate whether TEGs are a potential means for solar energy harvesting. A modular prototype was configured, relevant tests were run, and the performance characteristics obtained from experiments were discussed.

The TEG was tested in the vertical position to allow for natural convection, and devoid of most other thermal variables and hence may not reflect results that would be obtained in real application. The TEG prototype was exposed to the light source at different distances, perpendicular to the sheets. The study investigated the effect that the 2 variables have on the amount of solar power harvested i.e., the colour of metal IBR sheeting, and the ideal electrical arrangement for scalability of Peltier tiles for maximum power output.

The primary outcome is that the black coated sheets of TEG1 outperformed all other colours. It can, therefore, be concluded that when this TEG system is applied to the warehouse side sheeting and wall cladding, an optimum output may be established by coating the roof sheeting with a matte black paint. The output ΔT from solar experiments was found to be of a consistent range, therefore, it was deduced that the aluminium L-bars perform well as heat sinks and fulfilled its purpose of regulating ΔT. It was also concluded that the TEGs in series configuration, generated the highest P_{max} when located closest to the light source.

For normalising purposes, it was predicted, that on a surface area of one square metre, a resultant 625 TEMs as units are required and may generate a P_{max} of 0.89W/m^2. This is a theoretical extrapolation based on the experimental results achieved from this research, since the research conducted is a preliminary study in the investigation of power output of TEGs. The TEG system may generate 0.89W/m^2 on black coated IBR sheeting. It is acknowledged that the power output is low and some applications may be to power low power wearables, power storage in batteries for later use, or low power lighting applications. Hence, it may be concluded from the proposed TEG system that TEGs could be a reasonable method for harvesting solar energy on IBR sheeting, specifically in a vertical position.

The results merit further investigation and refinement into the use of TEGs on IBR sheeting where the herein TEG system may be set-up in a user friendly, simple, cost effective and practical manner for solar energy harvesting.

5.2 Recommendations

Applications of different orientations and geographical locations require further investigation.

The proposed TEG is tested in the vertical position to allow for natural convection, devoid of most thermal variables and hence would not reflect results that would be obtained in real application. The device was tested in the most efficient manner with respect to natural convection for cooling purposes. Therefore, when the presented TEG system is tested for real-world applications, thermal factors, geographical location, incline, tilt, sun-tracking, and orientations should be investigated. Further development is required for application specific TEG systems.

A dull matte black paint should be used to coat the IBR sheeting.

During the research, it was found that some spray cans are labelled as ‘matte black’ but were found to be slightly glossy or reflective when used. The matte black coated sheets are expected to absorb the most amount of radiation and thus achieving the highest temperature. The sheets would not heat up as fast if the black coat is slightly reflective [14][15]. It is recommended that this should be checked beforehand and avoided. In doing so, any reflection of radiation heat may be prevented. Thus, increasing the efficiency of the TEG system.

References

[1] Flanagan Logistics Wahrehouse Space. "What is a warehouse made of?" (accessed 3rd March, 2022).

[2] Anneliese O'Malley. "Warehouse construction: the differences and similarities." (accessed 3rd March, 2022).

[3] Roof Source (Pty) Ltd. "Roof Sheeting." https://www.roofsource.co.za/roof-metal-sheeting/ (accessed 26th September, 2022).

[4] Cousins Steel International. "686-IBR Profile." https://cousinssteel.co.za/686-ibr-profile/ (accessed 26th September, 2022).

[5] M. S. Mlasi, "A Parametric Study on IBR Sheeting Supported by Purlins," University of the Witwatersrand, Faculty of Engineering and the Built …, 2016.

[6] BYJU's. "Heat transfer." https://byjus.com/physics/heat-transfer-conduction-convection-and-radiation/ (accessed 25 January 2022).

[7] Siyavula. "Heating as a transfer of Energy." (accessed 10th March, 2022).

[8] savemyexams. "Convection." (accessed 10th March, 2022).

[9] M. Fahiminia, M. M. Naserian, H. Goshayeshi, and D. Majidian, "Investigation of Natural Convection Heat Transfer Coefficient on Extended Vertical Base Plates," *Energy and Power Engineering*, vol. 03, 01/01 2011, doi: 10.4236/epe.2011.32022.

[10] A. Molina, M. Falvey, and R. Rondanelli, "A solar radiation database for Chile," *Scientific reports*, vol. 7, no. 1, pp. 1-11, 2017.

[11] ResearchGate. "Representation of solar radiation components." (accessed 10th March, 2022).

[12] Alternative Energy Tutorials. "Solar Irradiance." https://www.alternative-energy-tutorials.com/solar-power/solar-irradiance.html (accessed 5th April, 2022).

[13] Chris Deziel. "Which colors reflect more light?" Sciencing. (accessed 3rd March, 2022).

[14] S. Ehsan and M. Kianmehr, "Effect of black surfaces to increase the average surface temperature of the earth: A global warning!," *Caspian Journal of Environmental Sciences*, vol. 11, no. 1, pp. 19-27, 2013.

[15] J. Paminto, F. Fianti, and I. Yulianti, "The Effect of Surface Color on the Absorption of Solar Radiation," *Physics Communication*, vol. 5, no. 1, pp. 27-32, 2021.

[16] Electronic Clinic. "Heat Sink, Types of Heat Sink and Design of Heat Sink." https://www.electroniclinic.com/heat-sink-types-of-heat-sink-and-design-of-heat-sink/ (accessed 18th October, 2022).

[17] Metal Supermarkets. "Which Metals Conduct Heat Best." https://www.metalsupermarkets.com/which-metals-conduct-heat-best/ (accessed 18th September, 2022).

[18] Arrow Electronics. "Understanding Heat Sinks: Functions, Types, & More." https://www.arrow.com/en/research-and-events/articles/understanding-heat-sinks-functions-types-and-more (accessed 18th September, 2022).

[19] Kapil Kumar, "How to Select a Heat Sink," in *Heat Sink, Thermal Management* vol. 2022, ed, 2022.

[20] P. Fernández-Yáñez, V. Romero, O. Armas, and G. Cerretti, "Thermal management of thermoelectric generators for waste energy recovery," *Applied Thermal Engineering*, vol. 196, p. 117291, 2021/09/01/ 2021, doi: https://doi.org/10.1016/j.applthermaleng.2021.117291.

[21] L. Hewawasam, A. Jayasena, M. Afnan, R. Ranasinghe, and M. Wijewardane, "Waste heat recovery from thermo-electric generators (TEGs)," *Energy Reports*, vol. 6, pp. 474-479, 2020.

[22] Q. Cao, W. Luan, and T. Wang, "Performance enhancement of heat pipes assisted thermoelectric generator for automobile exhaust heat recovery," *Applied Thermal Engineering*, vol. 130, pp. 1472-1479, 2018.

[23] N. Jaziri, A. Boughamoura, J. Müller, B. Mezghani, F. Tounsi, and M. Ismail, "A comprehensive review of Thermoelectric Generators: Technologies and common applications," *Energy Reports*, vol. 6, pp. 264-287, 2020.

[24] K. Sztekler, K. Wojciechowski, and M. Komorowski, "The thermoelectric generators use for waste heat utilization from conventional power plant," *E3S Web of Conferences*, vol. 14, p. 01032, 01/01 2017, doi: 10.1051/e3sconf/20171401032.

[25] L. Lira, "Why do some prices in the retail sector drop when demand rises?," 2006.

[26] B. Padilla, "Temperature sensing with thermistors," *Texas Instruments: Dallas, TX, USA*, 2020.

[27] microdigisoft.com. "Temperature Sensor and Types." https://microdigisoft.com/temperature-sensor-and-types/ (accessed 10th October 2022).

[28] M. Javaid, A. Haleem, R. P. Singh, S. Rab, and R. Suman, "Significance of sensors for industry 4.0: Roles, capabilities, and applications," *Sensors International*, vol. 2, p. 100110, 2021.

[29] Blaze technical inc., " Types of Temperature Sensors." https://blazeprobes.com/temperature-sensors-2/ (accessed 15th February 2024).

[30] J. Gums, "Types of Temperature Sensors," vol. 2022, ed: Digi-Key Electronics, 2018.

[31] A. Feteira, "Negative temperature coefficient resistance (NTCR) ceramic thermistors: an industrial perspective," *Journal of the American Ceramic Society*, vol. 92, no. 5, pp. 967-983, 2009.

[32] B. A. Kuzubasoglu and S. K. Bahadir, "Flexible temperature sensors: A review," *Sensors and Actuators A: Physical*, vol. 315, p. 112282, 2020.

[33] D. Tutunea, G. Gherghina, I. Dumitru, and A. Dima, "Evaluation of thermistors used for temperature measurement in automotive industry," in *Applied Mechanics and Materials*, 2018, vol. 880: Trans Tech Publ, pp. 157-162.

[34] Ametherm, "4 Most Common Types of Temperature Sensors," vol. 2022, ed.

[35] Elprocus. "Temperature Sensors - Types, Working and Operation." https://www.elprocus.com/temperature-sensors-types-working-operation/ (accessed 23rd October, 2022).

[36] Industrial Quick Search. "Temperature Sensors." https://www.iqsdirectory.com/articles/thermocouple/temperature-sensors.html (accessed 23rd October, 2022).

[37] F. C. Padoan, P. Altimari, and F. Pagnanelli, "Recycling of end of life photovoltaic panels: A chemical prospective on process development," *Solar Energy*, vol. 177, pp. 746-761, 2019.

[38] S. Mekhilef, R. Saidur, and A. Safari, "A review on solar energy use in industries," *Renewable and sustainable energy reviews*, vol. 15, no. 4, pp. 1777-1790, 2011.

[39] M. A. Green, "Photovoltaics: technology overview," *Energy policy*, vol. 28, no. 14, pp. 989-998, 2000.

[40] Z. A. Haidar, J. Orfi, and Z. Kaneesamkandi, "Experimental investigation of evaporative cooling for enhancing photovoltaic panels efficiency," *Results in Physics*, vol. 11, pp. 690-697, 2018.

[41] J. R. Balfour and M. Shaw, *Introduction to photovoltaic system design*. Jones & Bartlett Publishers, 2011.

[42] M. Mani and R. Pillai, "Impact of dust on solar photovoltaic (PV) performance: Research status, challenges and recommendations," *Renewable and sustainable energy reviews*, vol. 14, no. 9, pp. 3124-3131, 2010.

[43] Building DC Energy Systems, "Solar Panel," 2021. [Online]. Available: https://learn.libre.solar/system/solar_panel.html#photovoltaic-cells.

[44] Paul Wormser. "Can your solar project weather a hailstorm? ." https://www.solarpowerworldonline.com/2020/12/can-your-solar-project-weather-a-hailstorm/ (accessed 21st April, 2022).

[45] Solar Panel Cleaning. "Why clean solar panels?" https://www.solarpanelcleaningltd.co.uk/why-clean-solar-panels/dirty-v-clean-panel-pic-2-2/ (accessed 21st April, 2022).

[46] J. Papiewski. "The effect of wavelengths on Photovoltaic cells." https://education.seattlepi.com/effect-wavelength-photovoltaic-cells-3353.html (accessed.

[47] Brilliant. "Spectral properties - Solar Energy." https://brilliant.org/practice/spectral-properties-sunlight/ (accessed 28th September, 2022).

[48] Y. Zhao, M. Lu, Y. Li, M. Ge, L. Xie, and L. Liu, "Characteristics analysis of an exhaust thermoelectric generator system with heat transfer fluid circulation," *Applied Energy*, vol. 304, p. 117896, 2021/12/15/ 2021, doi: https://doi.org/10.1016/j.apenergy.2021.117896.

[49] J. Yang and F. R. Stabler, "Automotive applications of thermoelectric materials," *Journal of electronic materials*, vol. 38, no. 7, p. 1245, 2009.

[50] A. Marvão, P. J. Coelho, and H. C. Rodrigues, "Optimization of a thermoelectric generator for heavy-duty vehicles," *Energy Conversion and Management*, vol. 179, pp. 178-191, 2019.

[51] E. Thacher, B. Helenbrook, M. Karri, and C. J. Richter, "Testing of an automobile exhaust thermoelectric generator in a light truck," *Proceedings of the Institution of Mechanical Engineers, Part D: Journal of Automobile Engineering*, vol. 221, no. 1, pp. 95-107, 2007.

[52] X. Liu, Y. Deng, Z. Li, and C. Su, "Performance analysis of a waste heat recovery thermoelectric generation system for automotive application," *Energy conversion and management*, vol. 90, pp. 121-127, 2015.

[53] J. Chen, R. Wang, D. Luo, and W. Zhou, "Performance optimization of a segmented converging thermoelectric generator for waste heat recovery," *Applied Thermal Engineering*, vol. 202, p. 117843, 2022.

[54] A. S. Kushch, J. C. Bass, S. Ghamaty, and N. Eisner, "Thermoelectric development at Hi-Z technology," in *Proceedings ICT2001. 20 International Conference on Thermoelectrics (Cat. No. 01TH8589)*, 2001: IEEE, pp. 422-430.

[55] K. McEnaney, D. Kraemer, Z. Ren, and G. Chen, "Modeling of concentrating solar thermoelectric generators," *Journal of applied physics,* vol. 110, no. 7, p. 074502, 2011.

[56] X. Wang *et al.*, "High-performance flat-panel solar thermoelectric generators with high thermal concentration," 2011.

[57] S. Lv *et al.*, "High-performance terrestrial solar thermoelectric generators without optical concentration for residential and commercial rooftops," *Energy conversion and management,* vol. 196, pp. 69-76, 2019.

[58] P. Sundarraj, D. Maity, S. S. Roy, and R. A. Taylor, "Recent advances in thermoelectric materials and solar thermoelectric generators–a critical review," *RSC Advances,* vol. 4, no. 87, pp. 46860-46874, 2014.

[59] D. Sun, L. Shen, Y. Yao, H. Chen, S. Jin, and H. He, "The real-time study of solar thermoelectric generator," *Applied Thermal Engineering,* vol. 119, pp. 347-359, 2017/06/05/ 2017, doi: https://doi.org/10.1016/j.applthermaleng.2017.03.075.

[60] M. Telkes, "Solar thermoelectric generators," *Journal of Applied Physics,* vol. 25, no. 6, pp. 765-777, 1954.

[61] D. Kraemer *et al.*, "Concentrating solar thermoelectric generators with a peak efficiency of 7.4%," *Nature Energy,* vol. 1, no. 11, pp. 1-8, 2016.

[62] C. A. Mgbemene, H. O. Njoku, and C. O. A. Agbo, "Investigation of parametric performance of the hybrid 3D CPC/TEM system due to thermoelectric irreversibilities," *Frontiers in Energy Research,* p. 101, 2018.

[63] C. Tzivanidis, E. Bellos, D. Korres, K. Antonopoulos, and G. Mitsopoulos, "Thermal and optical efficiency investigation of a parabolic trough collector," *Case Studies in Thermal Engineering,* vol. 6, pp. 226-237, 2015.

[64] A. Lashin, M. Al Turkestani, and M. Sabry, "Performance of a Thermoelectric Generator Partially Illuminated with Highly Concentrated Light," *Energies,* vol. 13, no. 14, p. 3627, 2020.

[65] A. Kumar and S. Shukla, "Mathematical modeling and optimization of a parabolic trough concentrator for the improvement of collection efficiency," *Int. J. Innov. Res. Eng. Manage,* vol. 3, pp. 375-380, 2016.

[66] A.-N. Moh'd A, B. M. Tashtoush, M. A. Khasawneh, and I. Al-Keyyam, "A hybrid concentrated solar thermal collector/thermo-electric generation system," *Energy,* vol. 134, pp. 1001-1012, 2017.

[67] Y. Jeyashree, Y. Sukhi, A. V. Juliet, S. L. Jame, and S. Indirani, "Concentrated solar thermal energy harvesting using Bi2Te3based thermoelectric generator," *Materials Science in Semiconductor Processing*, vol. 107, p. 104782, 2020.

[68] C. Lertsatitthanakorn, J. Jamradloedluk, and M. Rungsiyopas, "Electricity generation from a solar parabolic concentrator coupled to a thermoelectric module," *Energy procedia*, vol. 52, pp. 150-158, 2014.

[69] M. Eswaramoorthy and S. Shanmugam, "Solar parabolic dish thermoelectric generator: a technical study," *Energy Sources, Part A: Recovery, Utilization, and Environmental Effects*, vol. 35, no. 5, pp. 487-494, 2013.

[70] P. Cheruvu, V. P. Kumar, and H. C. Barshilia, "Experimental analysis and evaluation of a vacuum enclosed concentrated solar thermoelectric generator coupled with a spectrally selective absorber coating," *International Journal of Sustainable Energy*, vol. 37, no. 8, pp. 782-798, 2018.

[71] R. Amatya and R. Ram, "Solar thermoelectric generator for micropower applications," *Journal of electronic materials*, vol. 39, no. 9, pp. 1735-1740, 2010.

[72] M. Zhang *et al.*, "Efficient, low-cost solar thermoelectric cogenerators comprising evacuated tubular solar collectors and thermoelectric modules," *Applied energy*, vol. 109, pp. 51-59, 2013.

[73] G. Contento, B. Lorenzi, A. Rizzo, and D. Narducci, "Simultaneous materials and layout optimization of non-imaging optically concentrated solar thermoelectric generators," *Energy*, vol. 194, p. 116867, 2020.

[74] A. Imenes and D. Mills, "Spectral beam splitting technology for increased conversion efficiency in solar concentrating systems: a review," *Solar energy materials and solar cells*, vol. 84, no. 1-4, pp. 19-69, 2004.

[75] A. Z. Sahin, K. G. Ismaila, B. S. Yilbas, and A. Al-Sharafi, "A review on the performance of photovoltaic/thermoelectric hybrid generators," *International Journal of Energy Research*, vol. 44, no. 5, pp. 3365-3394, 2020.

[76] P. Huen and W. A. Daoud, "Advances in hybrid solar photovoltaic and thermoelectric generators," *Renewable and Sustainable Energy Reviews*, vol. 72, pp. 1295-1302, 2017.

[77] G. Li, S. Shittu, T. M. Diallo, M. Yu, X. Zhao, and J. Ji, "A review of solar photovoltaic-thermoelectric hybrid system for electricity generation," *Energy*, vol. 158, pp. 41-58, 2018.

[78] M. Muzdakis. "Researchers developed a panel that continies to generae energy once the sun sets." https://mymodernmet.com/night-solar-panel/ (accessed 2nd June 2022).

[79] X. Ju, Z. Wang, G. Flamant, P. Li, and W. Zhao, "Numerical analysis and optimization of a spectrum splitting concentration photovoltaic–thermoelectric hybrid system," *Solar energy,* vol. 86, no. 6, pp. 1941-1954, 2012.

[80] W. Zhu, Y. Deng, Y. Wang, S. Shen, and R. Gulfam, "High-performance photovoltaic-thermoelectric hybrid power generation system with optimized thermal management," *Energy,* vol. 100, pp. 91-101, 2016.

[81] M. Mohsenzadeh and M. Shafii, "A novel concentrating photovoltaic/thermal solar system combined with thermoelectric module in an integrated design," *Renewable Energy,* vol. 113, pp. 822-834, 2017.

[82] T. Cui, Y. Xuan, E. Yin, Q. Li, and D. Li, "Experimental investigation on potential of a concentrated photovoltaic-thermoelectric system with phase change materials," *Energy,* vol. 122, pp. 94-102, 2017.

[83] R. McCarty and R. Piper, "Voltage–current curves to characterize thermoelectric generators," *Journal of electronic Materials,* vol. 44, no. 6, pp. 1896-1901, 2015.

[84] H. Shen, H. Lee, and S. Han, "Optimization and fabrication of a planar thermoelectric generator for a high-performance solar thermoelectric generator," *Current Applied Physics,* vol. 22, pp. 6-13, 2021.

[85] Z. M. Dalala, O. Saadeh, M. Bdour, and Z. U. Zahid, "A new maximum power point tracking (MPPT) algorithm for thermoelectric generators with reduced voltage sensors count control," *Energies,* vol. 11, no. 7, p. 1826, 2018.

[86] H. Mamur and Y. Coban, "Detailed modeling of a thermoelectric generator for maximum power point tracking," *Turkish Journal of Electrical Engineering and Computer Sciences,* vol. 28, no. 1, pp. 124-139, 2020.

[87] B. Bijukumar, A. K. Raam, S. I. Ganesan, and C. Nagamani, "A linear extrapolation-based MPPT algorithm for thermoelectric generators under dynamically varying temperature conditions," *IEEE Transactions on Energy Conversion,* vol. 33, no. 4, pp. 1641-1649, 2018.

[88] A. Montecucco, J. Siviter, and A. R. Knox, "The effect of temperature mismatch on thermoelectric generators electrically connected in series and parallel," *Applied Energy,* vol. 123, pp. 47-54, 2014.

[89] F. M. Siddiqui and V. Maurya, "Study of TEG When Connected in Series and Parallel Combinations Along With a DC-DC Converter," *Vivechan International Journal of Research,* vol. 8, no. 1, pp. 76-86, 2017.

[90] W.-H. Chen, C.-Y. Liao, C.-I. Hung, and W.-L. Huang, "Experimental study on thermoelectric modules for power generation at various operating conditions," *Energy,* vol. 45, no. 1, pp. 874-881, 2012.

[91] F. Morais *et al.*, "Optimization of the TEGs Configuration (Series/Parallel) in Energy Harvesting Systems with Low-Voltage Thermoelectric Generators Connected to Ultra-Low Voltage DC–DC Converters," *Energies,* vol. 13, no. 9, p. 2297, 2020.

[92] M. R. A. BHUİYAN, H. MAMUR, M. A. ÜSTÜNER, and Ö. F. DİLMAÇ, "Current and Future Trend Opportunities of Thermoelectric Generator Applications in Waste Heat Recovery," *Gazi University Journal of Science,* pp. 1-1, 2021.

[93] M. Araiz, A. Martínez, D. Astrain, and P. Aranguren, "Experimental and computational study on thermoelectric generators using thermosyphons with phase change as heat exchangers," *Energy Conversion and Management,* vol. 137, pp. 155-164, 2017.

[94] P. Aranguren, M. Araiz, D. Astrain, and A. Martínez, "Thermoelectric generators for waste heat harvesting: A computational and experimental approach," *Energy Conversion and Management,* vol. 148, pp. 680-691, 2017.

[95] M. Araiz, Á. Casi, L. Catalán, Á. Martínez, and D. Astrain, "Prospects of waste-heat recovery from a real industry using thermoelectric generators: Economic and power output analysis," *Energy Conversion and Management,* vol. 205, p. 112376, 2020.

[96] D. Dai, Y. Zhou, and J. Liu, "Liquid metal based thermoelectric generation system for waste heat recovery," *Renewable Energy,* vol. 36, no. 12, pp. 3530-3536, 2011.

[97] D. Ebling *et al.*, "Development of a system for thermoelectric heat recovery from stationary industrial processes," *Journal of Electronic Materials,* vol. 45, no. 7, pp. 3433-3439, 2016.

[98] P. M. Kumar *et al.*, "The design of a thermoelectric generator and its medical applications," *Designs,* vol. 3, no. 2, p. 22, 2019.

[99] D. Bhatia, S. Bairagi, S. Goel, and M. Jangra, "Pacemakers charging using body energy," *Journal of Pharmacy And Bioallied Sciences,* vol. 2, no. 1, p. 51, 2010.

[100] V. Leonov, T. Torfs, R. J. Vullers, and C. Van Hoof, "Hybrid thermoelectric–photovoltaic generators in wireless electroencephalography diadem and electrocardiography shirt," *Journal of electronic materials,* vol. 39, no. 9, pp. 1674-1680, 2010.

[101] C. S. Kim *et al.*, "Self-powered wearable electrocardiography using a wearable thermoelectric power generator," *ACS Energy Letters,* vol. 3, no. 3, pp. 501-507, 2018.

[102] D. Shwetha and M. Suma, "A Conceptual View to Empower Medical Gadgets by Harvesting Energy using TEG," *International Journal for Advance Research and Development*, vol. 2, no. 6, pp. 124-130, 2017.

[103] V. Bhatnagar and P. Owende, "Energy harvesting for assistive and mobile applications," *Energy Science & Engineering*, vol. 3, no. 3, pp. 153-173, 2015.

[104] A. Proto *et al.*, "Human Body Energy Harvesting Solutions for Wearable Technologies," in *2018 IEEE 20th International Conference on e-Health Networking, Applications and Services (Healthcom)*, 2018: IEEE, pp. 1-5.

[105] V. Leonov, T. Torfs, P. Fiorini, and C. Van Hoof, "Thermoelectric converters of human warmth for self-powered wireless sensor nodes," *IEEE Sensors Journal*, vol. 7, no. 5, pp. 650-657, 2007.

[106] K. T. Settaluri, H. Lo, and R. J. Ram, "Thin thermoelectric generator system for body energy harvesting," *Journal of electronic materials*, vol. 41, no. 6, pp. 984-988, 2012.

[107] M. Wahbah, M. Alhawari, B. Mohammad, H. Saleh, and M. Ismail, "Characterization of human body-based thermal and vibration energy harvesting for wearable devices," *IEEE Journal on emerging and selected topics in circuits and systems*, vol. 4, no. 3, pp. 354-363, 2014.

[108] A. Proto *et al.*, "Thermal energy harvesting on the bodily surfaces of arms and legs through a wearable thermo-electric generator," *Sensors*, vol. 18, no. 6, p. 1927, 2018.

[109] V. Leonov, "Thermoelectric energy harvesting of human body heat for wearable sensors," *IEEE Sensors Journal*, vol. 13, no. 6, pp. 2284-2291, 2013.

[110] I. Radian Thermal Products. "Aluminium heatsink." https://www.radianheatsinks.com/aluminum-heatsink/ (accessed 22nd September, 2022).

[111] Mantech. *Mantech Electronics*. (2022). Accessed: 31st October 2022. [Online]. Available: https://www.mantech.co.za/ProductInfo.aspx?Item=83M0125-A

[112] Arduino. "What is Arduino?" https://www.arduino.cc/en/Guide/Introduction (accessed 16th September, 2022).

[113] Arduino.cc. "Liquid Crystal Displays(LCD) with Arduino." https://docs.arduino.cc/learn/electronics/lcd-displays (accessed 15th November, 2022).

Appendices

Appendix A – Performance characteristics of TEM used in experiments

THERMOELECTRIC POWER GENERATION MODULES

200°C TEG (Tested at Hot Side Temperature: 200°C, Cold Side Temperature: 50°C)											
RS Part No.	MPN	Couples	V_{oc} (V)	R_{in} (Ω)	I_{max} (A)	P_{max} (W)	T_{max} (°C)	W (mm)	L (mm)	H (mm)	See Chart
6937028	GM200-127-10-15	127	7.00	7.70	1.60	1.60	200	30	30	3.7	1
6937030	GM200-71-14-16	71	3.90	2.10	1.80	1.80	200	30	30	3.8	2
6937043	GM200-127-14-16	127	7.00	4.00	3.10	3.10	200	40	40	3.8	3
6937040	GM200-31-28-35	31	1.70	0.56	1.30	1.30	200	30	30	6.3	4
6937059	GM200-127-28-35	127	7.00	2.30	5.30	5.30	200	62	62	6.3	5
6937056	GM200-49-45-30	49	2.50	0.28	5.60	5.60	200	62	62	5.8	6
6937068	GM200-49-45-25	49	2.50	0.23	6.80	6.80	200	62	62	5.3	7

250°C TEG (Tested at Hot Side Temperature: 250°C, Cold Side Temperature: 50°C)											
RS Part No.	MPN	Couples	V_{oc} (V)	R_{in} (Ω)	I_{max} (A)	P_{max} (W)	T_{max} (°C)	W (mm)	L (mm)	H (mm)	See Chart
6937071	GM250-127-10-15	127	9.40	7.90	0.59	2.80	250	30	30	3.7	1
6937078	GM250-71-14-16	71	5.30	2.40	1.10	2.90	250	30	30	3.8	2
6937080	GM250-127-14-16	127	9.40	4.30	1.09	5.10	250	40	40	3.8	3
6937093	GM250-31-28-35	31	2.30	0.59	1.95	2.20	250	30	30	6.3	4
6937090	GM250-127-28-35	127	9.40	2.40	1.96	9.20	250	62	62	6.3	5
6937103	GM250-49-45-30	49	3.60	0.31	5.80	10.60	250	62	62	5.8	6
6937116	GM250-49-45-25	49	3.60	0.27	6.67	12.20	250	62	62	5.3	7

Chart 1

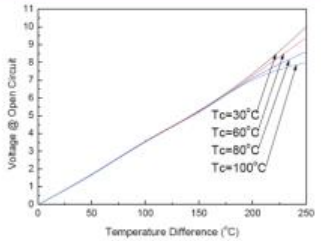

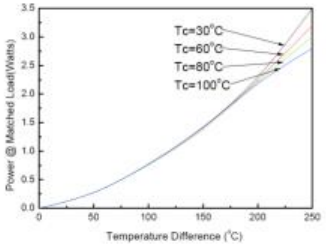

Chart 2

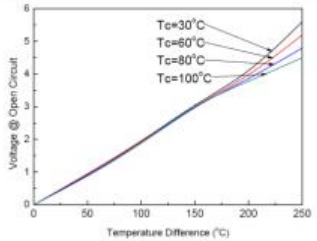

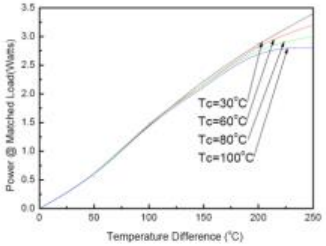

Chart 3

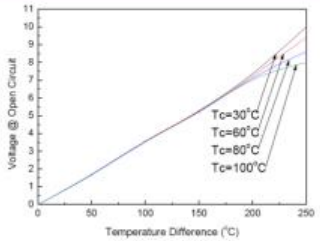

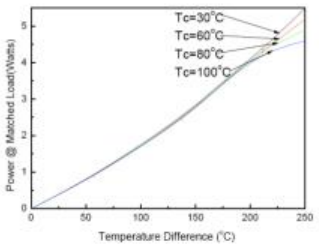

Chart 4

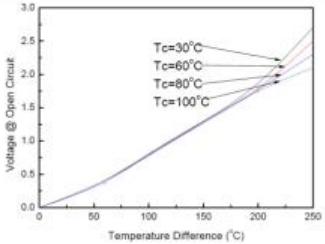

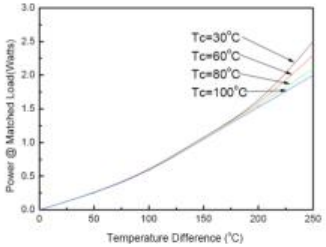

Chart 5

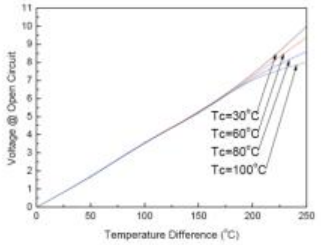

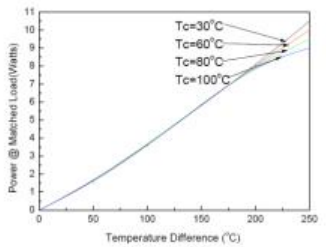

Chart 6

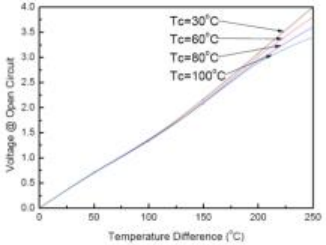

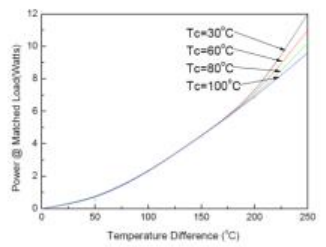

Chart 7

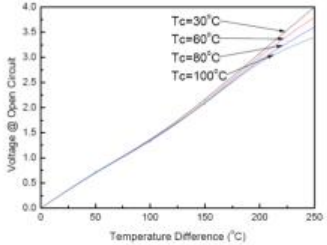

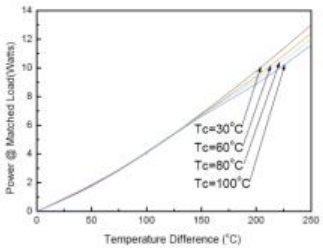

Dimensions

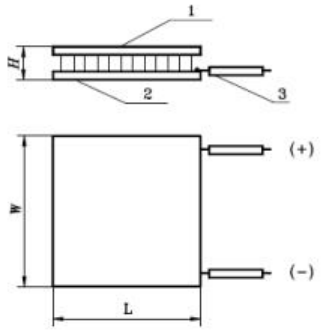

1—hot side, 2—Cold side, 3- wire.

European Thermodynamics Ltd
www.etdyn.com

Appendix B - The technical parameters and picture of the Arduino Uno microcontroller

CH340 UNO R3

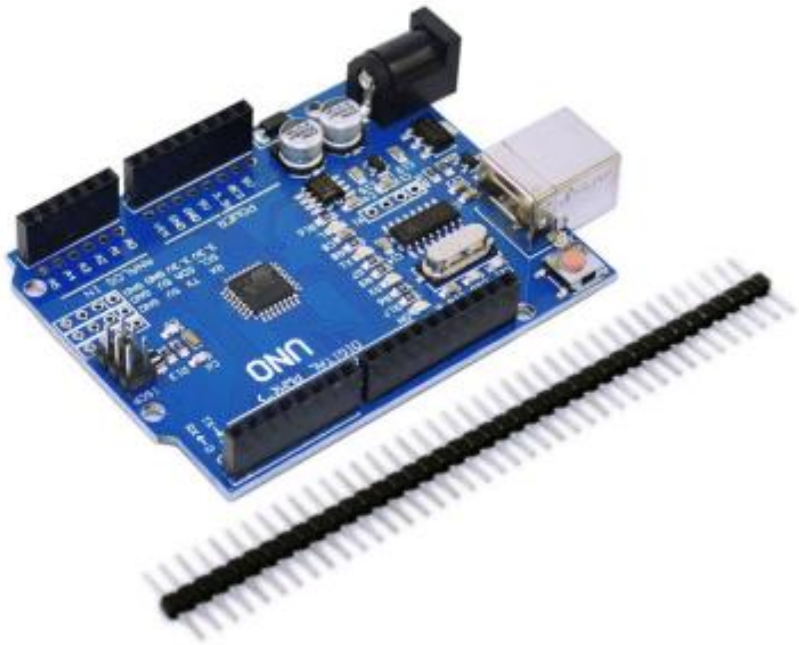

Introduction

This control board is optimized on the Arduino Uno R3 board. It mainly has two advantages, one is completely solving the incompatible and instable limitation of traditional UNO board under win7 and win8 system; another is replacing 16U2 chip with CH340G,with lower cost,offering you more benefits.

Technical Parameters

Microcontroller	ATmega328P-PU
Operating Voltage	5V
Input Voltage	5-9V
Digital I/O Pins	14 (of which 6 provide PWM output)

PWM Digital I/O Pins	6
Analog Input Pins	6
DC Current per I/O Pin	20 mA
DC Current for 3.3V Pin	50 mA
Flash Memory	32 KB (ATmega328P) of which 0.5 KB used by bootloader
SRAM	2 KB (ATmega328P)
EEPROM	1 KB (ATmega328P)
Clock Speed	16 MHz

Appendix C - The Arduino code to measure and display temperatures on LCD

```
#include <LiquidCrystal.h>
#define ADCPIN1 1
#define ADCPIN2 2
#define ADCPIN3 3
#define ADCPIN4 4

int units1 = 0; //Initialize variable to hold units
int units2 = 0;
int units3 = 0;
int units4 = 0;

int temperature1; //Initialize variable to hold temperature
int temperature2;
int temperature3;
int temperature4;
const int rs = 12, en = 11, d4 = 5, d5 = 4, d6 = 3, d7 = 2; //Declare RS, E, D4, D5, D6, D7
LiquidCrystal lcd(rs, en, d4, d5, d6, d7);

void setup()
{
  int temperature1 = 0;
  int temperature2 = 0;
```

```
  int temperature3 = 0;
  int temperature4 = 0;

  //Initialize the LCD Display
  lcd.begin(16, 2);

  lcd.setCursor(0, 0);              //T1 label position
  lcd.write("T1=");                 //Print Label for T1

  lcd.setCursor(0, 1);              //T2 label position
  lcd.write("T2=");                 //Print Label for T2

  lcd.setCursor(8, 0);              //T3 label position
  lcd.write("T3=");                 //Print Label for T3

  lcd.setCursor(8, 1);              //T4 label position
  lcd.write("T4=");                 //Print Label for T4
}

void loop()

{
```

```
units1 = analogRead(ADCPIN1);    //Read ADC of T1

units2 = analogRead(ADCPIN2);    //Read ADC of T2

units3 = analogRead(ADCPIN3);    //Read ADC of T3

units4 = analogRead(ADCPIN4);    //Read ADC of T4,


temperature1 = 0.6 * units1 - 4, 2;

temperature2 = 0.6 * units2 - 4, 2;

 temperature3 = 0.6 * units3 - 6, 2;

 temperature4 = 0.6 * units4 - 4, 2;


 lcd.setCursor(3, 0);

 lcd.print(temperature1);


 lcd.setCursor(3, 1);

 lcd.print(temperature2);


 lcd.setCursor(11, 0);

 lcd.print(temperature3);


  lcd.setCursor(11, 1);

  lcd.print(temperature4);

  }
```

Appendix D - The applications and electrical characteristics of the LM35DT temperature sensor

National Semiconductor

September 1997

LM35/LM35A/LM35C/LM35CA/LM35D Precision Centigrade Temperature Sensors

General Description

The LM35 series are precision integrated-circuit temperature sensors, whose output voltage is linearly proportional to the Celsius (Centigrade) temperature. The LM35 thus has an advantage over linear temperature sensors calibrated in ° Kelvin, as the user is not required to subtract a large constant voltage from its output to obtain convenient Centigrade scaling. The LM35 does not require any external calibration or trimming to provide typical accuracies of ±¼°C at room temperature and ±¾°C over a full −55 to +150°C temperature range. Low cost is assured by trimming and calibration at the wafer level. The LM35's low output impedance, linear output, and precise inherent calibration make interfacing to readout or control circuitry especially easy. It can be used with single power supplies, or with plus and minus supplies. As it draws only 60 µA from its supply, it has very low self-heating, less than 0.1°C in still air. The LM35 is rated to operate over a −55° to +150°C temperature range, while the LM35C is rated for a −40° to +110°C range (−10° with improved accuracy). The LM35 series is available packaged in hermetic TO-46 transistor packages, while the LM35C, LM35CA, and LM35D are also available in the plastic TO-92 transistor package. The LM35D is also available in an 8-lead surface mount small outline package and a plastic TO-220 package.

Features

- Calibrated directly in ° Celsius (Centigrade)
- Linear + 10.0 mV/°C scale factor
- 0.5°C accuracy guaranteeable (at +25°C)
- Rated for full −55° to +150°C range
- Suitable for remote applications
- Low cost due to wafer-level trimming
- Operates from 4 to 30 volts
- Less than 60 µA current drain
- Low self-heating, 0.08°C in still air
- Nonlinearity only ±¼°C typical
- Low impedance output, 0.1 Ω for 1 mA load

Typical Applications

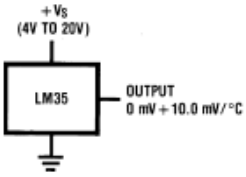

DS005516-3

FIGURE 1. Basic Centirade Temperature Sensor (+2°C to +150°C)

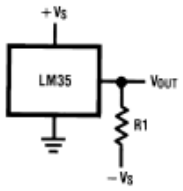

DS005516-4

Choose $R_1 = -V_S/50\ \mu A$
V_{OUT} = +1,500 mV at +150°C
= +250 mV at +25°C
= −550 mV at −55°C

FIGURE 2. Full-Range Centigrade Temperature Sensor

TRI-STATE® is a registered trademark of National Semiconductor Corporation.

Connection Diagrams

TO-46
Metal Can Package*

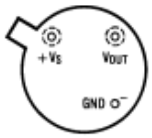

BOTTOM VIEW
DS005516-1

*Case is connected to negative pin (GND)

Order Number LM35H, LM35AH, LM35CH, LM35CAH or LM35DH
See NS Package Number H03H

TO-92
Plastic Package

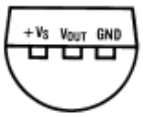

BOTTOM VIEW
DS005516-2

Order Number LM35CZ, LM35CAZ or LM35DZ
See NS Package Number Z03A

SO-8
Small Outline Molded Package

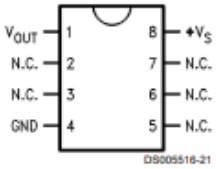

DS005516-21

N.C. = No Connection

Top View
Order Number LM35DM
See NS Package Number M08A

TO-220
Plastic Package*

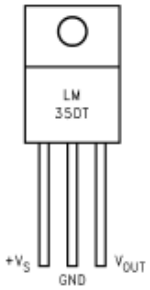

DS005516-24

*Tab is connected to the negative pin (GND).
Note: The LM35DT pinout is different than the discontinued LM35DP.

Order Number LM35DT
See NS Package Number TA03F

Absolute Maximum Ratings (Note 10)

If Military/Aerospace specified devices are required, please contact the National Semiconductor Sales Office/ Distributors for availability and specifications.

Supply Voltage	+35V to −0.2V
Output Voltage	+6V to −1.0V
Output Current	10 mA
Storage Temp.;	
TO-46 Package,	−60˚C to +180˚C
TO-92 Package,	−60˚C to +150˚C
SO-8 Package,	−65˚C to +150˚C
TO-220 Package,	−65˚C to +150˚C
Lead Temp.:	
TO-46 Package, (Soldering, 10 seconds)	300˚C
TO-92 and TO-220 Package, (Soldering, 10 seconds)	260˚C
SO Package (Note 12)	
Vapor Phase (60 seconds)	215˚C
Infrared (15 seconds)	220˚C
ESD Susceptibility (Note 11)	2500V
Specified Operating Temperature Range: T_{MIN} to T_{MAX} (Note 2)	
LM35, LM35A	−55˚C to +150˚C
LM35C, LM35CA	−40˚C to +110˚C
LM35D	0˚C to +100˚C

Electrical Characteristics

(Notes 1, 6)

Parameter	Conditions	LM35A			LM35CA			Units (Max.)
		Typical	Tested Limit (Note 4)	Design Limit (Note 5)	Typical	Tested Limit (Note 4)	Design Limit (Note 5)	
Accuracy (Note 7)	T_A=+25˚C	±0.2	±0.5		±0.2	±0.5		˚C
	T_A=−10˚C	±0.3			±0.3		±1.0	˚C
	T_A=T_{MAX}	±0.4	±1.0		±0.4	±1.0		˚C
	T_A=T_{MIN}	±0.4	±1.0		±0.4		±1.5	˚C
Nonlinearity (Note 8)	$T_{MIN} \le T_A \le T_{MAX}$	**±0.18**		**±0.35**	**±0.15**		**±0.3**	˚C
Sensor Gain (Average Slope)	$T_{MIN} \le T_A \le T_{MAX}$	**+10.0**	**+9.9, +10.1**		**+10.0**		**+9.9, +10.1**	mV/˚C
Load Regulation (Note 3) $0 \le I_L \le 1$ mA	T_A=+25˚C	±0.4	±1.0		±0.4	±1.0		mV/mA
	$T_{MIN} \le T_A \le T_{MAX}$	**±0.5**		**±3.0**	**±0.5**		**±3.0**	mV/mA
Line Regulation (Note 3)	T_A=+25˚C	±0.01	±0.05		±0.01	±0.05		mV/V
	$4V \le V_S \le 30V$	**±0.02**		**±0.1**	**±0.02**		**±0.1**	mV/V
Quiescent Current (Note 9)	V_S=+5V, +25˚C	56	67		56	67		µA
	V_S=+5V	**105**		**131**	**91**		**114**	µA
	V_S=+30V, +25˚C	56.2	68		56.2	68		µA
	V_S=+30V	**105.5**		**133**	**91.5**		**116**	µA
Change of Quiescent Current (Note 3)	$4V \le V_S \le 30V$, +25˚C	0.2	1.0		0.2	1.0		µA
	$4V \le V_S \le 30V$	**0.5**		**2.0**	**0.5**		**2.0**	µA
Temperature Coefficient of Quiescent Current		**+0.39**		**+0.5**	**+0.39**		**+0.5**	µA/˚C
Minimum Temperature for Rated Accuracy	In circuit of *Figure 1*, I_L=0	+1.5		+2.0	+1.5		+2.0	˚C
Long Term Stability	T_J=T_{MAX}, for 1000 hours	±0.08			±0.08			˚C

Electrical Characteristics

(Notes 1, 6)

Parameter	Conditions	LM35			LM35C, LM35D			Units (Max.)
		Typical	Tested Limit (Note 4)	Design Limit (Note 5)	Typical	Tested Limit (Note 4)	Design Limit (Note 5)	
Accuracy,	T_A=+25˚C	±0.4	±1.0		±0.4	±1.0		˚C
LM35, LM35C	T_A=−10˚C	±0.5			±0.5		±1.5	˚C
(Note 7)	T_A=T_{MAX}	±0.8	±1.5		±0.8		±1.5	˚C
	T_A=T_{MIN}	±0.8		±1.5	±0.8		±2.0	˚C
Accuracy, LM35D	T_A=+25˚C				±0.6	±1.5		˚C
(Note 7)	T_A=T_{MAX}				±0.9		±2.0	˚C
	T_A=T_{MIN}				±0.9		±2.0	˚C
Nonlinearity	T_{MIN}≤T_A≤T_{MAX}	**±0.3**		**±0.5**	**±0.2**		**±0.5**	˚C
(Note 8)								
Sensor Gain	T_{MIN}≤T_A≤T_{MAX}	**+10.0**	**+9.8, +10.2**		**+10.0**		**+9.8, +10.2**	mV/˚C
(Average Slope)								
Load Regulation	T_A=+25˚C	±0.4	±2.0		±0.4	±2.0		mV/mA
(Note 3) 0≤I_L≤1 mA	T_{MIN}≤T_A≤T_{MAX}	**±0.5**		**±5.0**	**±0.5**		**±5.0**	mV/mA
Line Regulation	T_A=+25˚C	±0.01	±0.1		±0.01	±0.1		mV/V
(Note 3)	4V≤V_S≤30V	**±0.02**		**±0.2**	**±0.02**		**±0.2**	mV/V
Quiescent Current	V_S=+5V, +25˚C	56	80		56	80		µA
(Note 9)	V_S=+5V	**105**		**158**	**91**		**138**	µA
	V_S=+30V, +25˚C	56.2	82		56.2	82		µA
	V_S=+30V	**105.5**		**161**	**91.5**		**141**	µA
Change of	4V≤V_S≤30V, +25˚C	0.2	2.0		0.2	2.0		µA
Quiescent Current	4V≤V_S≤30V	**0.5**		**3.0**	**0.5**		**3.0**	µA
(Note 3)								
Temperature Coefficient of Quiescent Current		**+0.39**		**+0.7**	**+0.39**		**+0.7**	µA/˚C
Minimum Temperature for Rated Accuracy	In circuit of *Figure 1*, I_L=0	+1.5		+2.0	+1.5		+2.0	˚C
Long Term Stability	T_J=T_{MAX}, for 1000 hours	±0.08			±0.08			˚C

Note 1: Unless otherwise noted, these specifications apply: −55˚C≤T_J≤+150˚C for the LM35 and LM35A; −40˚≤T_J≤+110˚C for the LM35C and LM35CA; and 0˚≤T_J≤+100˚C for the LM35D. V_S=+5Vdc and I_{LOAD}=50 µA, in the circuit of *Figure 2*. These specifications also apply from +2˚C to T_{MAX} in the circuit of *Figure 1*. Specifications in **boldface** apply over the full rated temperature range.

Note 2: Thermal resistance of the TO-46 package is 400˚C/W, junction to ambient, and 24˚C/W junction to case. Thermal resistance of the TO-92 package is 180˚C/W junction to ambient. Thermal resistance of the small outline molded package is 220˚C/W junction to ambient. Thermal resistance of the TO-220 package is 90˚C/W junction to ambient. For additional thermal resistance information see table in the Applications section.

Note 3: Regulation is measured at constant junction temperature, using pulse testing with a low duty cycle. Changes in output due to heating effects can be computed by multiplying the internal dissipation by the thermal resistance.

Note 4: Tested Limits are guaranteed and 100% tested in production.

Note 5: Design Limits are guaranteed (but not 100% production tested) over the indicated temperature and supply voltage ranges. These limits are not used to calculate outgoing quality levels.

Note 6: Specifications in **boldface** apply over the full rated temperature range.

Note 7: Accuracy is defined as the error between the output voltage and 10mv/˚C times the device's case temperature, at specified conditions of voltage, current, and temperature (expressed in ˚C).

Note 8: Nonlinearity is defined as the deviation of the output-voltage-versus-temperature curve from the best-fit straight line, over the device's rated temperature range.

Note 9: Quiescent current is defined in the circuit of *Figure 1*.

Note 10: Absolute Maximum Ratings indicate limits beyond which damage to the device may occur. DC and AC electrical specifications do not apply when operating the device beyond its rated operating conditions. See Note 1.

Note 11: Human body model, 100 pF discharged through a 1.5 kΩ resistor.

Note 12: See AN-450 "Surface Mounting Methods and Their Effect on Product Reliability" or the section titled "Surface Mount" found in a current National Semiconductor Linear Data Book for other methods of soldering surface mount devices.

Typical Performance Characteristics

Thermal Resistance Junction to Air

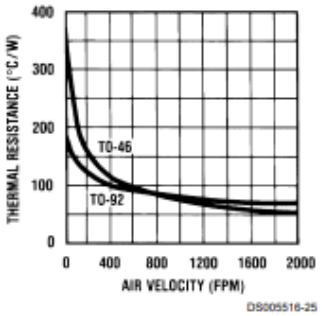

DS005516-25

Thermal Time Constant

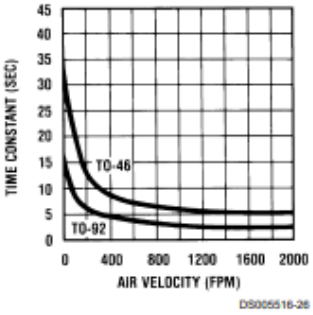

DS005516-26

Thermal Response in Still Air

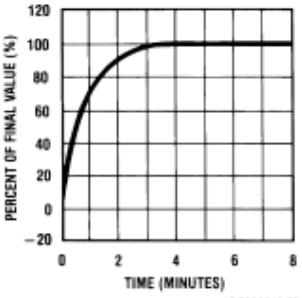

DS005516-27

Thermal Response in Stirred Oil Bath

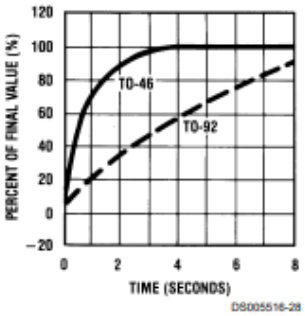

DS005516-28

Minimum Supply Voltage vs. Temperature

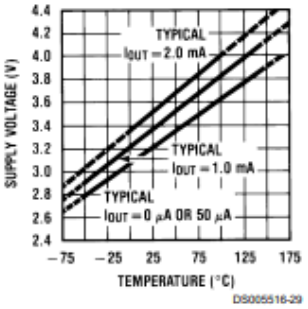

DS005516-29

Quiescent Current vs. Temperature (In Circuit of *Figure 1*.)

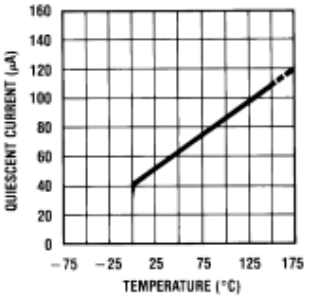

DS005516-30

Quiescent Current vs. Temperature (In Circuit of *Figure 2*.)

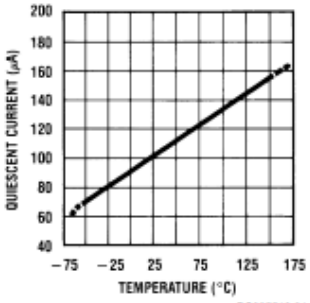

DS005516-31

Accuracy vs. Temperature (Guaranteed)

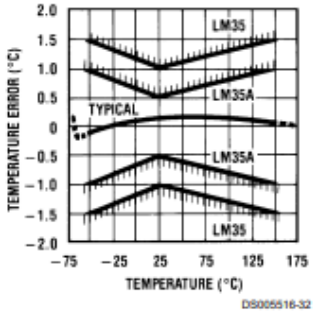

DS005516-32

Accuracy vs. Temperature (Guaranteed)

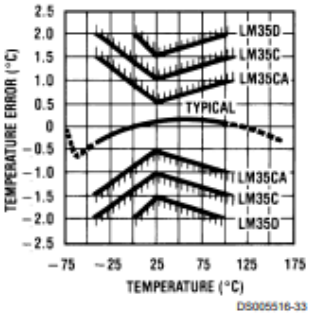

DS005516-33

Typical Performance Characteristics (Continued)

Noise Voltage

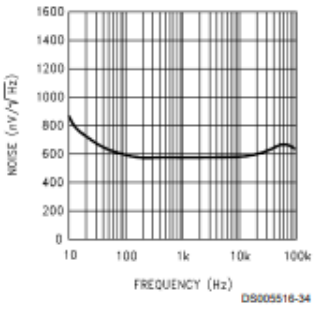

Start-Up Response

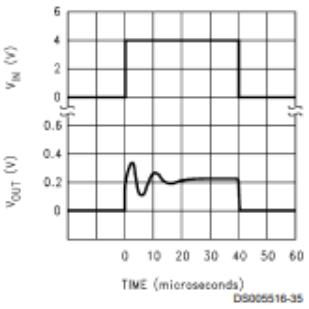

Applications

The LM35 can be applied easily in the same way as other integrated-circuit temperature sensors. It can be glued or cemented to a surface and its temperature will be within about 0.01˚C of the surface temperature.

This presumes that the ambient air temperature is almost the same as the surface temperature; if the air temperature were much higher or lower than the surface temperature, the actual temperature of the LM35 die would be at an intermediate temperature between the surface temperature and the air temperature. This is expecially true for the TO-92 plastic package, where the copper leads are the principal thermal path to carry heat into the device, so its temperature might be closer to the air temperature than to the surface temperature.

To minimize this problem, be sure that the wiring to the LM35, as it leaves the device, is held at the same temperature as the surface of interest. The easiest way to do this is to cover up these wires with a bead of epoxy which will insure that the leads and wires are all at the same temperature as the surface, and that the LM35 die's temperature will not be affected by the air temperature.

The TO-46 metal package can also be soldered to a metal surface or pipe without damage. Of course, in that case the V− terminal of the circuit will be grounded to that metal. Alternatively, the LM35 can be mounted inside a sealed-end metal tube, and can then be dipped into a bath or screwed into a threaded hole in a tank. As with any IC, the LM35 and accompanying wiring and circuits must be kept insulated and dry, to avoid leakage and corrosion. This is especially true if the circuit may operate at cold temperatures where condensation can occur. Printed-circuit coatings and varnishes such as Humiseal and epoxy paints or dips are often used to insure that moisture cannot corrode the LM35 or its connections.

These devices are sometimes soldered to a small light-weight heat fin, to decrease the thermal time constant and speed up the response in slowly-moving air. On the other hand, a small thermal mass may be added to the sensor, to give the steadiest reading despite small deviations in the air temperature.

Temperature Rise of LM35 Due To Self-heating (Thermal Resistance, Θ_{JA})

	TO-46, no heat sink	TO-46*, small heat fin	TO-92, no heat sink	TO-92**, small heat fin	SO-8 no heat sink	SO-8** small heat fin	TO-220 no heat sink
Still air	400˚C/W	100˚C/W	180˚C/W	140˚C/W	220˚C/W	110˚C/W	90˚C/W
Moving air	100˚C/W	40˚C/W	90˚C/W	70˚C/W	105˚C/W	90˚C/W	26˚C/W
Still oil	100˚C/W	40˚C/W	90˚C/W	70˚C/W			
Stirred oil	50˚C/W	30˚C/W	45˚C/W	40˚C/W			
(Clamped to metal, Infinite heat sink)	(24˚C/W)				(55˚C/W)		

*Wakefield type 201, or 1" disc of 0.020" sheet brass, soldered to case, or similar.
**TO-92 and SO-8 packages glued and leads soldered to 1" square of 1/16" printed circuit board with 2 oz. foil or similar.